A Computational Study of Flow Over a Wall-Mounted Cube in a Turbulent Boundary Layer Using Large Eddy Simulations

by

Siddhesh Dilip Shinde

A dissertation submitted in partial fulfillment
of the requirements for the degree of
Doctor of Philosophy
(Mechanical Engineering and Scientific Computing)
in The University of Michigan
2018

Doctoral Committee:

Associate Professor Eric Johnsen, Chair
Assistant Professor Jesse Capecelatro
Associate Professor Kevin Maki
Professor Joaquim Martins

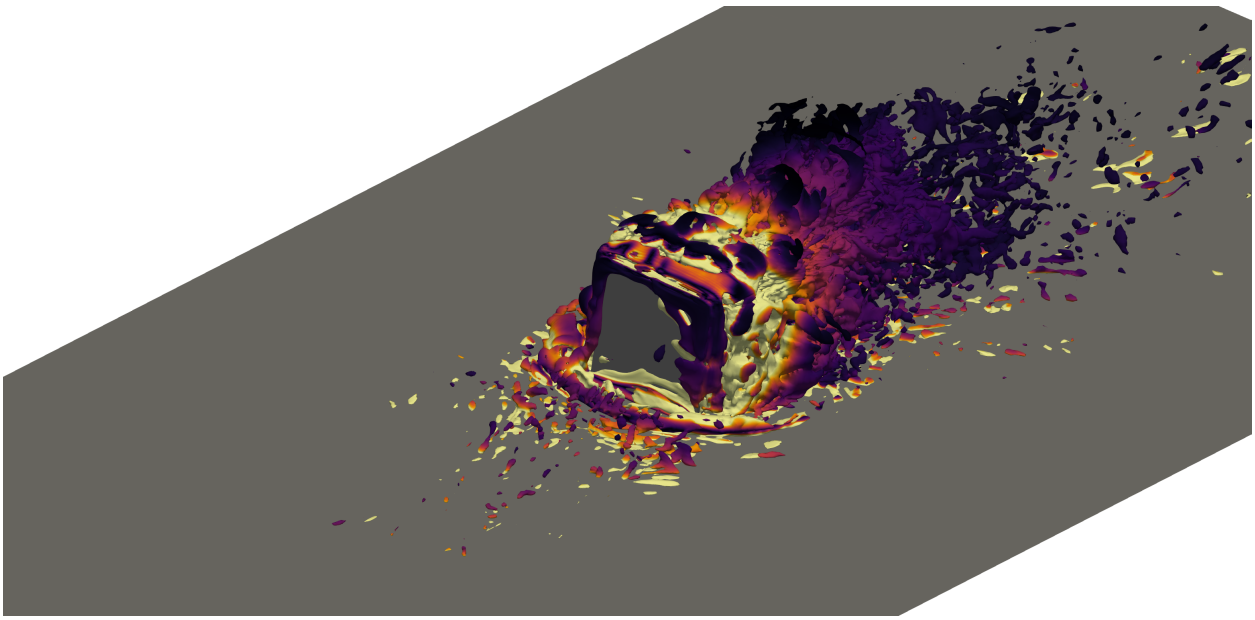

Siddhesh Shinde
siddhesh@umich.edu
ORCID iD: 0000-0002-0378-6761

To Aai and Baba

ACKNOWLEDGEMENTS

First and foremost I would like to express my immense gratitude and love towards my family, especially my parents, who taught me to be fearless and always motivated me to strive for excellence. This thesis would not have been possible without their support, for which I will forever be in their debt. I would like to express my deepest thanks to Dr. Eric Johnsen, my adviser, for this continued guidance and intellectual support during the course of my thesis. His advice has helped me excel in my research endeavor, and enabled me to perform at the best of my ability. I take this opportunity to thank Dr. Kevin Maki for his valuable inputs that have played a vital role in shaping my thesis objectives. I extend my thanks to my committee members Dr. Joaquim Martins, and Dr. Jesse Capecelatro for their thoughts and advice on my work. I would also like to thank Dr. Pooya Movahed for his contributions in developing the inflow boundary condition method.

My experiences at the University of Michigan have been invaluable in shaping my personality, and I am thankful for the memories I will cherish forever. I want to thank my colleague and dear friend, Suyash. Our research has progressed in tandem since the inception of my thesis, and I believe have gained a valuable friend for life. I want to thank all my friends including Vicky for co-founding "House of Bhaus", Jovin for being the younger brother away from home, Sameer for his wit and delicious cooking, Nikhil for his Chai sessions, Prasad for his life lessons, Nitish for his anecdotes, Sumit for his social media skills, and Namit for his Bollywood enthusiasm. I truly believe my time at the University of Michigan would not have been nearly as fulfilling without the company of my friends in the Autolab. I am thankful to Brian for his house parties and science talks, TJ for his board problems and humor, Brandon

for this help with anything computer related, Mauro for proof-reading my documents, Marc for his research related inputs, Sam for his insights into French culture, Harish for his philosophy about life, Phil for sharing his DG wisdom, Kevin for his March madness enthusiasm, and Greg and Yang for all the OpenFOAM related help. Their presence made the Autolab a fun place to work and my graduate experience a pleasant journey. During my PhD I served on the board of Graduate Rackham INternational (GRIN) student organization. I want to thank everyone at GRIN for giving me the opportunity to contribute my bit to improving the graduate life experience of all international students on campus. I also worked with the Michigan Data Science Team (MDST) on exciting machine-learning projects, and I am grateful to them for this collaborative opportunity. Finally, I want to thank my undergrad friends from Sardar Patel College of Engineering (SPCE), Mumbai, India: Jugal, Kumar, Priyam, Ankit, Atharv, Chaithra, Parshva, Manalee, Pranav, Arati, Saurabh, Saumil, for all the adventures, love and craziness.

This work used the Extreme Science and Engineering Discovery Environment (XSEDE), which is supported by National Science Foundation grant number ACI-1053575.

TABLE OF CONTENTS

LIST OF FIGURES

Figure

LIST OF TABLES

Table

LIST OF APPENDICES

Appendix

LIST OF ABBREVIATIONS

CFD Computational Fluid Dynamics

TBL Turbulent Boundary Layer

APG Adverse Pressure Gradient

FPG Favorable Pressure Gradient

LES Large Eddy Simulation

SGS Sub-Grid Scale

SETBL Spatially Evolving Turbulent Boundary Layer

TKE Turbulent Kinetic Energy

DNS Direct Numerical Simulation

LUST Linear Upwind Stabilized Transport

FVM Finite Volume Method

PISO Pressure Implicit with Splitting of Operator

SIMPLE Semi-Implicit Method for Pressure-Linked Equations

CFL Courant-Friedrichs-Lewy

KDE Kernel Density Estimation

PDF Probability Density Function

HIT Homogenous Isotropic Turbulence

FFT Fast Fourier Transform

PDE Partial Differential Equation

FST Free-Stream Turbulence

ABSTRACT

Flow over a wall-mounted cube in a turbulent boundary layer is a canonical problem with applications in many engineering systems. Atmospheric flow over buildings in an urban environment or vegetative canopies, air flow over road vehicles, flow over printed circuit boards, etc., are few examples which can be modeled by considering flow over wall-mounted cubes. Without loss of generality, the problem of interest in this work is controlling the separation region on the rear end of road vehicles to reduce aerodynamic drag. To do so, we intend to use an array of cubes placed in single line normal to the flow direction, as passive vortex generators (VGs) to reduce flow separation. Flow separation is caused by a strong adverse pressure gradient (APG). As the flow expends its kinetic energy to overcome the strong APG it decelerates, and eventually separates from the surface. It is important to reduce flow separation to improve and maintain aerodynamic efficiency, and the approach of interest is to energize the flow to help overcome the APG. Passive VGs aid in reducing flow separation by entraining the turbulent kinetic energy (TKE) from the free-stream flow to the near wall region. Prior research in passive flow control reveals that the effectiveness of a VG in controlling separation depends on multiple factors which include, the size of the VG relative to the boundary layer thickness, spacing between adjacent VGs, and position of the VG with respect to the line of separation. Performing experiments of the different VG geometries and configurations is both expensive and time consuming. While recent advances in numerical methods and computational resources have brought more complex flows under our computational grasp, resolving all the length and time scales for a large portion of real-world flows is still unfeasible. Large Eddy Simulations (LES) provide a promising alternative,

and is our tool for investigation in this study.

An optimal deployment of cubes to control boundary layer separation requires a thorough understanding of the TKE entrainment and distribution in the wake of the cubes. The dependence of these quantities on the cube to height (h) to boundary layer thickness (δ) ratio, and spacing between adjacent cubes (w/h) is poorly understood. Therefore, the objectives of this work are to perform LES of flow over wall-mounted cubes in turbulent boundary layer (TBL) to understand the effect of: (i) h/δ on the wake characteristics in general, and TKE distribution in particular (ii) inter-cube spacing (w/h) on the TKE distribution in the wake of a single line of cubes placed normal to the flow direction. To achieve these objectives, we validate an existing approach to simulate a spatially evolving turbulent boundary layer (SETBL), and propose a novel method using machine learning for the same purpose, with the aim of reducing computation time without any significant modification to the numerical framework. For a single cube placed in SETBL on a flat plate we discover that the TKE per unit area decays as a power law in the near-wake, and the power law exponent increases in a non-linear manner with increasing h/δ. The presence of the cube results in a departure from the state of equilibrium of the TBL, and a higher value of the power law exponent facilitates the faster transition back toward equilibrium. LES of flow over an array of cubes in SETBL reveals amplification of large scale coherent structures in the outer region of the TBL, which are characterized by increasing TKE. We believe the ejection of low momentum fluid in the region in between adjacent cubes is responsible for this amplification. From our physics-based findings we propose an optimal configuration of a row of cube shaped VGs to reduce pressure drag on road vehicles. We believe the cube height should be between 0.6δ and δ, the spacing between adjacent cubes should be between $3h$ and $4h$, and the row of cubes should be placed at an approximate distance of $5w$ from the line of separation. Our findings have direct applications in reducing aerodynamic drag on automobiles, aircrafts and improving turbine efficiency, which in turn can help us reduce greenhouse gas emissions.

CHAPTER I

Introduction

This chapter explains the motivation of our work. It defines the scope of the dissertation and the application of our work to solving problems of academic and engineering interest. Presented work lies within the broad research area of *computational fluid dynamics* (CFD). The goal behind pursuing a deeper understanding of a turbulent boundary layer flow over a wall-mounted cube is explained, along with a comprehensive review of relevant literature. The use of large eddy simulation approach as our preferred tool of investigation is defended, and the application of our results in reducing emissions of greenhouse gases from automobiles is explained. Finally, this chapter concludes with the thesis objective and the outline.

1.1 Physical context and applications

Turbulent flows are ubiquitous in nature. Flow of water in rivers, air flowing on the surface of earth, flow of air over an aircraft or an automobile, combustion of fuels in an engine, etc., are all examples of turbulent flows. Understanding the universal nature of turbulent flows has eluded researchers for a long time. One of the most notable contributions to the field of turbulence research was made by Kolmogorov (1941) [13]. Kolmogorov's hypotheses provided a foundation connecting the underlying nature of all turbulent flows. Based on the speed of the fluid under consideration in the problem, the variation in density of the fluid may or may not be significant. The importance of density variation is governed by the ratio

of fluid velocity (u) to the speed of sound in the medium (c), known as Mach number ($\mathcal{M}$), i.e., $\mathcal{M} = u/c$. As a rule of thumb if $\mathcal{M} \lesssim 0.3$ the flow is considered to be *incompressible*, and considered *compressible* in other scenarios. Flow over an aircraft cruising at high speeds is an example of a compressible turbulent flow, whereas flow over an automobile moving on a freeway is an example of an incompressible turbulent flow.

The problem of interest in the present work lies in the incompressible wall-bounded turbulent flow regime. The term "wall-bounded" refers to the fact that the fluid motion occurs in contact with a solid surface. Air flow over the surface of a car, an aircraft, or the earth are all examples of wall-bounded turbulent flows. The effect of the solid surface on the fluid flow is explained in Sec. 1.2. A common characteristic of all turbulent flows is the presence of a wide spectrum of length scales. These large and small length scales are stochastically time-varying, and a closed form analytical solution to determine the turbulent flow quantities does not exist. Therefore, in the present work we resort to computational methods to solve the governing system of equations.

The specific problem investigated in this study is turbulent flow over a wall-mounted cube. The canonical nature of the problem and its applicability in various engineering systems makes it an attractive problem for a high-fidelity, physics-based computational study. The numerical framework developed in this work can be further applied to investigate problems with applications in design of turbo-machinery, buildings, circuit boards, etc. However, it is important to mention that the quantities investigated and the choice of parameters in our work are influenced by the efforts in reducing aerodynamic drag on road vehicles. In the following sections we explain the fundamental concepts necessary to understand the motivation behind this research campaign, and describe the objectives and contributions of this thesis.

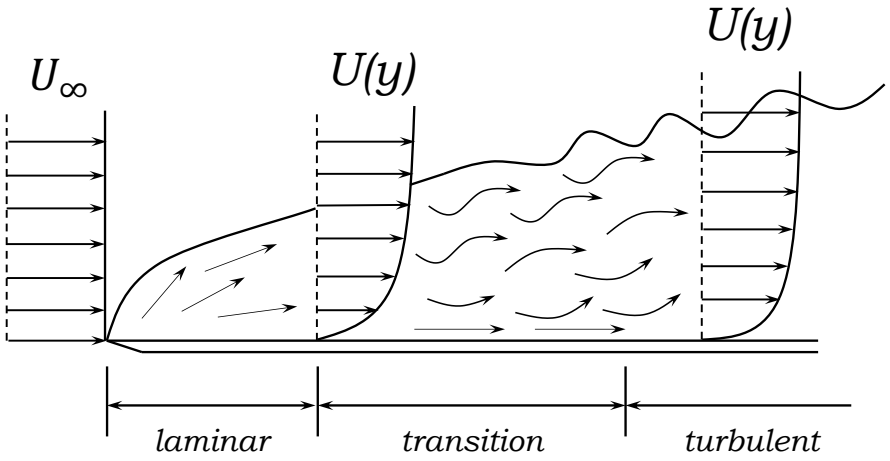

Figure 1.1: A schematic representation of laminar to turbulent boundary layer transition.

1.2 Turbulent boundary layer on a flat plate

When a fluid moves along a solid surface, due to the viscosity of the fluid a region develops close to the wall where the fluid velocity is much lower than the fluid velocity far away from the wall, and where the shear stresses are increasingly dominant. On the surface where the fluid meets the solid, the velocity of the fluid must be equal to that of the solid. This boundary condition is referred to as *no-slip*. At the surface, the fluid is at rest relative to the surface, whereas the fluid continues to move at the free-stream velocity far away from the surface. This difference results in a gradient of fluid velocity as a function of its wall-normal distance from the surface. This region extending from the surface to a point at which the fluid attains 99% of the free-stream velocity is called as the boundary layer. The height of the boundary layer is usually denoted by δ. This concept was first introduced by Prandtl in 1904 [14]. The boundary layer can be laminar or turbulent in nature. In case of laminar flow, the fluid flows in "layers", and the transfer of momentum takes place only across adjacent layers. In a turbulent flow on the other hand, there is transfer of momentum across the flow in a more effective manner than a comparable laminar flow. This is well demonstrated by an experiment conducted by injecting dye on the centerline of a long pipe in which water is flowing [15]. As Reynolds [16] later established, this flow is characterized by a single non-

dimensional parameter, now known as the *Reynolds number* (Re). The Reynolds number is defined in Eq. 1.1.

$$\text{Reynolds number, } Re = \frac{\rho U L}{\mu} \tag{1.1}$$

where ρ is the fluid density, U is the characteristic flow velocity, L is the characteristics length scale associated with the flow, and μ is the dynamic viscosity of the fluid. In Reynolds' pipe-flow experiment, if the Re is less than about 2,300, the flow is laminar, and the dye injected on the centerline forms a long streak that increases in diameter only slightly with downstream distance. If, on the other hand, Re exceeds about 4,000, then the flow is turbulent[1]. The dye streak is jiggled about by the turbulent motion; it becomes progressively less distinct with downstream distance; and eventually mixing with the surrounding water reduces the peak dye concentration to the extent that it is no longer visible. The Reynolds number relates the magnitude of inertia to viscous forces. For a fluid moving on a flat surface if the Reynolds number is higher than a critical value ($\sim 5 \times 10^5$), the boundary layer transitions from a laminar to a turbulent regime as depicted in Fig. 1.1.

The turbulent boundary layer (TBL) is a complex flow phenomenon, and it is characterized by a wide-range of length and time scales. A TBL can be further divided into a *inner region* and a *outer region*, as illustrated in Fig. 1.2. The inner region is the region close to the wall, where the magnitude of the viscous forces is comparable to the inertial forces. The characteristics length scale inside the inner region is much smaller than that in the outer region, and it is densely populated with coherent structures [17, 18]. These coherent structures scale with the friction velocity (u_τ) and the kinematic viscosity (ν), and u_τ and ν are known as the *inner variables*. The inner region extends to a height of $y \approx 0.2\delta$ from the wall [19, 20], and it is characterized by high levels of production and dissipation of turbulent

[1]As the Reynolds number is increased, the transition from laminar to turbulent flow occurs over a range of Re, and this range depends on the details of the experiment.

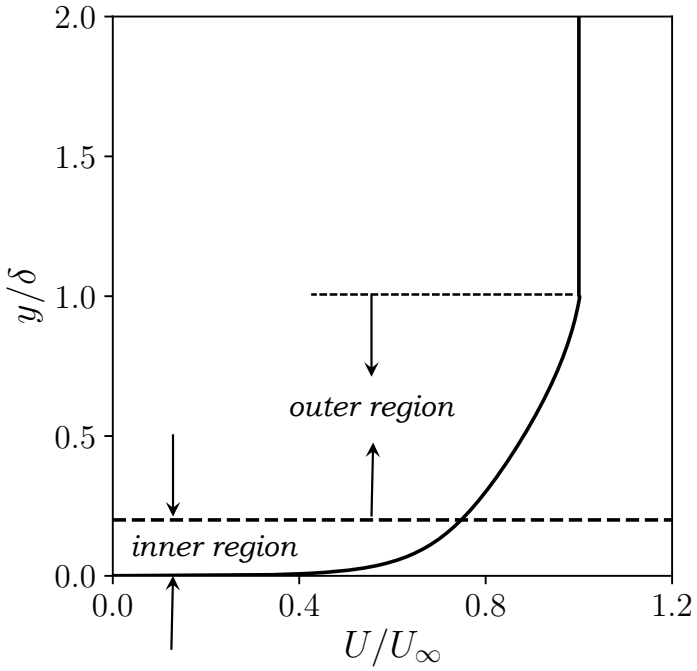

Figure 1.2: Mean turbulent boundary layer velocity profile normalized by the outer variables.

kinetic energy (TKE). The outer region extends from $y \approx 0.2\delta$ to the end boundary layer, and has low levels of TKE production. Inertial forces are dominant in the outer region, and the length scales in this region are governed by the outer variables, i.e., flow velocity (U) and TBL thickness (δ). The outer region has larger coherent structures known as the hairpin vortices, which are organized in packets, and are of the size of the boundary layer thickness [21, 22]. Many researchers have investigated different aspects of the TBL in great detail over the years [23, 24, 25]. TBLs are a common occurrence in engineering applications, and separation of the TBL from the surface can have profound consequences on the efficiency of the application.

1.3 Flow separation

When flow along a surface decelerates too strongly, streamlines detach from the surface in a process called *flow separation*. Flow separation occurs either due to a strong adverse pressure gradient (APG) on a smooth surface, or a surface discontinuity. Consider the

stream-wise momentum equation inside a boundary layer in the limit, $Re \to \infty$, presented in Eq. 1.2.

$$\frac{\partial u}{\partial t} + u\frac{\partial u}{\partial x} + v\frac{\partial u}{\partial y} = -\frac{1}{\rho}\frac{\partial p}{\partial x} + \nu\frac{\partial^2 u}{\partial y^2} \tag{1.2}$$

At the solid surface, $y = 0$, at steady state we have, $\partial u/\partial t = 0, u = 0$ and $v = 0$, so that,

$$\frac{dp}{dx} = \mu\frac{\partial^2 u}{\partial y^2}$$

On the surface $\partial^2 u/\partial y^2$ must always have the same sign as the pressure gradient, dp/dx, and in case of an APG, $dp/dx > 0$. However, at the edge of the boundary layer we must have, $\partial^2 u/\partial y^2 < 0$. Therefore, there must exist an inflection point between the cross-over from the inner region of $\partial^2 u/\partial y^2 > 0$ and the outer region of $\partial^2 u/\partial y^2 < 0$. As we proceed along the stream-wise direction the gradient of the velocity profile becomes so steep that,

$$\left(\frac{\partial u}{\partial y}\right)_{y=0} = 0$$

This point is defined as the point of separation. When a TBL approaches separation due to a strong APG, it results in modification of the coherent structures inside the boundary layer; coherent streaks tend to disappear or reduce [26, 27]. Flow separation and the stages that lead to it have been studied in great detail. Yet, investigating the flow characteristics in the separated and reattachment regions is an area of active research. Stratford *et al.* [28] developed a criterion for turbulent boundary layer separation on a flat plate. Work done by Simpson *et al.* [29] on measurements of flows with adverse pressure gradient revealed that the log law is maintained until close to separation. More recently, direct numerical simulation (DNS) of separating turbulent boundary layer studied by Na *et al.* [30] revealed stark similarities in the kinetic energy budget in the separated region to that of a plane mixing layer. Along with studying the underlying universal nature of the boundary layer in separated regions, the subsequent reattachment and recovery of the boundary layer have

been investigated with equal interest. In the review on recovery of a boundary layer, Smits *et al.* [31] report that the recovery process initiates from the wall and grows outwards in the shear layer. However, Alving *et al.* [32] present a contrary view observed while studying mild separation of a turbulent boundary layer in which the recovery process is initiated in the outer layer. Flow separation has drastic effects in engineering applications like, drop in lift and increase in drag of an aircraft, drop in efficiency of turbo-machinery, energy losses in subsonic diffusers, increased after-body drag in aircraft fuselage, etc., making flow separation control important.

1.4 Control of flow separation

When a TBL encounters a strong APG it expends its energy to overcome the APG. According to the Bernoulli equation, the kinetic energy gradient ($\frac{1}{2}\Delta u^2$) is working against the pressure gradient ($\Delta p/\rho$). The point at which the flow can no longer overcome the APG, it separates. Conversely, one might expect that energizing the flow will help mitigate flow separation. This is the fundamental idea behind *flow separation control* strategies that are relevant to the present work. Energizing the TBL can be achieved by inducing strong stream-wise and/or span-wise vortices near the wall, which entrain high momentum fluid from the free-stream to the near wall region. The methods used to facilitate this momentum transfer can be classified into two categories: *passive* and *active flow control*.

1.4.1 Passive flow control

In *passive flow control* methods, stationary objects are mounted on the surface inside the flow domain, before the flow separates. These objects are referred to as *passive vortex generators* (VGs). Passive VGs have been found to be most effective in controlling flow separation in applications where flow separation line is relatively fixed [2] like, flow over a backward-facing step [33, 34]. Passive VGs with different shapes and sizes have been investigated, which include, vane-type, span-wise cylinders, wheeler's doublets, wishbone

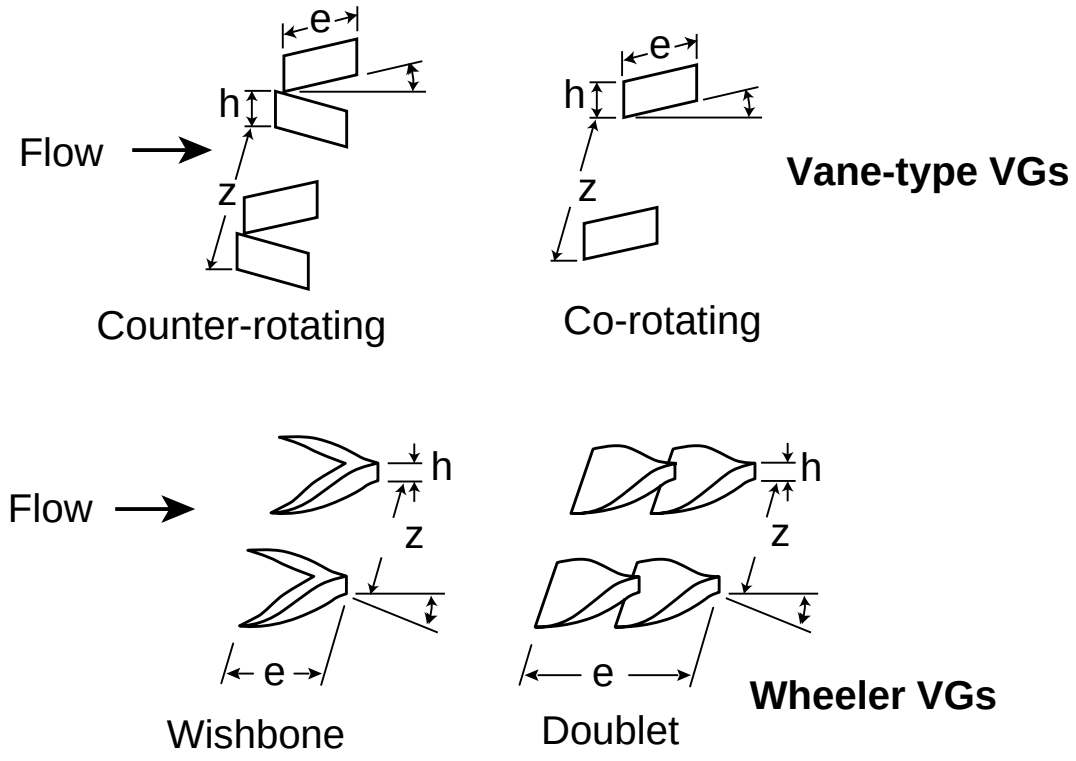

Figure 1.3: Different passive vortex generator configurations from Lin [2], © Elsevier. Reproduced with permission. All rights reserved.

type etc. as seen in Fig. 1.3. Passive VGs modify the flow by entraining turbulent kinetic energy from the mean flow to the near the wall region inside a TBL. The increased TKE helps to overcome the adverse pressure gradient, and reduce the region of flow separation. Reduction in flow separation can be beneficial in reducing pressure drag, as demonstrated by Pujals *et al.* [8]. They used cylinder shaped passive VGs to reduce pressure drag on a simplified car model.

The effectiveness of passive VGs depends on the size (h) of the VG compared to the boundary layer thickness (δ). Larger VGs produce stronger vortices however, they also have a greater device drag associated with their size. VGs of size comparable to the boundary layer thickness (δ) have been used by early researchers [35, 2]. However, it was soon realized that larger VGs have a greater device drag associated with their shape, and soon they were replaced by sub-merged VGs, with height $h \sim 0.2\delta$ [36, 2]. Sub-merged VGs are found

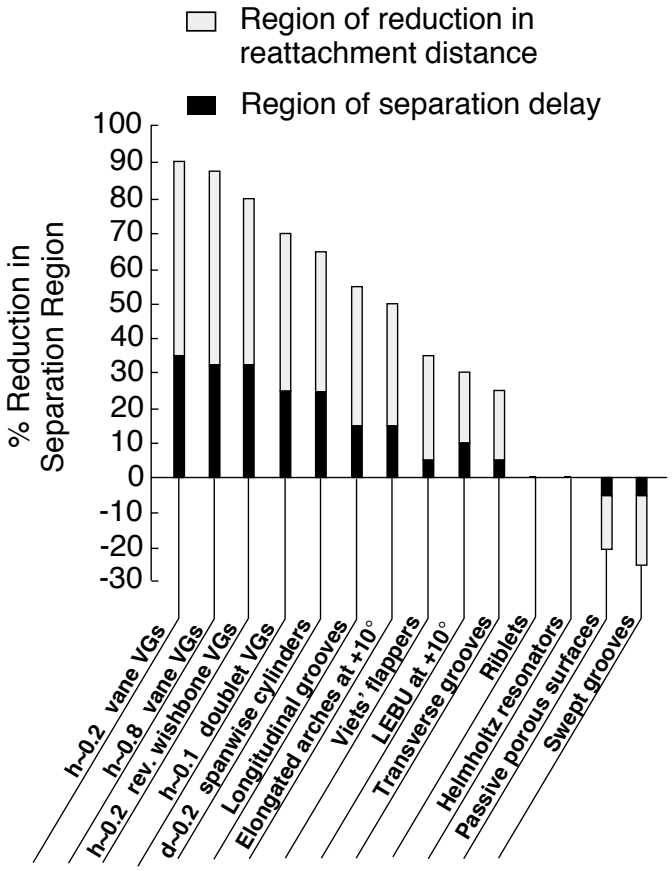

Figure 1.4: Relative effectiveness of flow separation control versus device category from Lin [2], © Elsevier. Reproduced with permission. All rights reserved.

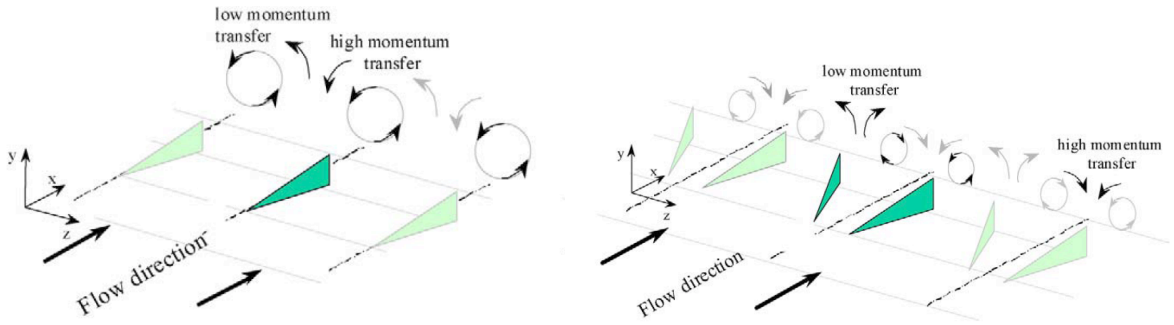

(a) co-rotating vane-type VG (b) counter-rotating vane-type VG

Figure 1.5: Streamwise vortices produced by vane-type VGs from Cuvier [3].

to be more efficient in momentum transfer than bigger VGs [36, 2, 37]. In 2002, Lin *et al.* published work on an extensive exploratory analysis on the effectiveness of different

passive VGs in flow control. They measured the effectiveness of a VG configuration based on the percentage reduction in separation region, as observed in Fig. 1.4. They concluded that submerged VGs that produce strong stream-wise vortices like the vane-type, are most effective in separation control, Fig. 1.5, followed by VGs that produce span-wise vortices, like span-wise cylinders. Researchers have explored a variety of shapes of passive VGs to control separation on different geometries [35, 36, 2, 38]. From [2, 38] and several others it is clear the effectiveness of the VG in controlling boundary layer separation depends on the size of the VG relative to the boundary layer thickness, the span-wise spacing between the VGs, and the streamwise distance between the VG trailing edge and the line of separation.

1.4.2 Active flow control

Active flow control is the use of actuators to convert electrical energy to fluid flow disturbances. There are scenarios in which flow control is needed only under specific conditions, in which case continuously using a passive VG would result in performance degradation. An example is the flow separation that occurs on the wings on an aircraft during landing and take off. When an aircraft lands or take off, the wings are exposed to high angles of attack, leading to separated flow on the suction side however, when the aircraft is in cruise condition, the airfoil is designed such that there is no separation. If passive VGs were used in cruise conditions they would result in increased drag and lower efficiency. To overcome this problem, active devices have been developed, which can be turned off when not required. There are various types of actuators used to interact with the flow, which can be classified in numerous ways. One way to classify them is based on their function, as illustrated in Fig. 1.6. The most common type is fluidic, which uses fluid suction or injection, and are briefly described below. Another class of actuators include moving body inside or on the domain boundary, with the objective to induce local fluid motion. An example is the electrodynamic fluid oscillator used in the classic flat plate experiments [39]. The final category of commonly used active VGs is the plasma actuators, which have gained popularity in the recent years

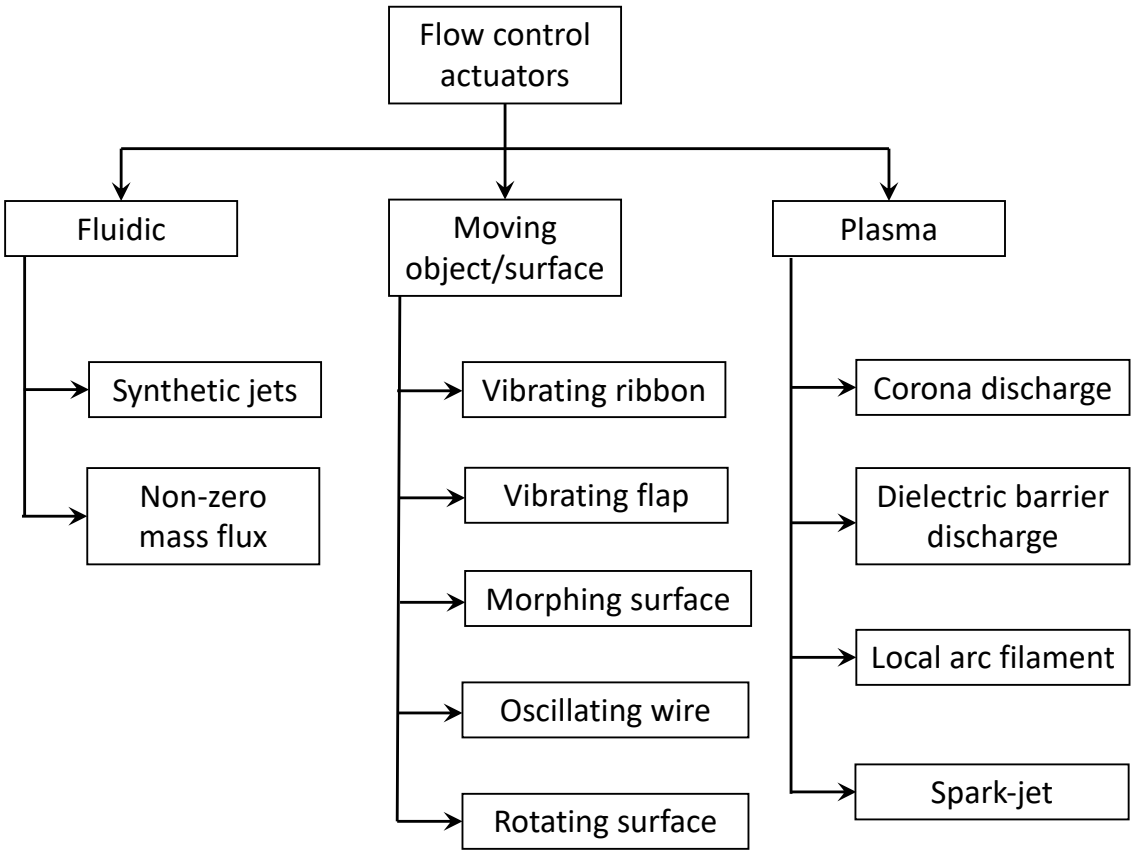

Figure 1.6: A type classification of flow control actuators from Cattafesta *et al.* [4].

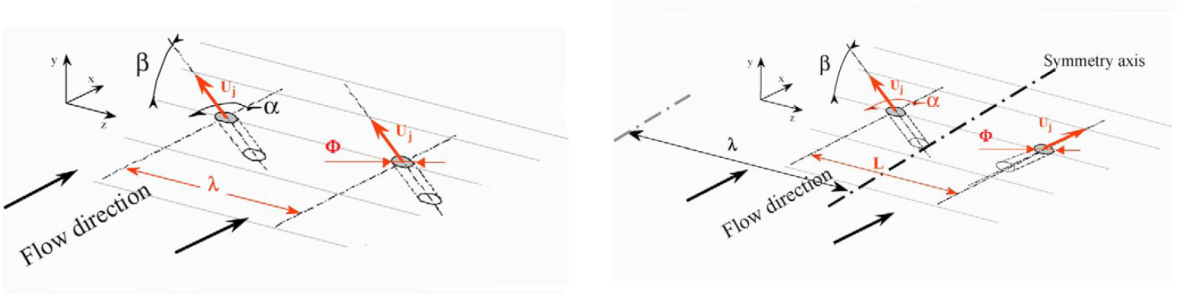

(a) Co-rotating (b) Counter rotating

Figure 1.7: A schematic of synthetic jets from Cuvier [3].

because of their solid-state nature and fast response time.

Within the class of fluidic actuators, round jets are the most commonly used active VGs [40, 41, 42]. Steady jet VGs require a constant supply of power and are not suitable for real-world applications due to their large energy requirements. To overcome this drawback, pulsed jets have been developed [42, 43], which can be used in a co-rotating or counter-

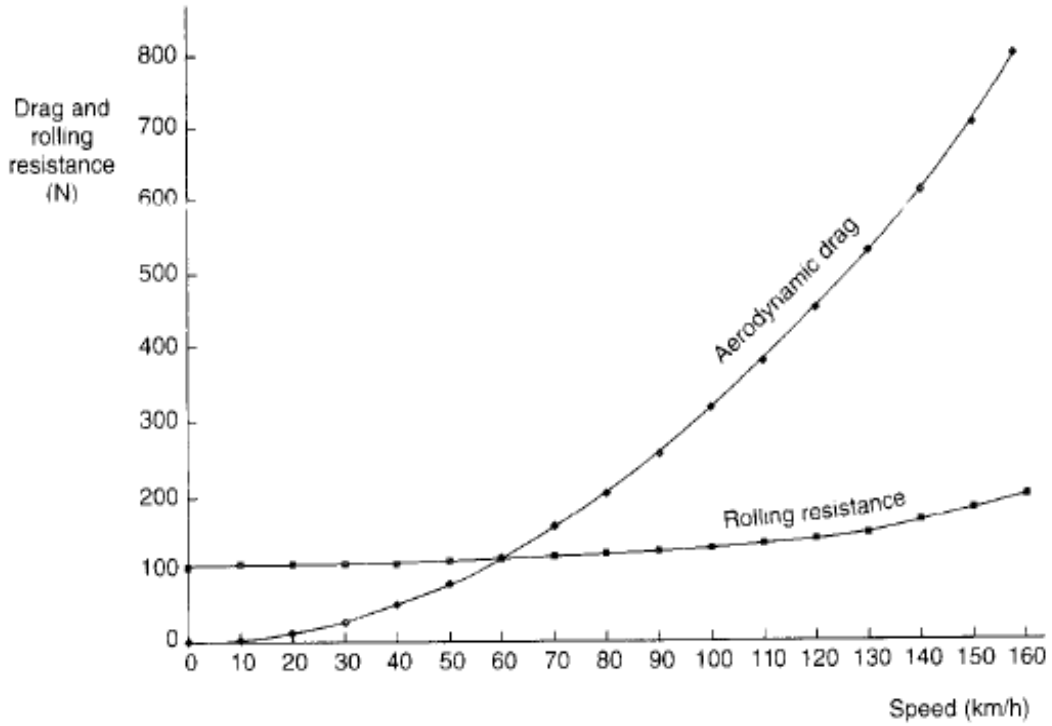

Figure 1.8: Forces acting on an automobile as a function of it's speed from Barnard [5].

rotating configurations, as illustrated in Fig. 1.7. Steady and pulsed jets were initially used in an open loop, without feedback [40, 42]. More recently, closed-loop pulsed jets have been used efficiently to reduce flow separation [44, 45]. The effectiveness of a pulsed jet depends on a number of factors like the jet velocity compared to the free-stream velocity, the jet angle compared to the free-stream velocity, the diameter of the jet, the pulse frequency, the spacing between adjacent jets, etc. [42, 43, 46].

1.5 Flow separation on an automobile

Our work is a part of a larger project with the ultimate goal of reducing the aerodynamic drag acting on road vehicles by manipulating the separated region on the back of the vehicles. Recent data from the Environmental Protection Agency (EPA) reveals that nearly 23% of the total greenhouse gas emissions in the United States come from automobiles [47]. For a typical mid-sized American car, 18% of fuel energy is expended to perform work against

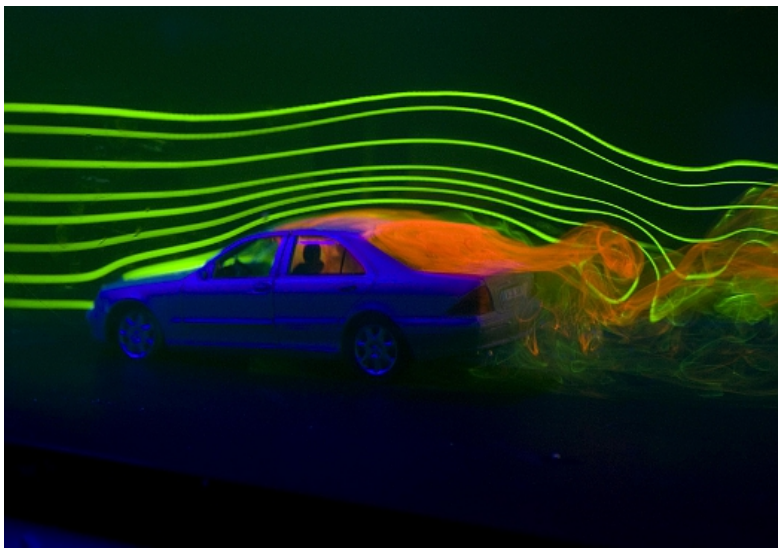

Figure 1.9: Visualization of air-flow separation of the rear end of an automobile. Photo credit: NASA [6].

the aerodynamic drag on an urban schedule, and the number can be as high as 51% on the free-way [48]. Reducing the aerodynamic drag will in turn aid our efforts in mitigating greenhouse gas emissions. Aerodynamic drag is the resistance to the motion of the car by air. If we consider an automobile moving on a freeway there are two main forces acting on the car: (i) rolling resistance acting on the wheels, and (ii) air resistance, i.e., aerodynamic drag. Barnard [5] explain that as the speed of the automobile increases the rolling resistance does not significantly change, while, the aerodynamic drag increases in a quadratic manner, as depicted in Fig. 1.8. This aerodynamic drag acting on the car can be decomposed into two components,

$$\text{Aerodynamic drag} = \text{Pressure drag} + \text{Viscous drag}$$

where pressure drag is the net pressure force acting on the car and viscous drag is the net viscous force acting on the surface of the car, which depends strongly on the viscosity of

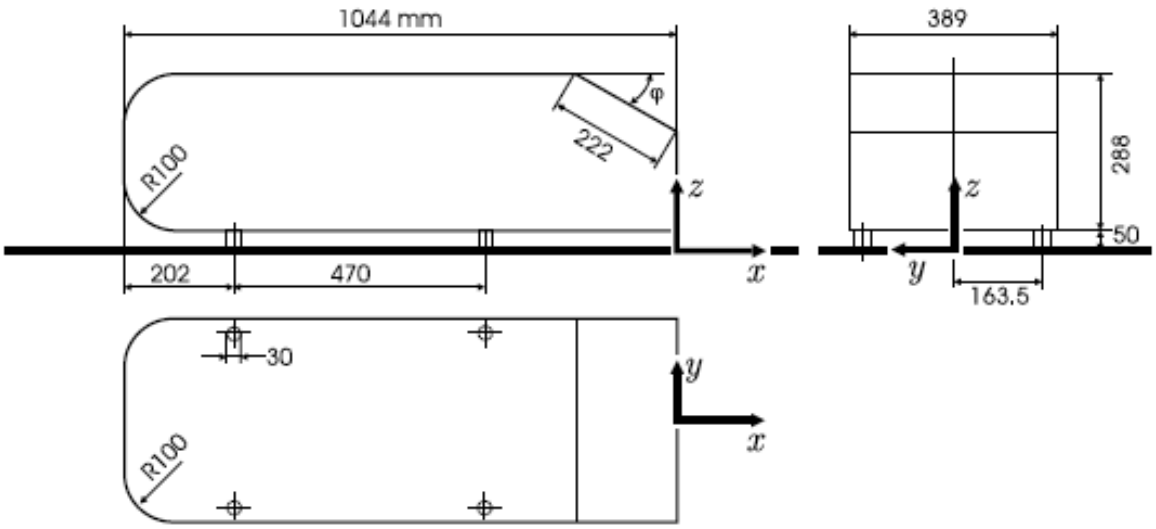

Figure 1.10: Schematic of an Ahmed body from Hinterberger *et al.* [7], © Springer Nature. Reproduced with permission. All rights reserved.

the fluid. Flow separation occurs on the rear end of the automobile, as illustrated in Fig. 1.9. The sudden change in vehicle geometry at the rear end of the roof results in flow separation. Experimental investigation [8] of a simplified model shows that the separated region is characterized by low pressure. The pressure gradient setup along the surface of the vehicle results in a net force opposing its motion. This force is termed as *pressure drag*.

1.6 Ahmed body: a simplified car model

The geometry of road vehicles is complex and highly variable, therefore for the purpose of academic research Ahmed *et al.* [49] proposed a simplified model subsequently referred to as Ahmed body (Fig. 1.10). Amongst other studies, researchers have used this model to understand the complex three dimensional wake formed behind a car [8, 50, 51]. An Ahmed body is essentially a parallelepiped with a slant face at the rear which reproduces basic aerodynamic features of a car. Ahmed *et al.* showed that the strength of the side-edge vortices and the horse-shoe vortices in the separation bubble is mainly determined by the rear slant angle. Beyond a critical slant angle ($\alpha \approx 30^{\circ}$) while keeping all other parameters

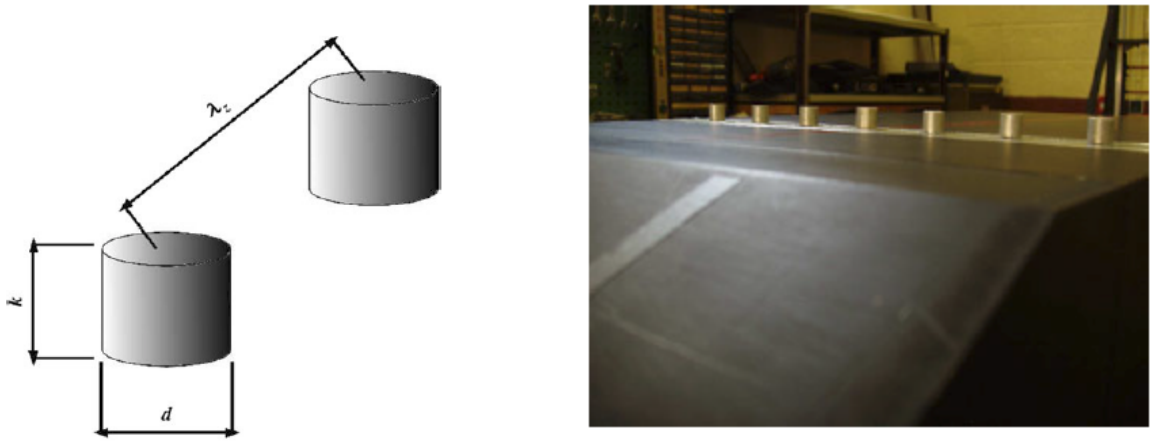

(a) Shape of cylinder VGs with relevant parameters.

(b) Rear view of the cylinder VGs placed on the Ahmed body.

Figure 1.11: From Pujals *et al.* [8], © Springer Nature. Reproduced with permission. All rights reserved.

fixed, pressure drag increases significantly.

The separation of flow from the rear edge creates a strong pressure gradient between the sides and the slant, which leads to the formation of strong counter-rotating vortices from the two upper corners of the slant. Minguez *et al.* [52] performed a LES of flow over an Ahmed body to find that the flow separates from the leading edge of the body front and reattaches after a recirculation bubble on the top-surface. The reattachment is followed by a thickening of the turbulent boundary layer. Minguez *et al.* demonstrated in their simulations that before the flow separates from the rear end of the Ahmed body the turbulent boundary layer is spatially evolving in nature. The quantities investigated and the choice of parameters in our work are influenced by the efforts in reducing pressure drag acting on the rear end of an Ahmed body.

Pujals *et al.* [8] performed an exploratory study to reduce the flow separation on the rear end of an Ahmed body using cylinders as passive VGs with different configurations. The cylinder-shaped VGs and their arrangement on the Ahmed body can be seen in Fig. 1.11a and 1.11b respectively. An experimental study conducted by Pujals *et al.* [53, 8]

using cylinder shaped roughness elements to modify a flat plate turbulent boundary layer at moderate Reynolds number ($Re = U_e\delta^*/\nu = 1000$, where δ^* is the displacement thickness) demonstrated that large-scale, high-speed and low-speed stream-wise coherent structures are formed downstream of the roughness elements. These coherent structures emanate from the horse-shoe vortex formed in front of the cylinder, as illustrated by Fig. 1.12. From the extensive work done on passive VGs by Lin *et al.* [2], we know that strong stream-wise vortices are most effective in entraining momentum from the free stream to the near wall region, and therefore in separation reduction. Pujals *et al.* put this observation to test by investigating the ability of large-scale stream-wise coherent streaks to reduce flow separation on the rear end of the Ahmed body, and then evaluating whether the drag changed [8]. In the most optimal configuration they were able to reduce the total drag coefficient by 10% in which the cylinders were placed at a distance of $4\lambda_z$ to $5\lambda_z$ upstream of the separation line, where λ_z is the distance between adjacent cylinders. In this study the Reynolds number of the TBL on the top surface of an Ahmed body was 20,000, based on the boundary layer thickness and the mean flow velocity. The similarity between the horse-shoe vortices produced by a wall-mounted cylinder and a cube is evident from Fig. 1.12 and 1.13. This is the inspiration behind considering a wall-mounted cube as a potential passive VG.

1.7 Cube as a passive vortex generator

Flow over cube-like obstacles in a turbulent flow have been investigated using experimental and numerical methods. Martinuzzi [54] performed an extensive experimental study of flow over surface-mounted prismatic obstacles of width-to-height ratio (W/H) ranging from 1 to 24 in a fully developed channel flow at Reynolds numbers ranging from 80,000 to 115,000 based on the mean velocity and channel height. They documented the reattachment length and separation length for different ratios, and concluded that for $W/H > 6$ the flow is nominally two dimensional in the middle of the wake. In the experimental study by Hussein et al. [11] the evolution of the spatial dissipation rate from the near field recirculation zone to

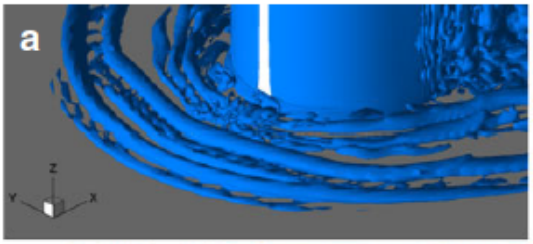

Figure 1.12: Coherent structures of horseshoe vortex around a cylinder in a turbulent boundary layer from Escauriaza *et al.* [9], © Springer Nature. Reproduced with permission. All rights reserved.

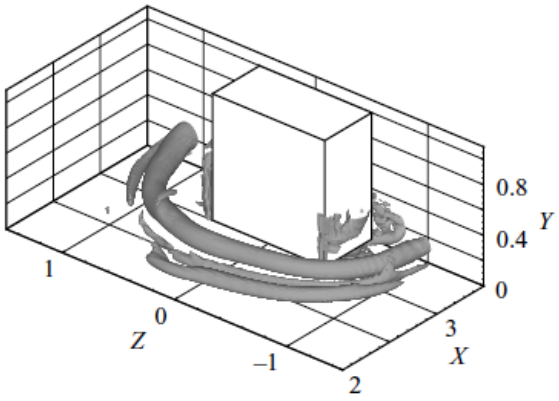

Figure 1.13: Coherent structures of horseshoe vortex around a cube in a channel flow from Yakhot *et al.* [10], © Cambridge University Press. Reproduced with permission. All rights reserved.

the asymptotic wake is examined. A cube of half channel height was placed in a fully developed turbulent channel flow at a Reynolds number of 40,000, based on the cube height and mean channel velocity. The production and dissipation of turbulent kinetic energy (TKE) exhibited a power law decay in the center-plane of the channel.

Numerical studies of flow over a wall-mounted cube placed in a turbulent channel have been performed using the Reynolds Averaged Navier Stokes (RANS) approach with little success [55, 56] because steady RANS simulation neglects the unsteady flow features. Shah et al. [57, 58] and Krajnovic et al. [59, 12] performed Large-Eddy Simulation (LES) of this problem at a Reynolds number of 40,000 based on the mean velocity and cube height. They compared their results with those of Martinuzzi et al. [54] with good agreement. For this problem, the one-equation sub-grid scale model and its variants were reported to perform better than Smagorinsky-type models due their ability to capture back-scatter. Back-scatter is a phenomenon in which TKE flows from smaller scales to larger scales, contrary to an equilibrium turbulent flow.

More recently, Liakos et al. [60] performed a Direct Numerical Simulation (DNS) of steady-state laminar flow over a cube at Reynolds numbers ranging from 1 to 2000 based on

the cube height. The study investigates the onset of dominant flow structures and instability in this flow configuration. It was found that the horse-shoe vortex begins to appear at a Reynolds number of 1267 and the onset of unsteadiness is seen at $Re = 2000$. In another DNS study by Yakhot et al. [61, 10] the inflow was fully developed channel flow, with a Reynolds number of 1870 based on the cube height. They reported that the unsteadiness in the flow is caused by the viscous-inviscid interaction between the horse-shoe vortex and a narrow band of positive vorticity in front of the cube.

Drawing inspiration from the work done by Pujals *et al.* [8], in the successful use of cylinder VGs in reducing drag on the Ahmed body, we propose to use cube-shaped VGs to investigate the basic fluid mechanics associated with blunt VGs. A cube geometry has several advantages: (i) a face-on cube has a single length dimension associated with it, as opposed to two, in case of the cylinder; this reduces the parameter space. (ii) The cube produces similar large stream-wise coherent structures in its wake (horse-shoe vortices), as shown in Fig. 1.13 [59, 12, 61]. These vortices are important flow features associated with VGs. In fact, with a detailed understanding of the fluid mechanics, cubic VGs could be a possible geometry in practice.

As explained in Sec. 1.6, a spatially evolving turbulent boundary layer (SETBL) is formed on the top-surface of the Ahmed body. In light of this knowledge, our proposition to investigate the cube as a passive VG gives rise to three important questions: (i) what should be the height of the cube relative to the boundary layer thickness? (ii) where should we place the cube with reference to the rear end of the Ahmed body? (iii) what should be the spacing between adjacent cubes, if using an array of cubes? We seek to answer these questions by studying a cube placed on a flat plate in isolation, subjected to a SETBL using high-fidelity numerical simulations (large-eddy simulations). This canonical geometry will enable us to identify the fundamental physics underlying SETBL flow over wall-mounted, blunt objects, and possibly generalize to more complicated geometries and settings.

1.8 Objectives of this thesis

The objective of this thesis is to understand the basic fluid mechanics of turbulent flow over (cube-like) VGs in a SETBL using high-fidelity numerical simulations. For the findings to be useful to control TBL separation on the rear end of an Ahmed body, we consider a Reynolds number of 20,000 (Sec. 1.6). There are many numerical approaches to solve the Navier-Stokes equations for turbulent flows, among which the most commonly used approaches are Reynolds Averaged Navier-Stokes (RANS), Large Eddy Simulation (LES) and Direct Numerical Simulation (DNS). The three methods are described in detail in Sec. 2.1, with their advantages and disadvantages. The RANS approach gives a steady-state solution by computing time-averaged flow quantities. RANS simulations are computationally inexpensive. We know that the unsteady vortex shedding observed in flow over cube-like objects has a significant impact on the physics, and steady RANS simulations cannot capture the flow accurately [55, 56]. In a DNS, we solve the Navier-Stokes equations on a fine computational grid, and resolve the entire spectrum of length scales in the turbulent flow. DNS is only feasible for low Reynolds number flows, due to its fine mesh requirement. They are computationally expensive and not a feasible option for the present study, because we are interested in understanding the effect of a number of parameters on the flow physics. Therefore, we use the LES approach in this computational campaign. The computational expense of LES lies between RANS and DNS.

The literature demonstrates that there is a good understanding of the complex flow structures formed around a cube, e.g., the horse-vortex, hair-pin vortices and vortex shedding, for a range of Reynolds numbers [59, 12, 60, 61, 10]. These flow structures are demonstrated in Fig. 1.14. We illustrate the iso-surfaces of the second invariant of the velocity gradient tensor (∇u), known as the Q-criterion. The Q-criterion defines a vortex as a "connected fluid region with a positive second invariant of ∇u" i.e. $Q > 0$. It represents vortices as regions where the vorticity magnitude is greater than the magnitude of rate-of-strain [62]. In Fig. 1.14, the iso-surfaces of $Q-$criterion are colored with vorticity magnitude. In this figure

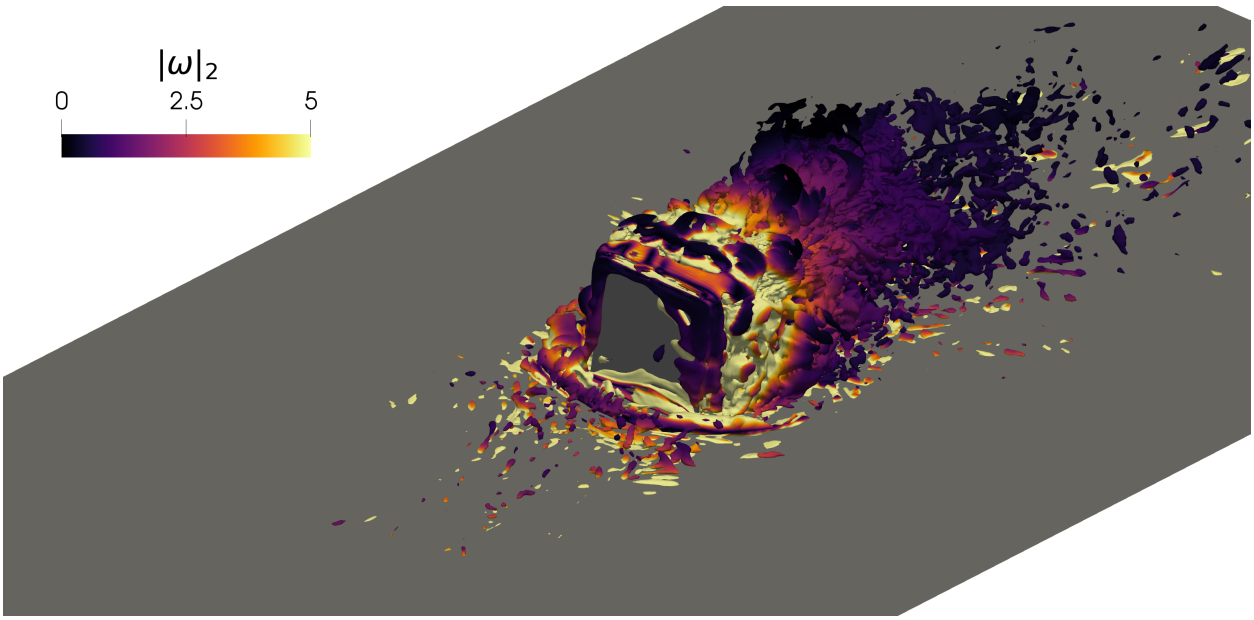

Figure 1.14: Iso-surfaces of $Q-$criterion colored with vorticity magnitude for flow over a wall-mounted cube in a spatially evolving turbulent boundary layer.

we observe a horse-shoe shaped vortex formed in front of the cube, lateral vortices on the side of the cube, and vortex shedding on the top surface of the cube. While various bodies of work [11, 59, 60, 61, 10] have advanced our understanding of physics of turbulent flow over a cube with $h \sim \delta$, these studies have been performed in a fully developed channel. For the physics-based findings from turbulent flow over a cube to be applicable for estimating wind loads on buildings, simulations of flow over vehicles, passive flow control, etc., with the cube height (h) greater than 0.3δ, a SETBL provides a more accurate representation of the turbulent flow physics than that by a fully developed channel flow. Beyond a wall-normal distance of 0.3δ, there are quantifiable differences in the Reynolds stresses between a SETBL and a turbulent channel flow [63], and the effect of these differences on the flow over a cube is not completely understood.

On the other hand a vast body of work investigates atmospheric boundary layer flows over wind farms [64], vegetative canopies [65, 66] and urban environments [67, 68, 69, 70]. These engineering and geophysical examples are distinctly different from smooth wall turbulence, because of the presence of a distribution of obstacles of height, h, which protrude in the

inertial region of the boundary layer [71]. The obstacle height is these studies is typically less than 0.2δ. A 3D array of cubes with $h < 0.2\delta$ has also been investigated to understand the physics of turbulent flow over rough surfaces [72, 73, 74, 75]. From these studies and several others it has been found that the validity of the wall-similarity hypothesis of Townsend [76] — outside the roughness sublayer, turbulent motions are independent of the surface roughness and the interaction between inner and outer layers is weak at high Reynolds numbers — depends on the type of roughness (2D or 3D), and the nature of the turbulent flow (internal or external). For turbulent channel flows with symmetric 2D, or 3D roughness the wall-similarity is satisfactory in the outer region. Whereas, in case of TBLs the wall-similarity hypothesis holds only for 3D roughness elements at high Reynolds numbers. For 2D roughness elements the effects extend in the outer region at both low and high Reynolds numbers regardless of the roughness height.

For the cube to be used as a passive vortex generator, $h > 0.2\delta$, and the problem of understanding the wake characteristics of a cube ($h > 0.2\delta$) placed in a TBL has not garnered significant attention. Furthermore, for our findings to be applicable in controlling flow separation on the rear end of road vehicles, we need to understand the mechanism of TKE entrainment and its distribution in the wake of the cube. In a related work, Hussein *et al.* [11] studied the flow over a cube in fully developed channel flow, and reported the TKE production and dissipation as a function of the stream-wise coordinate in the plane of symmetry of the cube. However, the differences in the Reynolds stresses in a turbulent channel flow and a TBL prevent us from directly employing their findings to the application of interest. Moreover, the TKE distribution in regions away from the center-plane, and its dependence of h/δ ratio have not been examined. For the aforementioned reasons, the objective of our work is two-fold: (i) to investigate the effect of h/δ ratio (for $h > 0.2\delta$) on the TKE distribution in the wake of a cube placed in a SETBL (ii) to understand the effect of varying the spacing between adjacent cubes on the wake characteristics, when a single row of cubes is placed normal to the flow direction.

1.9 Thesis overview

To accomplish the aforementioned objectives we perform high-fidelity large eddy simulations of flow over a cube placed in a TBL. For our findings to be applicable in controlling separated region on the rear end of road vehicles, flow over a cube in a SETBL is considered. We begin our computational campaign by studying a single cube in isolation, and understanding the effect of h/δ ratio on the wake characteristics. Later, we consider a single array of cubes placed in a line normal to the flow direction, and scrutinize the effect of varying the inter-cube spacing on the wake characteristics. The sequential steps we took to achieve our objectives form the basis of the different chapters in my thesis and are summarized below:

1. In Chapter II, the governing equations and numerical approach (large-eddy simulation of the incompressible Navier-Stokes equation) are described. Given that the simulations are conducted using the open source OpenFOAM [77] libraries, we first assess the viability of the code to simulate the problem of interest. In particular, we present our approach to introduce a turbulent boundary layer as an inflow into our domain in the OpenFOAM framework. After evaluating an existing strategy [1], we introduce a novel approach making use of a turbulent flow database and machine-learning.

2. To understand the basic fluid mechanics of a spatially evolving turbulent boundary layer flow over a wall-mounted cube, we present our LES results for cubes of different heights in Chapter III. We observe that size of the wake behind the cube scales with the cube height (h). The center of the horse-shoe vortex is characterized by high levels of TKE production, and the reason for this increase is explained. An important finding of this work is the discovery of the power of decay of TKE per unit area in the near-wake of the cube, and quantifying the dependence of the decay rate on the cube height to boundary layer thickness ratio.

3. To predict the influence of neighboring cubes on each other, we present in Chapter IV results from LES of a line array of cubes, for which the spacing between the cubes

is varied. The periodic arrangement of cubes in the span-wise direction artificially imposes a periodic forcing in the outer region of the TBL. This leads to amplification of large scale coherent structures in the outer region for the case with the smallest spacing. The amplification of these structures results in an increasing TKE in the region in between adjacent cubes. We conclude with Chapter V, highlighting our major contributions and possible avenues for future research.

CHAPTER II

Governing equations and the numerical approach

We perform a computational analysis of flow over a wall-mounted cube in a spatially evolving turbulent boundary layer (SETBL) using Large Eddy Simulations (LES). The purpose of this chapter is to justify the use of LES, present the system of governing equations, and explain the discretization schemes and the boundary conditions employed to perform the simulations. In order to simulate a SETBL we implement an existing physics-based approach, and propose a novel approach to perform the same task. A detailed explanation of the procedure and validation of both these methods in presented in this chapter.

2.1 Large Eddy Simulations

2.1.1 Introduction

A fundamental characteristic of turbulent flows is the presence of a wide spectrum of length and time scales. The amount of energy contained in the fluctuating velocity field in a turbulent flow is quantified by the turbulent kinetic energy (TKE). TKE is distributed in a non-uniform manner across the spectrum of scales. If $V(x,t)$ represents the velocity field as a function of time and space, and $\langle V(x,t)\rangle$ represents the velocity field averaged in time and invariant spatial directions, then,

$$v(x,t) = V(x,t) - \langle V(x,t)\rangle$$

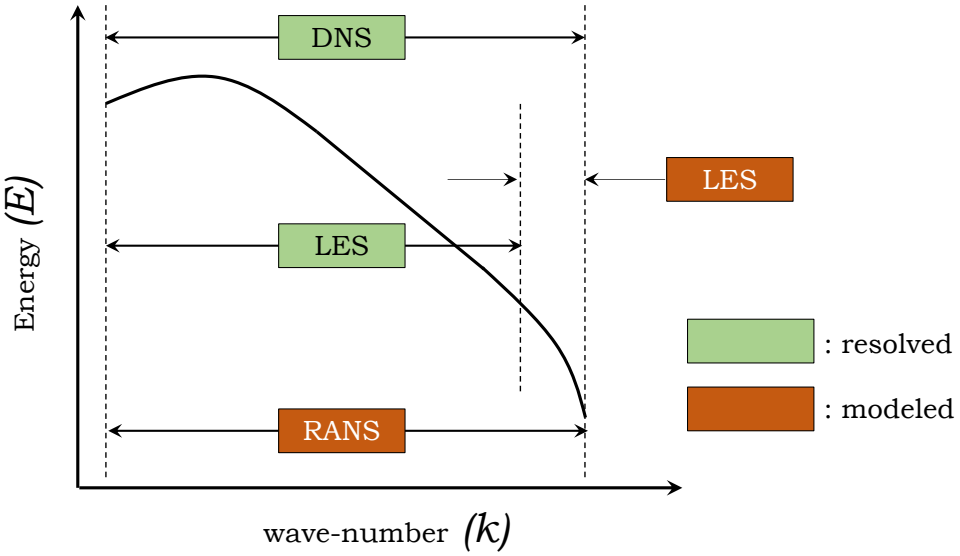

Figure 2.1: Schematic of the one-dimensional turbulent kinetic energy spectrum as a function of wave-number.

where, $v(x,t)$ is the fluctuating velocity field. Turbulent kinetic energy (TKE) is defined as the mean kinetic energy contained in the velocity fluctuation field given by $\frac{1}{2}\langle v_i v_i \rangle$. It remains to be determined how the TKE is distributed among the eddies of different sizes. This is most easily done for *homogeneous turbulence*. A turbulent flow is said to be homogenous if all the statistics are invariant under a shift in position. The distribution of TKE for such a flow is illustrated in the wave-number space in Fig. 2.1. In this figure, larger eddies correspond to smaller wave-numbers and contain greater amount of TKE, whereas smaller eddies correspond to larger wave-numbers and contain less TKE. We will use the TKE energy spectrum for a homogeneous turbulent flow in Fig. 2.1 to explain the three common numerical approaches to simulate turbulent flows.

For a numerical simulation to accurately predict such a turbulent flow it should have zero numerical errors and resolve all the length and time scales. Assuming the numerical framework is accurate, in order to resolve the entire spectrum of scales, we require a computational grid at least as fine as the smallest length scale. A simulation in which the entire spectrum of TKE is resolved using a fine computational grid is called as Direct Numerical

Simulation (DNS), as depicted in Fig. 2.1. As the Reynolds number (Re) of the flow increases the computational cost of DNS increases as $Re^{37/14}$ [78]. The Reynolds number of the flow under consideration in the present work ($Re = 19,600$) is significantly high, and though DNS would be quite expensive, it is not out of reach in the foreseeable future. Moreover, for a large parametric study like the present work, DNS is not a feasible approach. On the other end of the spectrum of methods to simulate turbulent flows is the Reynolds Averaged Navier-Stokes (RANS) approach. In a RANS simulation, we decompose the velocity field into a mean component and a fluctuating component, as given below,

$$V(x,t) = \langle V(x,t) \rangle + v(x,t) \tag{2.1}$$

Using Eq. 2.1, we explicitly calculate the mean flow quantities, and model the effect of the fluctuating component on the mean flow for the entire spectrum. While a RANS simulation is computational inexpensive, the accuracy of the results largely depends on the nature of the turbulent flow, and the accuracy of the RANS model is capturing the effect of the fluctuating component. For flow over a cube in a turbulent boundary layer, the flow is highly unsteady in the region in front of the cube and in its near-wake, and RANS models are known to perform poorly in capturing this unsteadiness [55, 56]. To address the drawbacks of DNS and RANS approaches, the LES methodology was developed. It provides an accurate alternative to DNS for the flow under consideration in the present work. In LES, we explicitly calculate both, the mean and the fluctuating components of the flow for a major part of the spectrum, as demonstrated in Fig. 2.1. This part of the spectrum is referred to as the resolved component. The effect of the remaining or the unresolved part of the spectrum on the resolved component is captured using a LES model. The scale separation between the resolved and the unresolved components is achieved via a filtering operation, explained in the next section.

2.1.2 Filtered Navier-Stokes equations

The main idea behind LES is to filter the turbulent scales into two components, those which can be explicitly resolved using the grid, i.e., resolved or the grid scales, and those which cannot be resolved and need to be modeled, called unresolved or the sub-grid scales (SGS). This decomposition is achieved via a filtering operation. A general filtering operation is defined as,

$$\bar{f}(x_i) = \int_{\Omega} f(x_i')G(x_i, x_i')dx_i' \tag{2.2}$$

where G is the filter function and Ω is the entire flow domain. In the present work, a top-hat filter with filter function $G = (1/\Delta)H(\frac{1}{2}\Delta - |x - x'|)$ is used, where $H(x)$ is the Heaviside function. The filter width Δ is defined as $\Delta = (\Delta_1\Delta_2\Delta_3)^{1/3}$, where Δ_i are the computational mesh sizes in the three coordinate directions.

The velocity field has the following decomposition,

$$u(x,t) = \overline{u}(x,t) + u'(x,t) \tag{2.3}$$

where, $\overline{u}(x,t)$ is the filtered velocity, and $u'(x,t)$ is the SGS velocity field. Despite the apparent similarities with Reynolds decomposition in Eq. 2.1, $\overline{u}(x,t)$ is a random field, and thus (in general) the filtered residual is not zero. The convolution of the filter function with the Navier-Stokes equations gives the filtered Navier-Stokes equations,

$$\begin{aligned} \frac{\partial \bar{u}_i}{\partial x_i} &= 0 \\ \frac{\partial \bar{u}_i}{\partial t} + \frac{\partial(\bar{u}_i\bar{u}_j)}{\partial x_j} &= -\frac{\partial \bar{p}}{\partial x_i} + \nu\frac{\partial^2 \bar{u}_i}{\partial x_j^2} - \frac{\partial \tau_{ij}}{\partial x_j} \end{aligned} \tag{2.4}$$

Eq. 2.4 is a set of four couple non-linear equations, which include one continuity equation and three momentum equations for the three coordinate directions. This set is referred to as the *filtered Navier-Stokes* equations.

2.1.3 Dynamic k-equation model

In a turbulent flow energy cascades from the resolved, large-scales to the smallest scales at which kinetic energy dissipates [79]. If one does not explicitly solve for the smallest scales, as in LES, kinetic energy eventually accumulates due to inadequate dissipation. To address this inadequacy, the effect of the SGS is taken into account through the SGS stress tensor, $\tau_{ij} = \overline{u_i u_j} - \bar{u}_i \bar{u}_j$. The SGS stress contains the unknown, second order term $\overline{u_i u_j}$. Without an explicit equation for the unknown term, the filtered Navier-Stokes equations do not form a closed system. Different methods have been developed to close the system of Eq. 2.4, and a detailed review of many different methods can be found in Meneveau *et al.* [80]. In the present work we use the *dynamic k-equation* model [81] in which we solve an additional transport equation for the SGS kinetic energy (k). The reasons to use this specific model is its ability to predict *back-scatter*. Back-scatter is a phenomenon in which kinetic energy flows from the unresolved small scales to the resolved scales. Back-scatter has been observed in flow over a wall-mounted by Yakhot *et al.* [61].

In the dynamic k-equation model, the SGS stress tensor is given by,

$$\begin{aligned} \tau_{ij} &= -2\nu_T \overline{S}_{ij} + \frac{1}{3}\delta_{ij}\tau_{kk} \\ \nu_T &= c_\nu k^{1/2} \overline{\Delta} \\ \overline{S}_{ij} &= \frac{1}{2}\left(\frac{\partial \bar{u}_i}{\partial x_j} + \frac{\partial \bar{u}_j}{\partial x_i}\right) \end{aligned} \tag{2.5}$$

where, $\overline{\Delta} = (\Delta_1 \Delta_2 \Delta_3)^{1/3}$ is the average grid spacing, and $k = \frac{1}{2}\left(\overline{u_i^2} - \overline{u_i}^2\right)$ is the SGS kinetic energy. In the dynamic k-equation model, the transport equation for k is given by Eq. 2.6,

$$\frac{\partial k}{\partial t} + \overline{u_i}\frac{\partial k}{\partial x_i} = -\tau_{ij}\frac{\overline{u_i}}{x_j} - \epsilon + \frac{\partial}{\partial x_i}\left(\nu_T \frac{\partial k}{\partial x_i}\right) \tag{2.6}$$

In Eq. 2.6, the dissipation rate (ϵ) is given by,

$$\epsilon = c_\epsilon \frac{k}{\overline{\Delta}} \tag{2.7}$$

An important feature of this model is that no assumption of local equilibrium between the SGS energy production and dissipation rate has been made. Therefore, this model can take into account non-local and history effects which are completely neglected in the algebraic models.

In Eq. 2.5, $\overline{S_{ij}}$ is the resolved strain rate tensor and $\left|\overline{S}\right| = (2\overline{S}_{ij}\overline{S}_{ij})^{1/2}$. The coefficients c_ν in Eq. 2.5 and c_ϵ in Eq. 2.7 are determined by a dynamic procedure [82]. In the dynamic modeling approach, a mathematical identity between the stresses resolved at the grid scale filter $\overline{\Delta}$ and a test filter $\widehat{\Delta}$ (typically, $\widehat{\Delta} = 2\overline{\Delta}$) is used to determine the coefficients.

$$\begin{aligned} c_\nu &= \frac{1}{2}\frac{L_{ij}M_{ij}}{M_{ij}M_{ij}} \text{ where, } L_{ij} = \widehat{\overline{u_i}\overline{u_i}} - \widehat{\overline{u_i}}\,\widehat{\overline{u_j}} \\ M_{ij} &= -\left(\widehat{\Delta}K^{1/2}\widehat{\overline{S_{ij}}} - \overline{\Delta}\widehat{k^{1/2}\overline{S_{ij}}}\right), \text{ and } K = L_{ii}/2 + \widehat{k} \end{aligned} \tag{2.8}$$

$$c_\epsilon = \frac{F}{G} \text{ where, } F = \nu\left(\widehat{\frac{\partial\overline{u}_i}{\partial x_j}\frac{\partial\overline{u}_i}{\partial x_j}} - \frac{\partial\widehat{\overline{u}}_i}{\partial x_j}\frac{\partial\widehat{\overline{u}}_i}{\partial x_j}\right), \text{ and } G = \left(\frac{K^{1/2}}{\widehat{\Delta}} - \frac{\widehat{k^{1/2}}}{\overline{\Delta}}\right) \tag{2.9}$$

In Eq. 2.8 and Eq. 2.9, $\widehat{(\ )}$ represents quantities at the test filter scale, and $\overline{(\ )}$ represents quantities at the grid filter scale. In the present work, the size of the test filter is twice that of the grid filter. The filtered Navier-Stokes equations (Eq. 2.4), transport equation for SGS kinetic energy (Eq. 2.6), and the coefficients (Eq. 2.8 and 2.9) form a closed system. This system of equations is solved simultaneously using the Finite Volume Method (FVM) in the open-source software OpenFOAM®[77], with the discretization schemes described in Sec. 2.2.

2.2 Discretization schemes

OpenFOAM [77] is an open-source software with the capability of simulating a wide range of flow processes. In the present study, we use the LES capabilities of OpenFOAM version 4.1 to solve the governing equations described in Sec. 2.1.2 and 2.1.3. Numerical schemes implemented in OpenFOAM are 1^{st} and 2^{nd} order accurate. A detailed validation of the numerical methods and RANS models in OpenFOAM can be found in Robertson *et al.* [83]. Cao *et al.* [84] validated the LES models and discretization schemes for separated flow over a square cylinder, and concluded that the "LUST" (Linear Upwind Stabilized Transport) and "linearUpwind" schemes for the convective term give good agreement of the mean and RMS quantities with experimental data.

The coupled non-linear LES equations are solved on a structured collocated grid using a Finite Volume Method (FVM) in which all the variables (three components of velocity, pressure, and LES terms) are stored at the cell centers. The system of couple equations is solved using the PIMPLE algorithm. PIMPLE is a combination of PISO (Pressure Implicit with Splitting of Operator) [85] and SIMPLE (Semi-Implicit Method for Pressure-Linked Equations) [86] algorithms, which follow the general procedure of momentum prediction, pressure solution and momentum correction. The detailed procedure is available in Robertson *et al.* [83]. An implicit backwards scheme is used to discretize the unsteady term. For illustration, consider an unsteady PDE of a scalar variable "ϕ". An implicit backwards time marching scheme used for the unsteady term $\frac{\partial \phi}{\partial t}$ gives,

$$\frac{\partial \phi}{\partial t} = \frac{3\phi^{n+1} - 4\phi^{n} + \phi^{n-1}}{2\Delta t} \tag{2.10}$$

The time marching procedure in Eq. 2.10 is used for three components of velocity in our work. The time step (Δt) is variable, determined by the *Courant-Friedrichs-Lewy* (CFL) condition (Eq. 2.11).

$$C = \Delta t \sum_{i=1}^{n} \frac{u_{x_i}}{\Delta x_i} \leq C_{max} \tag{2.11}$$

where, u_{xi} is the velocity in the x_i direction, Δx_i is the grid spacing in the x_i direction and C_{max} is the maximum CFL number prescribed in the code, which in the present work is set to 1. The implicit time marching scheme is preferred over an explicit scheme to ensure stability. The scheme is unconditionally stable and the time-step size (Δt) is not restricted by the CFL number, however, we limit Δt by a CFL number of 1 to ensure that the numerical errors accumulated by the time-marching scheme are of the same order of magnitude as those accumulated by the spatial discretization scheme.

The pressure and the viscous terms are discretized by the 2^{nd} order central scheme [83]. The convective term is discretized using the LUST scheme, which is a combination of the central differencing scheme and the linear upwind scheme with the weighting factors of 0.75 and 0.25 respectively. By Gauss's divergence theorem, the convective terms are integrated over the cell volume (denoted by V_p) and expressed as a sum of fluxes evaluated on each face of the cell, as shown in Eq. 2.12.

$$\int_{V_p} \nabla \cdot (u\phi_p) = \sum_{f} S_f \cdot (u\phi)_f \tag{2.12}$$

where, u is the cell-center velocity, ϕ_p is the flux at the cell-center, ϕ_f is the flux at the cell-face and S_f is the normal vector of the corresponding cell-face. ϕ_f is interpolated using Eq. 2.13 in a central differencing scheme.

$$\phi_f = f_x \phi_P + (1 - f_x)\phi_E \tag{2.13}$$

where, the factor $f_x = \overline{fE}/\overline{PE}$, $\overline{fE}$ is the distance between face f and cell-center E, and $\overline{PE}$ is the distance between cell-centers P and E. Mittal *et al.* [87] report, a drawback of the second order central scheme is that the simulations are sensitive to the numerical factors such as grid discontinuities and outflow boundary conditions, and thus, grids and boundary

conditions have to designed with extreme care. To overcome this problem, the LUST scheme adds weighting towards the upstream contribution. In a the linear upwind scheme, the face flux ϕ_f is determined by both, the value, and the cell gradient of ϕ in the upwind cell, as shown in Eq. 2.14.

$$\phi_f = \begin{cases} \phi_P + (\nabla\phi_P) \cdot d_f \text{ for } u > 0 \\ \phi_E + (\nabla\phi_E) \cdot d_f \text{ for } u < 0 \end{cases} \tag{2.14}$$

2.3 Boundary conditions and initial conditions

The flow configuration of interest in this study consists of a cube placed on a flat plate in a spatially evolving turbulent boundary layer (SETBL). In all the simulations over the cube, the top-wall is treated as a slip (or no-stress) wall. If x, y and z represent the stream-wise, wall-normal and span-wise directions, and u, v and w represent the velocity components in those directions respectively, then the no-stress boundary condition is given by,

$$v = 0, \quad \frac{\partial u}{\partial y} = \frac{\partial w}{\partial y} = 0, \text{ and } \frac{\partial p}{\partial y} = 0 \tag{2.15}$$

where, p is the pressure field. The outflow plane is treated with the standard implementation of the *zero-gradient* boundary condition in OpenFOAM, for velocity and pressure,

$$\frac{\partial u}{\partial x} = \frac{\partial v}{\partial x} = \frac{\partial w}{\partial x} = 0, \text{ and } \frac{\partial p}{\partial x} = 0 \tag{2.16}$$

The side-walls are treated differently for the cases with single and multiple cubes. In case of the single cube, we deploy a slip-wall boundary condition as described in Eq. 2.15, whereas in case of multiple cubes we use periodic boundary conditions on the side-walls. The initial condition of velocity is zero everywhere inside the domain for the coarse mesh, whereas, for the medium and fine mesh simulations the final instantaneous velocity field from the immediate lower resolution simulation is mapped on the grid and used as an initial guess

for the velocity field. An initial value of 1% of the free-stream kinetic energy ($\frac{1}{2}U_\infty^2$) if used for turbulent kinetic energy (k) inside all the cells. In order to achieve a SETBL, a special type of time-varying boundary condition needs to be used for the velocity field at the inflow boundary, described in detail is Sec. 2.4.

2.4 Inflow boundary condition

2.4.1 Introduction

The problem in LES of wall-bounded flows is prescribing fluctuations at the inlet which are not only time-varying and random, but also, preserve the structure of near-wall turbulence in an average sense. Furthermore, the appropriate amount of kinetic energy distributed over the appropriate length scales must be provided at the inlet. Inflow boundary conditions for spatially evolving turbulent boundary layer (SETBL) can be classified in two categories, namely *rescale and recycle* and *synthetic inflow* approaches. A thorough review of these methods can be found in Tabor *et al.* [88]. The two approaches are briefly described below:

1. The most accurate technique to impose the inlet boundary conditions for a LES is to obtain inflow data from a precursor simulation. The precursor simulation typically has a periodic streamwise boundary condition. The data from plane located at an appropriate distance from the inlet boundary in the precursor simulation are sampled at every time-step and stored. This stored data are then carefully modified to satisfy the inflow boundary layer properties, and used as time-varying inflow boundary condition for the main simulation. The inflow contains the exact large scale eddies of the flow and there is no or little transition downstream of the inlet. This technique however has two major drawbacks. Firstly, it is restricted to simple cases where the flow at the inlet of the computational domain can be regarded as a fully developed turbulent flow or SETBL. Secondly, it entails significant computational and storage costs.

2. The overcome these drawbacks researchers have pursued an alternate route of prescrib-

ing synthetic turbulence at the inlet. This method was first implemented by Le [1] to simulate a turbulent boundary layer flow over a backward facing step. The basic idea in this class of methods is to superimpose random fluctuations on top of a mean velocity profile. The prescribed time-varying inflow velocity field does not obey Navier-Stokes equations, and therefore requires a transition length for the flow to develop into a realistic TBL. The most critical part is prescribing fluctuations that possess the right spatial and temporal correlations to minimize the transition length. In order to make it more realistic we superimpose a fluctuation field satisfying different statistics like the turbulent kinetic energy, dissipation rate and in some cases the full Reynolds stress tensor. There are a variety of approaches to prescribe the fluctuation field, which include Fourier techniques [89, 90], proper orthogonal decomposition based methods [91], digital filter based methods [92], and methods based on Lagrangian treatment of vortices [93, 94]. In the present work we use the same method as Le [1] to obtain a SETBL, described in Sec. 2.4.2, and propose a novel approach based on machine-learning to address the same problem in Sec. 2.5

2.4.2 Conventional approach of Le [1]

The basic idea is to superimpose random fluctuations on a mean turbulent velocity profile [1], as outlined below:

1. Prescribe energy spectrum for TKE.

$$E(k) = u_{rms}^2 16\sqrt{\frac{2}{\pi}}\frac{k^4}{k_p^5}exp(-2k^2/k_p^2) \tag{2.17}$$

   where, k_p is the most energetic wavenumber. In the present work, we set $k_p = 4$, and $u_{rms} = 0.01U_\infty$, where U_∞ is the free-stream velocity.

2. Compute $\widehat{E}(\boldsymbol{k})$, the kinetic energy at a given wavenumber vector, $\boldsymbol{k}$, from the prescribed spectrum $E(k)$ as follows.

The energy spectrum $E(k)$ is defined as,

$$E(k) = \sum_{k \leqslant |\boldsymbol{k}| < k+1} \widehat{E}(\boldsymbol{k}), \tag{2.18}$$

where,

$$\widehat{E}(\boldsymbol{k}) = \langle \widehat{u}_i^*(\boldsymbol{k}) \widehat{u}_i(\boldsymbol{k}) \rangle / 2 \tag{2.19}$$

and $\widehat{u}_i(\boldsymbol{k}, t)$ is the Fourier coefficient of $u_i'(y, z, t)$ and $\widehat{u}_i^*(\boldsymbol{k}, t)$ is its complex conjugate. Thus $\widehat{E}(\boldsymbol{k})$ can be computed from the prescribed $E(k)$ as,

$$\widehat{E}(\boldsymbol{k}) = E(k)/Z(k) \tag{2.20}$$

where $Z(k)$ is the number of Fourier modes at the wave number k,

$$Z(k) = \sum_{k \leqslant |\boldsymbol{k}| < k+1} 1 \tag{2.21}$$

3. Compute the instantaneous $\widehat{u}_i(\boldsymbol{k}, t)$ at every time step from

$$\widehat{u}_i(\boldsymbol{k}, t) = [\widehat{E}(\boldsymbol{k})]^{1/2} exp[\mathrm{i}\Phi_i(\boldsymbol{k}, t)] \tag{2.22}$$

where Φ_i is a random phase angle and $\mathrm{i} = \sqrt{-1}$.

4. Prescribe profiles for the velocity fluctuation auto-correlations, $\langle u_1' \rangle$, $\langle u_2' \rangle$, $\langle u_3' \rangle$, and cross-correlation $\langle u_1' u_2' \rangle$. In our simulations we use fluctuation correlation profiles from DNS of SETBL over a flat plate by Wu *et al.* [95].

5. In order to ensure that $\langle u_1' u_2' \rangle$ does not vanish, we rotate the flow coordinates $[x, y]$

by an angle θ_p so that they coincide with the principal coordinates $[\tilde{x}, \tilde{y}]$, where the corresponding velocities $\tilde{u}_1'$ and $\tilde{u}_2'$ are uncorrelated, i.e. $\langle u_1' u_2' \rangle = 0$.

$$\theta_p = \frac{1}{2} tan^{-1} \left[\frac{2\langle u_1' u_2' \rangle}{\langle u_2'^2 \rangle - \langle u_1'^2 \rangle} \right] \tag{2.23}$$

Compute $\langle (u_1')^2 \rangle$ and $\langle (u_2')^2 \rangle$ in the principal coordinates as

$$\begin{aligned} \langle (u_1')^2 \rangle &= \frac{\langle u_1'^2 \rangle cos^2\theta_p - \langle u_2'^2 \rangle sin^2\theta_p}{cos^2\theta_p - sin^2\theta_p} \\ \langle (u_2')^2 \rangle &= \frac{\langle u_2'^2 \rangle cos^2\theta_p - \langle u_1'^2 \rangle sin^2\theta_p}{cos^2\theta_p - sin^2\theta_p} \end{aligned} \tag{2.24}$$

Note that since no rotation is required for u_3', the profile is identical to the prescribed $\langle u_3'^2 \rangle$.

6. Compute at every time step, the inverse Fourier transform of $\widehat{u}_i(k_y, k_z, \omega)$ in the k_y direction to obtain $\widehat{u}_i(y, k_z, \omega)$. Then evaluate the mean-square velocity correlation

$$\overline{u_i'^2}(y) = \sum_{k_z=-N_z/2+1}^{N_z/2} \sum_{\omega=-N_t/2+1}^{N_t/2} \widehat{u}_i(y, k_z, \omega) \widehat{u}_i^*(y, k_z, \omega) \tag{2.25}$$

to compute the ratio $r_i(y)$ of the mean squares as

$$r_i(y) = \frac{\langle (\tilde{u}_i')^2 \rangle (y)}{\overline{u_i'^2}(y)} \tag{2.26}$$

7. Compute at every time step, the inverse Fourier transform of $\widehat{u}_i(y, k_z, \omega)$ in the k_z direction, and sum the result over all the frequencies ω to obtain $\tilde{u}_i'(y, z, t)$. Then

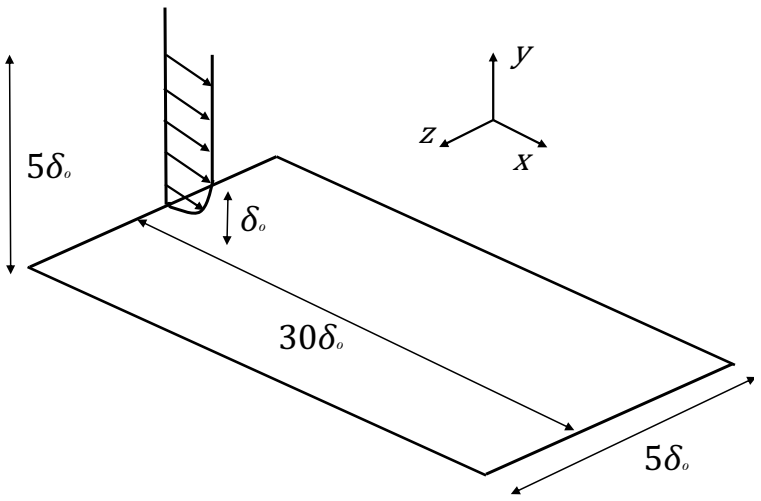

Figure 2.2: Flow configuration for validation of the inflow generator technique.

multiply $\tilde{u}_i'(y,z,t)$ by $\sqrt{r_i(y)}$ so that the mean -square of the product matches $\langle(\tilde{u}_i')^2\rangle(y)$ obtained from Eq. 2.24.

8. Rotate $\tilde{u}_1'$ and $\tilde{u}_2'$ back to u_1' and u_2' in the flow coordinates $[x,y]$ using Eq. 2.27

$$\begin{aligned} u_1' &= \tilde{u}_1' cos\theta_p + \tilde{u}_2' sin\theta_p \\ u_2' &= -\tilde{u}_1' sin\theta_p + \tilde{u}_2' cos\theta_p \end{aligned} \tag{2.27}$$

Our implementation of the approach of Le [1] into OpenFOAM is validated by simulating a SETBL on a flat plate at a inlet Reynolds number of 7000, based on the free-stream velocity and inlet boundary layer thickness. The parameters of the simulation were chosen to have a fair comparison with the DNS study of Ferrante *et al.* [96]. The schematic of the case setup is as shown in Fig. 2.2.

The domain is $30\delta_o$ long, 5 δ_o wide and $5\delta_o$ high, where δ_o is the boundary layer thickness at the inlet. The corresponding Reynolds number based on the friction velocity at the inlet is $Re_\tau = \frac{u_\tau \delta_o}{\nu} = 395$, while Reynolds number based on the momentum thickness at the inlet is $Re_\theta = \frac{U_\infty \theta}{\nu} = 1050$. The computational grid has uniform spacing in the stream-wise (x) and the span-wise (z) directions, whereas it is non-uniform in the wall-normal direction,

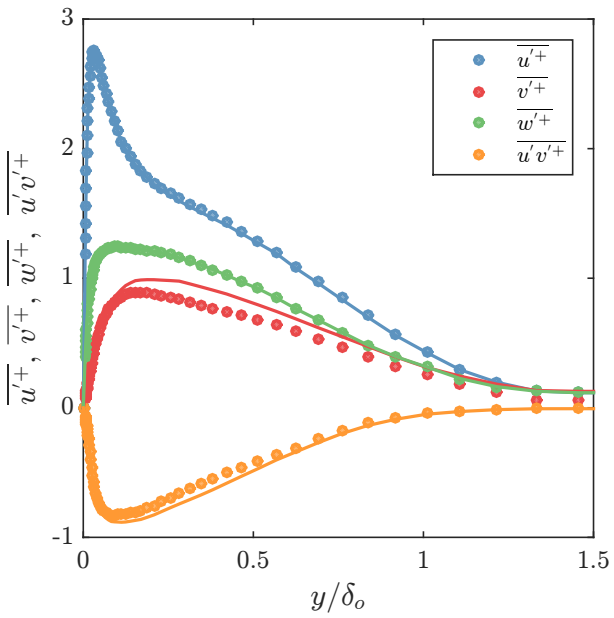

Figure 2.3: Span-wise average of Reynolds stress profiles at the inlet. Solid lines: DNS results of [95]; dots: our implementation of the conventional synthetic inflow method.

with a hyperbolic tangent stretching. The grid size close to the bottom-wall in wall units ($\Delta^+ = \frac{\Delta u_\tau}{\nu}$) is 30, 1 and 20 in x, y and z directions respectively.

After following the procedure described above we obtain a $[y, z]$ plane of velocity fluctuation values which vary with every time step. These fluctuations are superimposed on the mean turbulent boundary layer velocity profile given by "law of the wall" [97]. For any given time-step the span-wise average of the Reynolds stress profiles is presented in Fig. 2.3. At the inlet plane there is excellent agreement in the prescribed fluctuation field and the DNS profiles [95].

In Fig. 2.4a we compare the evolution of the turbulent boundary layer thickness as a function of the stream-wise coordinate with DNS results from Ferrante *et al.* [96]. The velocity profiles are averaged in time and the span-wise direction to calculate the boundary layer thickness (99 $\%U_\infty$). We observe that after an initial transition length of approximately $12\delta_o$ there is good agreement with DNS data. The transition length is similar to that observed by Le [1] ($\sim 10\delta_o$ at $Re_\theta = 670$).

If we observe the mean velocity profiles in Fig. 2.4b at different stream-wise locations,

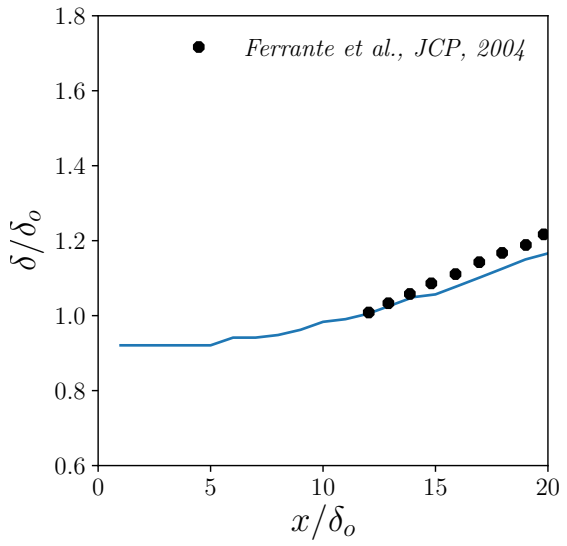

(a) Normalized boundary layer thickness (δ) vs. normalized streamwise coordinate (x)

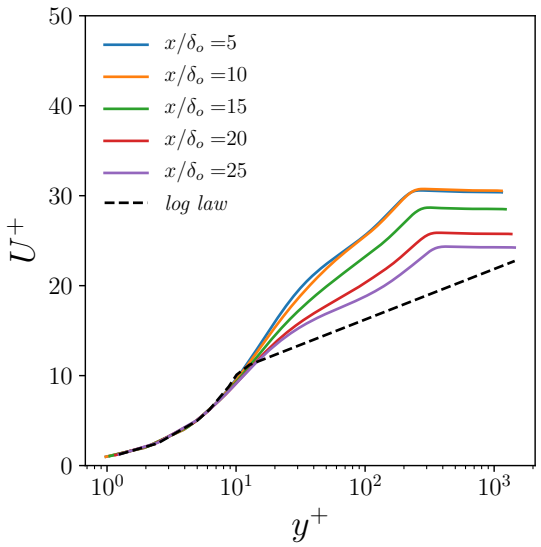

(b) Semi-log plot of mean velocity vs. wall-normal distance in wall units at different stream-wise locations

Figure 2.4: Mean quantities averaged in time and span-wise direction.

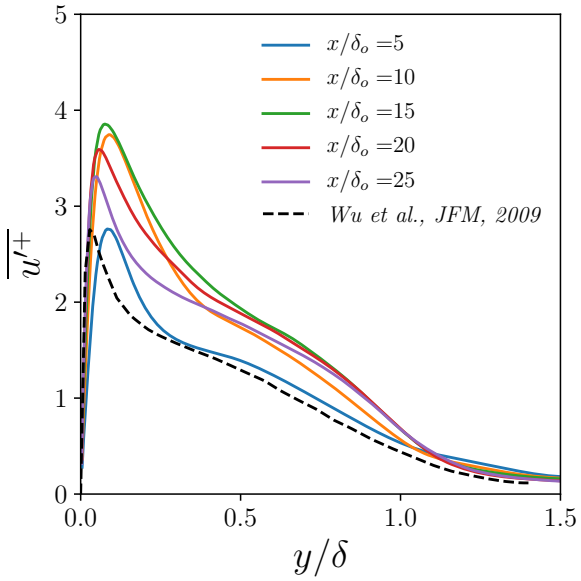

(a) $xx-$component

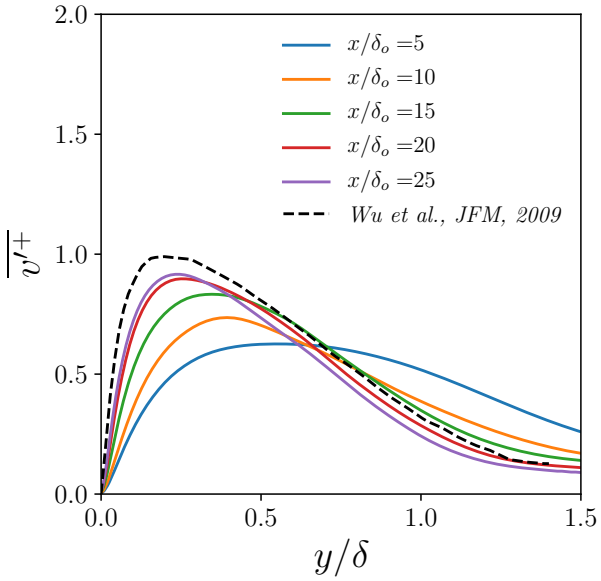

(b) $xx-$component

Figure 2.5: Reynolds stress profiles averaged in time and span-wise direction at different stream-wise locations.

there is small deviation of the converged profiles from the law of the wall. The velocity profiles and wall-normal distance are expressed in wall coordinates ($U^+ = U/u_\tau$ and $y^+ =$

yu_τ/ν). Le [1] observed similar deviations and attributed them to the inaccurate prediction of friction velocity u_τ, however, our results demonstrate excellent agreement in the buffer region ($y^+ < 10$). Therefore, we believe these differences originate from a favorable pressure gradient (FPG) in the stream-wise direction [98]. Although, it would be ideal to simulate a SETBL with zero pressure gradient in the stream-wise direction, it is impossible to achieve those conditions even with the most carefully configured DNS, as explained by Wu *et al.* [95]. Our simulation profiles approach the log-law behavior as we move along the stream-wise direction.

In Fig. 2.5a and 2.5b we present the $xx-$ and $xy-$component of the Reynolds stress averaged in time and the span-wise direction at different stream-wise locations. The Reynolds stresses and the wall-normal distance are expressed in wall-units ($\overline{u'^{2+}} = \overline{u'^2}/u_\tau^2$, $\overline{u'v'}^+ = \overline{u'v'}/u_\tau^2$ and $y^+ = yu_\tau/\nu$). The DNS result from Wu *et al.* [95] has a momentum thickness based Reynolds number ($Re_\theta = U_\infty\theta/\nu$) of 900, whereas in our simulations Re_θ varies from 1050 to 1300. We know from prior research [99, 95] that the Reynolds stresses do not exhibit a universal scaling in inner coordinates especially in the logarithmic region, therefore we do not expect our simulation results to match exactly with the DNS profiles. The near-wall region shows excellent agreement. However, there are small discrepancies in the logarithmic region. From the behavior of the mean and turbulence quantities in Fig. 2.4 and 2.5 we are confident that we can simulate a SETBL with reasonable accuracy with our implementation of the physics-based approach of Le [1].

2.5 Machine learning approach

We present a novel approach similar to the rescale and recycle methods. The motivation to pursue this novel approach is to address the drawbacks of existing rescale and recycle methods. The current implementation of our method does not produce a realistic TBL, and we highlight the reasons for poor agreement with DNS results. Finally, we propose a modified approach to address the shortcomings of the current implementation. There are

three common approaches to implement the rescale and recycle procedure:

1. Perform a precursor simulation and store a library of velocity profiles [100]. Modify the stored velocity profiles and use them at the inflow boundary of the main simulation.

2. Run an auxiliary simulation simultaneously with the main simulation and map velocity profiles from the auxiliary simulation to the inlet plane of the main simulation [96, 101]

3. Modify and map velocity profiles from a downstream plane of the same simulation to the inlet plane [102].

In these three approaches we have to either create a massive storage library of velocity profiles or significantly modify the flow solver to synchronize the main simulation with the auxiliary simulation. We present a technique that circumvents both these drawbacks. In our approach we leverage the *kernel-density estimation* (KDE) technique [103] to learn the *probability density function* (PDF) of the velocity fluctuations from a precursor simulation, and instead of storing a library of velocity profiles we only store the learned models. Then we use the library of stored models to generate a time-varying inflow field for any other simulation. This techniques does not require major modifications to the flow solver, except sampling fluctuations from a known PDF.

2.5.1 Method

The fundamental idea behind our machine learning approach is to learn the prior PDFs from training datasets. The learned PDFs are then used to generate time-varying velocity fluctuation fields. In our approach we learn the PDF of the fluctuation field obtained from the precursor simulation as a function of the wall-normal coordinate. We know that the Reynolds stresses when expressed in wall units exhibit self-similar behavior, at least over a wide-range of Reynolds numbers. Therefore, we express the fluctuation field from the precursor simulation in wall-units to train the PDFs. Our hypothesis is that the learned PDFs can be used to generate fluctuation fields for the main simulation by scaling the values

from wall coordinates to physical coordinates. Our proposed procedure is described in detail below for the $x-$component of velocity fluctuation field (the same steps are followed for the y and z components):

1. Using the physics-based approach described in Sec. 2.4.2, a SETBL on a flat plate a precursor simulation is performed to produce training data. Sample instantaneous velocity profiles from the precursor simulation after a transition length of $12\delta_o$ at every time step, where δ_o is the boundary layer thickness at the inflow boundary.

2. The mean velocity profile is calculated by averaging the instantaneous velocity in time. Time-averaged velocity profile are then averaged in the span-wise direction to obtain $\langle U(y) \rangle$. From this mean velocity profile the friction velocity is calculated,

$$u_\tau = \sqrt{\nu \left(\frac{\partial |\langle U(y) \rangle|_2}{\partial y} \right)_{y=0}} \tag{2.28}$$

   where ν is the kinematic viscosity, and $|\ \ |_2$ represents the $L-2$ norm.

3. The fluctuation field $u'(y,z,t)$ is computed and transformed to wall coordinates using Eq. 2.29,

$$\begin{aligned} u'(y,z,t) &= U(y,z,t) - \langle U(y) \rangle \\ u'^{+}(y,z,t) &= \frac{u'(y,z,t)}{u_\tau} \\ y^+ &= \frac{y u_\tau}{\nu} \end{aligned} \tag{2.29}$$

   where $(\ \ )^+$ represents a quantity expressed in wall units.

4. From Fig. 2.6 we observe that the variance of the Reynolds stress profiles is higher inside the boundary layer as compared to the region outside the boundary layer. At different wall-normal locations inside the boundary layer, the variance differs by a significant amount. Therefore, we seek to learn the PDF of the Reynolds stresses as

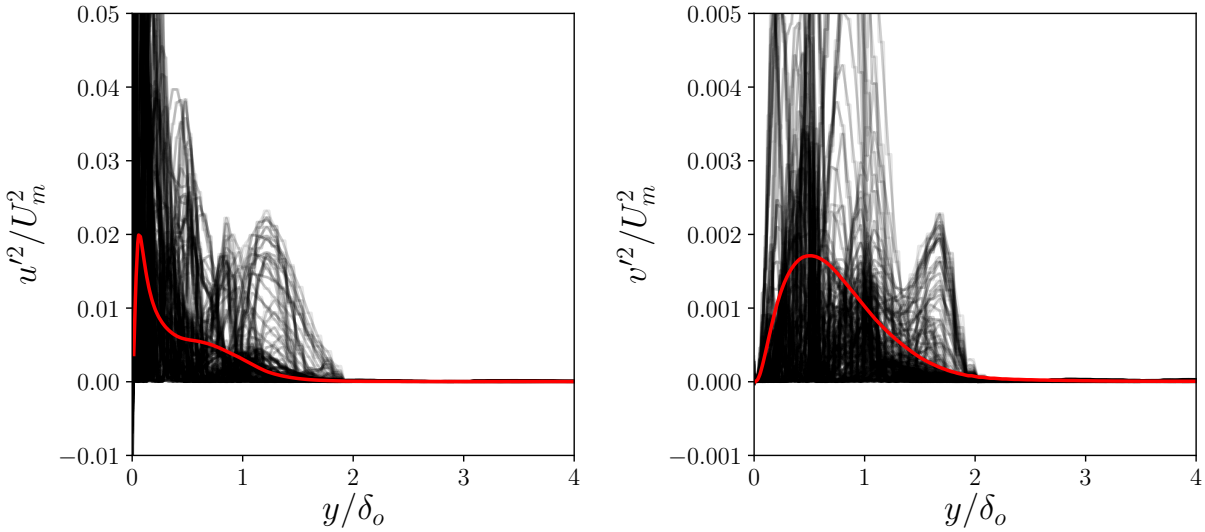

(a) $xx-$component (b) $yy-$component

Figure 2.6: Reynolds stresses at $x/\delta_o = 15$ from the precursor simulation. Red curve is the mean, averaged in time and the spanwise direction. Black lines are the instantaneous profiles.

a function of the wall-normal coordinate. We consider equi-spaced points inside the boundary layer, and learn the PDF of u'^+ for each of those points.

Extensive research on the behavior of Reynolds stresses inside a turbulent boundary [104] reveals that there exists a strong cross-correlation between the x-y components of the fluctuation field, whereas the cross-correlation between the x-z and y-z components is negligible. We capitalize on this fact in the training process: simply put, we learn a joint distribution of the x-y components of the fluctuation field and an independent distribution of the z-component.

The PDFs are learned using the kernel density estimation method [103] implementation in the *scikit-learn* Python machine learning library. The word "learn" refers to determining the shape of the PDF of velocity fluctuation fields at different wall-normal locations. For the learning process, we use a k-folds approach in which we divide the training dataset in k parts. The velocity profiles in each of those folds are chosen at random, but the number of profiles in each fold is the same. $(k-1)$ out of those k folds are used for learning the PDF, and one fold is used for testing the PDF accuracy.

5. After learning the PDFs for different wall-normal locations, we use them to generate the u'^{+} field for the inflow of the main simulation using the *rejection sampling* procedure [105]. These fluctuations are transformed to physical coordinates to obtain the fluctuation field $u'(y, z, t)$. The fluctuation field is then superimposed on the mean turbulent velocity profile at the inlet.

$$\begin{aligned} u'(y, z, t) &= u'^{+}(y, z, t) \times u_\tau \\ U(y, z, t) &= U(y) + u'(y, z, t) \end{aligned} \tag{2.30}$$

2.5.2 Preliminary validation

In order to examine the accuracy of our proposed method, we follow a two-step process: (i) *Learning process.* The process in which we use the procedure outlined in Sec. 2.5.1 to learn the PDFs of the velocity fluctuation fields in the three coordinate directions, and (ii) *Physical validation.* The main step in which we use the PDFs learned from step (i) to generate a time-varying velocity inflow field to simulate a SETBL on a flat plate.

To train the ML models, we perform a precursor simulation of a SETBL at a inlet Reynolds number (Re_δ) of 7000, based on the mean velocity and the inlet boundary layer thickness. The procedure outlined in Sec. 2.4.2 is used to perform the precursor simulation. We discovered that the flow requires a transition length of approximately $12\delta_o$ to develop into a realistic TBL. Therefore, we sample instantaneous velocity field from the precursor simulation at a stream-wise distance of $15\delta_o$. The velocity profiles are sampled over a time period of $700\delta_o/U_m$, starting at $500\delta_o/U_m$ to avoid the influence of the initial transient. Using the procedure described in Sec. 2.5.1, we learn the PDFs of the velocity fluctuations as a function of the wall-normal (y) coordinate. The kernel density estimation (KDE) models are used to generate Reynolds stress profiles presented in Fig. 2.7. We compare the profiles generated by the ML model with the training profile from the precursor simulation and DNS profiles of Wu *et al.* [95]. The different values of n in Fig. 2.7 correspond to profiles obtained

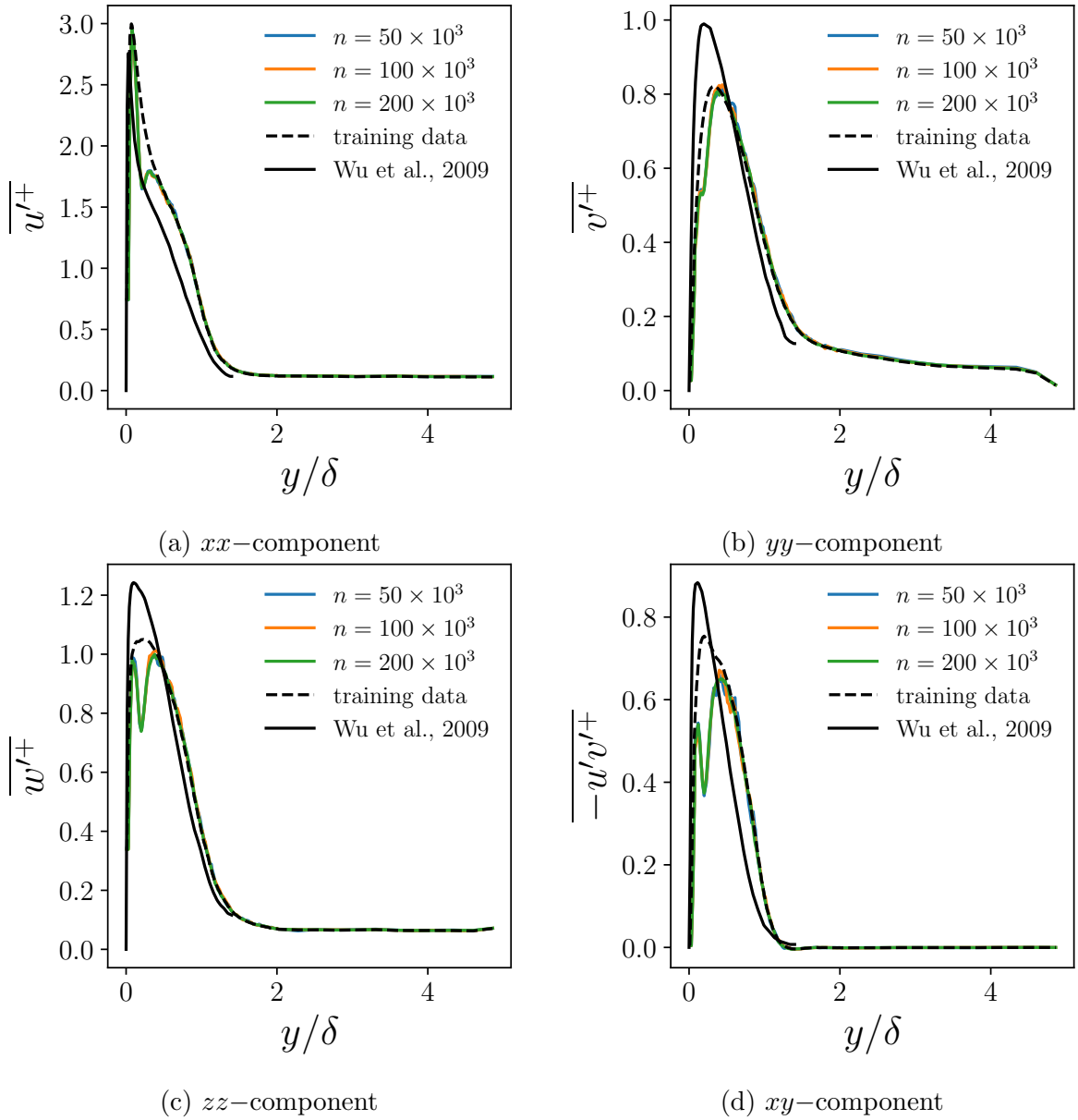

(a) $xx-$component

(b) $yy-$component

(c) $zz-$component

(d) $xy-$component

Figure 2.7: Machine-learned profiles of Reynolds stresses at $x/\delta_o = 15$ from the precursor simulation.

from KDE models trained using different number of samples. We observe that the accuracy of the KDE models is independent of the number of training samples for $n > 50 \times 10^3$. The DNS profiles are presented only as a guide to verify the physical validity of our results. From Fig. 2.7, it evident that the KDE models produce a fluctuation field with a mean profile that exhibits good agreement with the training data. Also it is clear that the number of training samples does not have a major effect on the accuracy of the Reynolds stress profiles. After

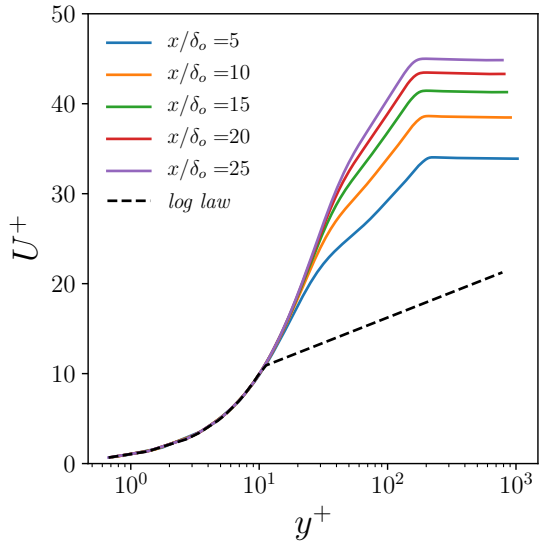

(a) Mean velocity vs. wall-normal coordinate in wall units.

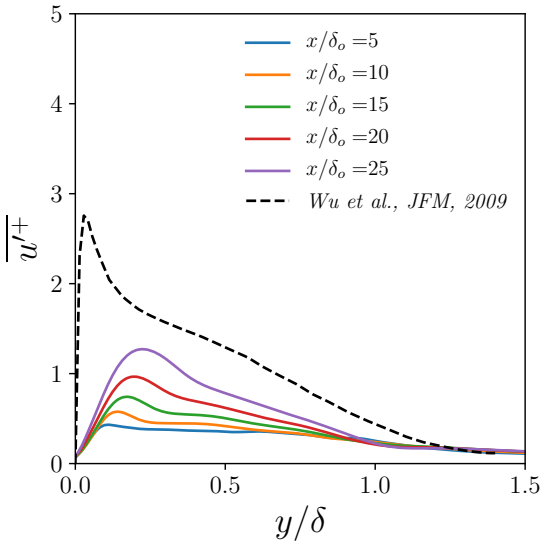

(b) $xx-$component of Reynolds stress vs. normalized wall-normal coordinate.

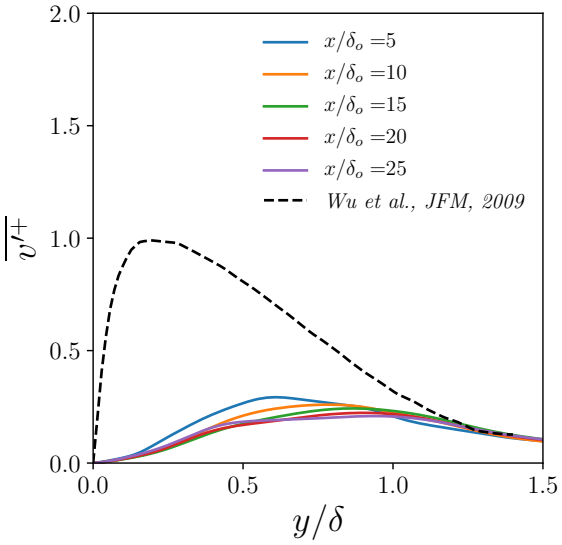

(c) $yy-$component of Reynolds stress vs. normalized wall-normal coordinate.

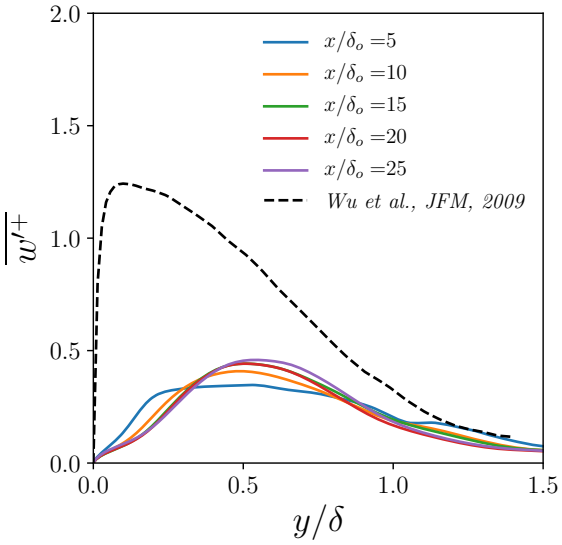

(d) $zz-$component of Reynolds stress vs. normalized wall-normal coordinate.

Figure 2.8: Results from main SETBL simulation on a flat plate using ML inflow approach.

having successfully trained the ML models, we performed the next step, which is physical validation.

To validate the ML approach, we use KDE models to generate a time-varying velocity fluctuation field which was used as a inflow boundary condition for the main simulation. The computational setup of the main simulation is exactly the same as the precursor simulation.

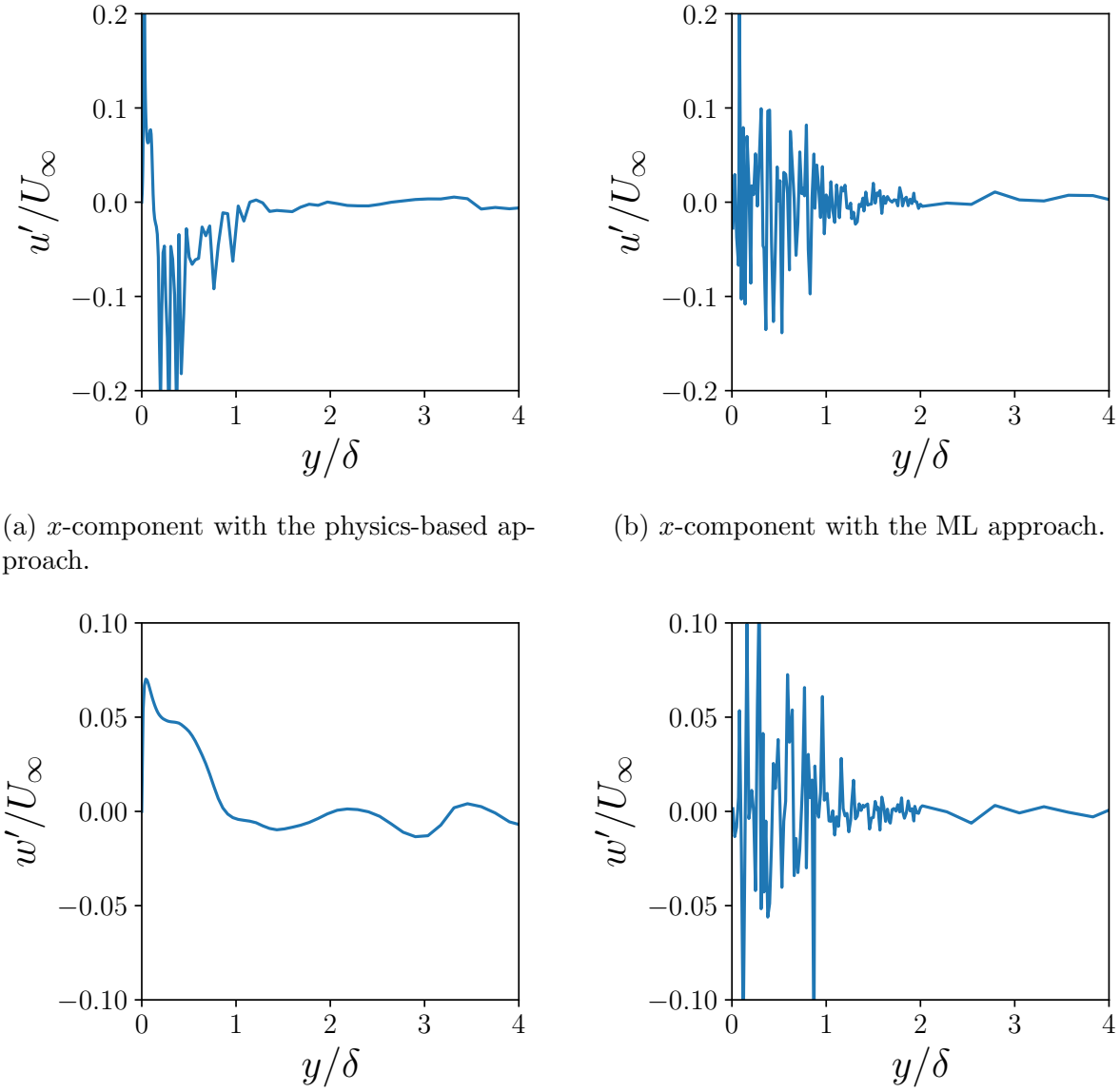

(a) x-component with the physics-based approach.

(b) x-component with the ML approach.

(c) z-component with the physics-based approach.

(d) z-component with the ML approach.

Figure 2.9: Instantaneous velocity fluctuation profiles generated by the physics-based approach and the ML approach.

We present the mean velocity and the Reynolds stresses obtained at different stream-wise locations in Fig. 2.8. All the quantities are averaged in time and the span-wise direction. From the mean velocity profiles we observe that the magnitude of the mean velocity exhibits a reasonable agreement in the inner region ($y^+ < 50$). However, in the logarithmic region the magnitude increases with increasing stream-wise coordinate. The increase is particularly

significant in the initial part of the domain ($x/\delta_o < 15$), and the profiles tend to approach an asymptotic value towards the end of the domain. On the other hand, the Reynolds stress profiles exhibit a magnitude significantly lower than the reference DNS profiles. The magnitude of the Reynolds stress profiles in all three directions increases as we move along the stream-wise coordinate. This observed behavior of the mean velocity and the Reynolds stress profiles can be explained by examining the instantaneous velocity fluctuation profiles generated by the ML approach, as discussed below.

Fig. 2.9 illustrates the instantaneous velocity fluctuation profiles generated by the physics-based approach described in Sec. 2.4.2 and the ML approach described in Sec. 2.5. With the conventional (physics-based) approach, the superposition of Fourier modes is evident from the underlying wave-like pattern observed in Fig. 2.9a and 2.9c. This field is later on modified in the wall-normal direction to account for the anisotropy near the wall in a SETBL. Following this approach results in a distribution of turbulent kinetic energy across the range of wave-numbers resolved by the computational grid. Although, the fluctuation field generated by the physics-based approach does not obey the Navier-Stokes equations at the inlet, there is enough energy in the smaller wave-numbers, which correspond to the large scale structures in the turbulent boundary layer, to set the energy cascade in motion. As the flow transitions to a realistic turbulent boundary layer, energy is redistributed across the spectrum of length scales to achieve equilibrium. In the case of a TBL, equilibrium is referred to as the state in which production of TKE at the large scales in balanced by dissipation of TKE at the smallest scales.

In case of the ML approach, the KDE models are learned as a function of the wall-normal coordinate, but independently of each other. This approach therefore does not account for the spatial and temporal relationship between the fluctuation fields. The instantaneous velocity profiles presented in Fig. 2.9b and 2.9d confirm this point. The fluctuations at adjacent $y-$locations are completely independent of each other with no underlying modal structure. This observation can also be interpreted as generating a fluctuation field, where

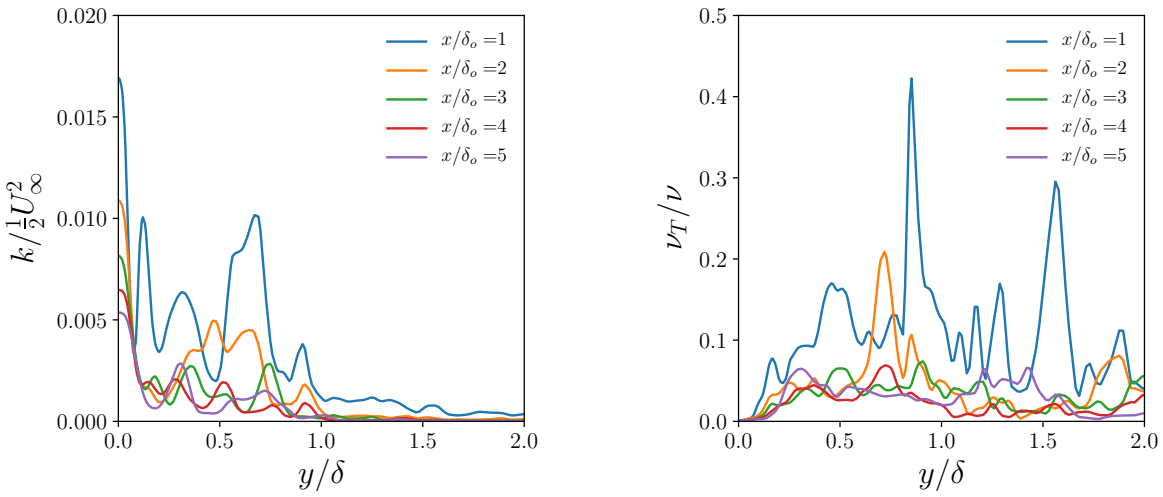

(a) Normalized SGS kinetic energy (k). (b) Normalized turbulent viscosity (ν_T).

Figure 2.10: Span-wise averaged profiles vs. normalized wall-normal coordinate (y) from a SETBL on a flat plate using the ML approach.

all the energy content is present in the high wave-numbers which cannot be resolved on the computational grid. In Fig. 2.10a, we observe a high initial magnitude of SGS kinetic energy, and the magnitude gradually decreases in the stream-wise direction. The increase in k is accompanied by an increased turbulent viscosity (ν_T), which results in an increased contribution to the SGS stress term to the filtered Navier-Stokes equation (Eq. 2.4). The increase is SGS stress is further balanced by a strong favorable pressure gradient (FPG). As a result, the magnitude of the mean velocity in the outer region increases [98] which is clearly visible in Fig. 2.8a. The high frequency nature of the inflow turbulence leads to an absence of grid scale coherent structures in the TBL. Therefore, there is negligible turbulent kinetic energy in the resolved scales which is evident from the Reynolds stress profiles in Fig. 2.8b, 2.8c, and 2.8d. The magnitude of the $xx-$component of the Reynolds stress increases much more rapidly in the stream-wise direction than the other components in Fig. 2.8. The reason for this increase is the contribution of the stream-wise and wall-normal gradients in $x-$component of velocity to the $xx-$component of the Reynolds stress tensor. The ML inflow approach would require a larger computational domain for the TBL to achieve equilibrium, which is impractical for the present simulations.

2.5.3 A modified machine learning approach

To address the drawbacks of the ML inflow method described in Sec. 2.5.1, we propose a modification to the learning process inspired by the lessons learnt while developing time-varying inflow conditions for SETBL over a flat plate. This strategy paves a way forward to improve on the existing method to achieve shorter transition lengths and reduced computational time. The idea presented in this section is a well-informed hypothesis, which begs further investigation.

A TBL is made up of coherent structures which vary in length and time scales. The distribution of turbulent kinetic energy amongst these varying scales must be accounted for in our approach. Considering this distribution in the Fourier domain, we realize that there is a specific superposition of the resolved Fourier modes in space and time which must be respected when prescribing such a boundary condition. With this view in mind, we propose to perform the learning process in the Fourier space as opposed to our prior efforts in the physical space as follows,

1. Sample velocity profiles from the precursor simulation of a SETBL on a flat plate at every time-step taken from a plane normal to the flow direction after the initial transient.

2. Consider a set of these velocity profiles in ascending time order. The set should span a time-interval corresponding to the convection of the largest structures ($l^+ \sim 100$) at the mean boundary layer velocity.

$$\Delta t = \frac{l^+}{U_m} \tag{2.31}$$

   Project the velocity fluctuations in this 3D volume onto Fourier space.

3. Learn the distribution of the Fourier coefficients after projection using a KDE-type algorithm.

4. Use the learned KDE-type models to generate a 3D superposition of Fourier modes.

5. Inverse Fourier transform these modes to obtain a velocity fluctuation field in the physical space to be used as a time-varying inflow boundary condition.

2.6 Summary and conclusions

In this chapter, we listed the governing equations, motivated our turbulence modeling approach, and described the underlying numerical methods. An essential part of our problem is the accurate specification of the boundary conditions. We described the challenges in simulating a SETBL, in particular regarding inflow boundary conditions. We described two such approaches. The first, a physics-based approach, is shown to simulate a SETBL on a flat plate with good accuracy. For the Reynolds number under consideration in the present work this approach requires a transition length of $x \approx 12\delta$ to develop into a realistic TBL. The second, is a novel approach, based on machine-learning (ML) to address some of the drawbacks of the existing methods.

CHAPTER III

Understanding the dependence of near-wake characteristics on the cube height in a turbulent boundary layer

3.1 Introduction

Turbulent flow over a wall-mounted cube is a canonical problem with applications in many engineering fields. A cube placed inside a channel flow with no-slip boundary conditions on the top and bottom-walls replicates flow over printed circuit boards with chips mounted, heat exchangers with cooling fins, turbines with rotor blades, to name a few examples. Understanding the flow physics and the heat transfer mechanisms in such flows has significant implications in the engineering design process. Researchers have resorted to both experimental and numerical methods to investigate different aspects of flow over wall-mounted obstacles.

Experimental studies of a single cube placed inside a fully developed channel flow were performed by Martinuzzi and Tropea [54], Hussein and Martinuzzi [11], Meinders and Hanjalic [106] and Meinders et al. [107]. Time-averaged PIV measurements and laser visualization techniques used in these experiments reveal the existence of flow features like a horse-shoe vortex formed in front of the cube, an arc-shaped vortex formed behind the cube, tornado-shaped vortices formed on the sides, and vortex shedding in the wake of the cube.

We know that the size and intensity of the vortices scales with the incoming boundary layer thickness [108]. For cube heights with $h/\delta > 1.4$, the dynamic behavior of the pressure and velocity fields in bimodal [54]. Hwang *et al.* [109] studied the effect of laminar boundary layers with a low to moderate Reynolds number ($Re < 3500$) on the wake characteristics. They found that the near-wake of the cube is unsteady and turbulent even at low Reynolds number, and the periodicity of the vortical structures depends on the Reynolds number. With advances in computational power, numerical simulations have been performed using Reynolds Averaged Navier-Stokes (RANS) and Large Eddy Simulation (LES) approaches. Steady RANS simulations are [55, 56] are not capable of accurately predicting fully developed turbulent channel flow over a cube because the inherently unsteady nature of vortex shedding cannot be represented with this approach. On the other hand, LES is capable of accurately representing these unsteady flow phenomenon [110]. LES of fully developed turbulent channel flow over a cube was performed by Shah *et al.* [57, 58] and Krajnovic *et al.* [59, 12] at Reynolds number of 40,000 based on the mean velocity and cube height. Back-scatter is observed in the region in front of the cube, therefore Smagorinsky-type LES models do not perform nearly as well as the one-equation LES models and its variants [59]. A survey of LES models [12] in accurately simulating this complex flow problem revealed that the dynamic one-equation model gives good agreement of the mean flow features with experimental data using coarse grids. The dynamic one-equation model was also able to predict the periodicity of the vortical structures to reasonable accuracy. Direct Numerical Simulations (DNS) of flow over a cube in a fully developed channel at $Re = 1870$ [61, 10] illustrates the bi-modal behavior of the wall-normal velocity fluctuation in the region in front of the cube. This behavior is a result of aperiodic ejection of low-momentum fluid away from the wall, and sweep of high-momentum fluid towards the wall. The Reynolds number of the flow in the present work is 19600, and DNS of this complex flow is infeasible to study the dependence on a number of parameters. The choice of this Reynolds number was made so that it is large enough for the results to be Reynolds number independent, but small enough

that we can perform a high-fidelity LES.

A cube placed in a fully developed channel flow is an important canonical problem with applications in a variety of engineering problems however, in numerous situations such as, flow over a car moving on a free-way, flow over objects mounted on the surface of a car or an airplane like vortex generators, flow over a building inside the atmospheric boundary layer, there is no confinement on the top boundary. In such situations flow over a cube placed inside a spatially evolving turbulent boundary layer (SETBL) is a more relevant flow model to study. Sillero *et al.* [63] investigated the differences in the wake structure, velocity components, pressure and velocity fluctuations, between a fully developed channel flow and a turbulent boundary layer (TBL). In case of a TBL the edge of the boundary layer entrains irrotational fluid from the free-stream, and the entrainment reaches equilibrium. The rotational-irrotational intermittency at the edge of the boundary layer is responsible for higher normalized values of velocity and pressure fluctuations in a TBL as compared to a fully developed channel flow. The largest differences lie between a height of $y/\delta \approx 0.3 - 0.8$. We believe these differences will have an effect on the near-wake characteristics of a cube placed inside a TBL. This effect is poorly understood and motivates us to pursue a wall-resolved LES study of a cube placed on a smooth-flat plate in a SETBL. A SETBL is more difficult to replicate as compared to a fully developed channel inflow because of the non-periodic boundary condition in the streamwise direction. Periodic boundary condition resembles an infinite stream-wise domain in which the transition to a fully developed turbulent state is not limited by the stream-wise length of the domain. On the other hand, in a SETBL the flow requires a large stream-wise length due to the slow convergence of larger outer scales [63]. The buffer region ($y^+ < 50$) in a TBL is laden with stream-wise streaks, i.e. narrow stream-wise regions where the stream-wise velocity is larger or smaller than the mean velocity at the same height from the wall. The characteristic span-wise spacing of these streaks inside the buffer region is $\lambda_z^+ \approx 100$ [17, 111]. Coherent structures, however, exist at scales comparable to the boundary layer thickness (δ). These coherent large scale structures populate the outer

region of the TBL, and carry a significant amount of turbulent kinetic energy (TKE) and turbulent Reynolds stresses [112, 113, 114]. Therefore, it is evident that the height of the cube (h) relative to δ will play a crucial role in the extent and the nature of its interaction with a TBL. The TKE distribution in the near-wake of the cube will depend on the h/δ ratio which is investigated in this work.

In the present study we perform wall-resolved LES of flow over a cube placed inside a SETBL. An in-house code is developed to prescribe a time-varying turbulent inlet boundary condition to achieve a SETBL with the desired boundary layer thickness and turbulence statistics at the cube [115]. We investigate the effect of h/δ ratio on the near-wake characteristics. Our hypothesis is that a larger cube enables larger TKE production, and exhibits a more rapid decay of TKE as a function of the stream-wise coordinate. The underlying idea is that the characteristic vortices associated with the cube scale with the height of the cube, and larger vortices signify a greater departure of the TKE distribution from an equilibrium state. We present the dependence of the horse-shoe vortex and turbulent kinetic energy on the h/δ ratio. The results from this study have potential implications in design of passive vortex generators for flow control.

3.2 Computational approach

3.2.1 Geometry and mesh

We consider a SETBL flow over a flat plate of length $18\delta_o$, where δ_o is the boundary layer thickness at the inlet. As seen in Fig. 3.1, a cube of height h is placed in the plane of symmetry of the flat plate with its front face at a stream-wise location of $12\delta_o$ from the inflow boundary. A synthetic inflow method [116] is used to prescribe a time-varying inflow velocity field to simulate the SETBL with a free-stream turbulence of 1%. The synthetic inflow velocity field does not obey the Navier-Stokes equations and requires a transition length of $12\delta_o$ to develop into a realistic TBL. Hence the cube is placed at $12\delta_o$ from the

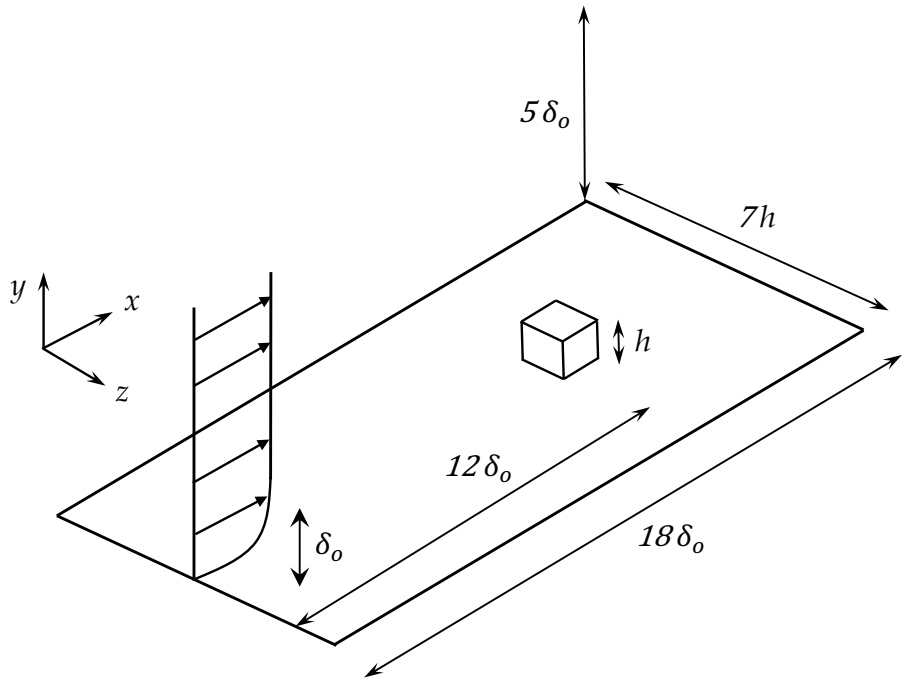

Figure 3.1: Problem setup

inlet plane. In the absence of the cube, the boundary layer thickness at $x = 12\delta_o$ is also δ_o. We investigate the effect of h/δ_o ratio on the near-wake characteristics by keeping the incoming boundary layer thickness constant and considering three different cube heights, so that h/δ_o is 0.2, 0.6 and 1.0. The width of the domain is $7h$, because we know this width is sufficiently large to avoid any effect of the side-walls on the turbulent wake [12, 61]. The height of the domain is $5\delta_o$ so that we can capture all the effects of the turbulent shear layer formed on top of the cube and avoid any interaction with the top-wall. The Reynolds number (Re_h) based on the mean velocity (U_m) and boundary layer thickness (δ_o) at the inlet is 19,600. The Reynolds number (Re_τ) based on the friction velocity (u_τ) and the boundary layer thickness (δ_o) at the inlet is 800. The choice of the Reynolds number is influenced by two factors: (i) it should be small enough so that it is feasible to perform wall-resolved LES, and (ii) it should be large enough for our results to be Reynolds number independent. Castro *et al.* [108] observed that there are no discernible Reynolds number

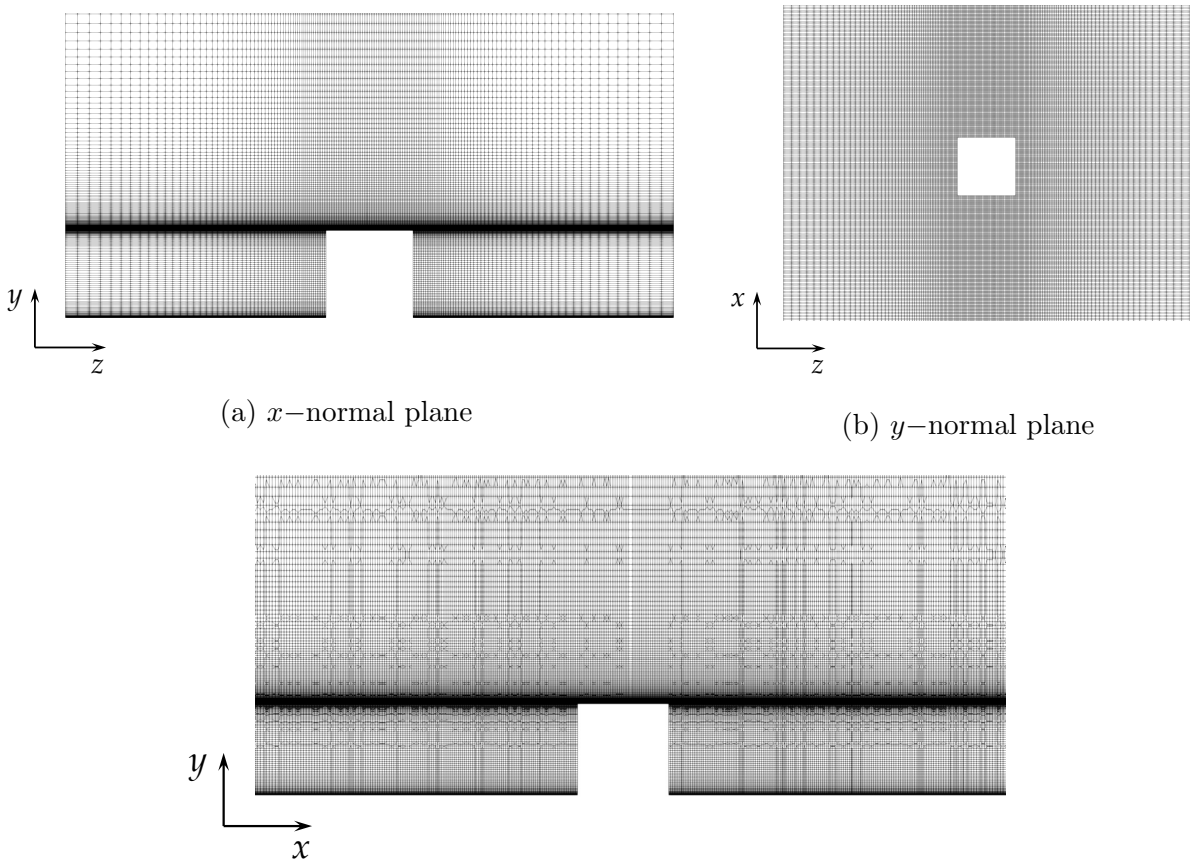

(a) $x-$normal plane

(b) $y-$normal plane

(c) $z-$normal plane

Figure 3.2: Computational grid for $h/\delta_o = 1.0$.

effects of incoming turbulent conditions if $Re_h > 4000$, and the Re_h in this study varies from 3,920 to 19,600. The boundary conditions used in the simulation are no-slip on the bottom-wall and the surface of the cube. Slip-wall boundary conditions are used on the side walls and the top-wall. A zero-gradient boundary condition is used on the outlet. A time-varying turbulent inflow boundary condition is used at the inlet. An in-house code is used to provide a time-varying turbulent inflow field, which implements the procedure described by Le [1]. The inflow generation procedure has been validated for the present flow configuration (Appendix A).

The mesh is non-uniform with smaller cells in the vicinity of the cube and larger cells towards the periphery of the domain, as demonstrated in Fig. 3.2. Fig. 3.2 illustrates the

computational grid for $h/\delta_o = 1.0$ by taking slices normal to the three directions. Similar mesh is used for $h/\delta_o = 0.6$ and 0.2. Three different mesh resolutions are used to achieve grid convergence. The details of the three grids are presented in Table 3.1. Grid convergence is achieved on the fine mesh, and results can be found in Appendix C.

3.2.2 Numerical Method

The incompressible filtered Navier-Stokes equations are solved with a finite volume approach using OpenFOAM [77]. The effect of the sub-grid scales is accounted for with the dynamic $k-$equation eddy-viscosity LES model [81]. The reason to use this model is its ability to capture back-scatter. Back-scatter of turbulent kinetic energy is observed in the region in front of the cube [12]. This model can also accurately simulate the periodicity of the vortices formed around the cube. A second-order central scheme is used for the viscous and pressure terms, whereas as the LUST (Linear Upwind Stabilized Transport) [84] scheme is used to discretize the convection term. LUST scheme a linear combination of the central and linear upwind schemes with weights 0.75 and 0.25 respectively. Mittal *et al.* [87] reported that for LES of turbulent flows, the computational grids and boundary conditions should be designed with extreme care when using a central scheme for the convective term. To overcome this problem, a more robust LUST scheme is used in the present work. The solution is advanced in time using a second-order implicit backward time-marching scheme. The validation results were presented in Appendix B [116]. The simulations are carried out for a total time period of $1100\delta_o/U_m$ with variable time-step and a maximum Courant num-

Mesh	Δx^+_{min}	Δx^+_{max}	Δy^+_{min}	Δy^+_{max}	Δz^+_{min}	Δz^+_{max}
Coarse	21	104	2.5	200	21	146
Medium	18	80	0.5	200	18	125
Fine	16	74	0.5	200	16	110

* Δ^+ represents grid spacing in wall units. $\Delta^+ = \Delta u_\tau/\nu$

Table 3.1: Non-dimensional grid spacing details.

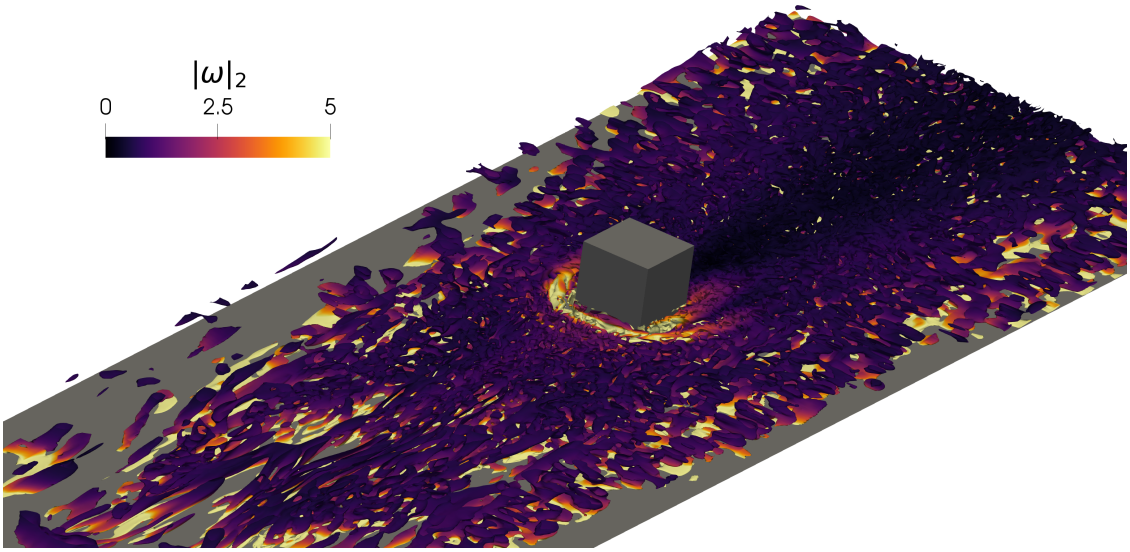

Figure 3.3: Iso-surfaces of $Q-$criterion colored with vorticity in the near wall region for a cube with $h/\delta_o = 1.0$ in a SETBL.

ber of 1.0. The turbulent statistics are averaged starting from $100\delta_o/U_m$ over a time period of $1000\delta_o/U_m$ to avoid contamination of the results by the initial transient.

3.3 Results

3.3.1 Flow description

We present the iso-surfaces of the $Q-$criterion colored with vorticity magnitude for $h/\delta_o = 1.0$ in Fig. 3.3 and 1.14 to illustrate the basic features of flow over a cube in a TBL. The $Q-$criterion is the second invariant of the velocity gradient tensor (∇u) and defines a vortex as a "connected fluid region with a positive second invariant of ∇u" i.e. $Q > 0$. It represents vortices as regions where the vorticity magnitude is greater than the magnitude of the rate-of-strain [62]. In Fig. 3.3, we depict the inner region of the TBL which contains small-scale coherent structures. We observe that the density of small-scale structures increases in the near-wake due to the break-down of vortices produced by the cube. In Fig. 3.3 and 1.14, we notice a region of high vorticity in the shape of a horse-shoe around the front-face of the cube. This region is known as the horse-shoe vortex. We examine the dependence of the

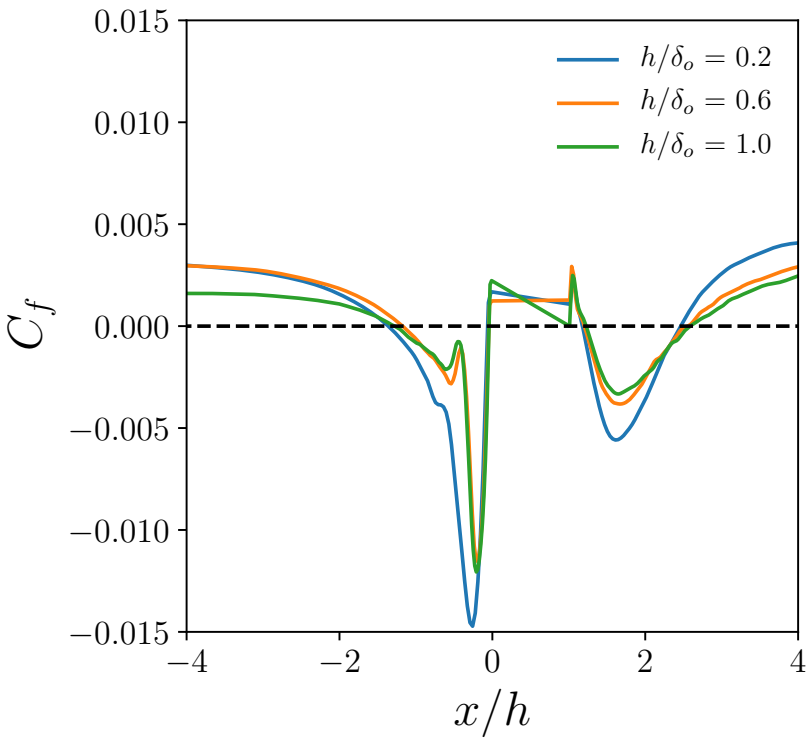

Figure 3.4: Skin friction coefficient (C_f) for different h/δ_o ratios.

horse-shoe vortex on the h/δ_o ratio in Sec. 3.3.3. The lateral vortices formed on the sides of the cube, and the vortex shedding from the top surface are visible in Fig. 1.14. The vorticity magnitude decreases in the wake of the cube as we move along the stream-wise direction.

3.3.2 Drag coefficient, separation and reattachment lengths

Previous experimental and numerical studies [54, 59, 12] performed on flow over a cube placed inside a channel flow have reported the existence of a horse-shoe vortex around the cube. The presence of the horse-shoe vortex leads to the separation of the boundary layer from the bottom-wall in front of the cube and reattachment of the boundary layer behind the cube. The separation length (X_s) is the length in front of the cube where the boundary layer separates from the bottom-wall; the reattachment length (X_r) is the length behind the cube where the boundary layer reattaches to the bottom-wall. The skin-friction coefficient (C_f)

is plotted against the stream-wise coordinate in Fig. 3.4 to quantify X_s and X_r. The exact values of X_s and X_r are shown in Table 3.2. Our results for X_s and X_r are similar to those obtained from DNS of a wall-mounted cube in a fully developed channel flow [61, 11]. From Fig. 3.4 and Table 3.2 we observe that X_s and X_r are independent of the cube height to boundary layer thickness ratio. This observation indicates that the stream-wise position of the horse-shoe vortex formed around the cube scales with the size of the cube itself. On the other hand, from Table 3.2 we notice that the drag coefficient (C_d) increases with increasing h/δ_o. This increase is justified by the fact that a larger cube provides a greater resistance to the boundary layer flow.

3.3.3 Horse-shoe vortex

We analyze the strength and the size of the horse-shoe vortex in Fig. 3.5. The x-component of the time-averaged vorticity is plotted in the $y-z$ plane for the three h/δ_o ratios. In Fig. 3.5a - 3.5i, we observe two bright spots on either sides of the cube along the wall which correspond to the horse-shoe vortex. In the region close to the wall, between the horse-shoe vortex and the bottom-wall we observe a secondary vortex sheet, which extends to a more wider span-wise distance. As we go downstream, we observe the diverging nature of the horse-shoe vortex, whose strength decreases with increasing x/h. For a given x/h location, the smaller cube has a weaker horse-shoe vortex. Interestingly, we notice that for $h/\delta_o = 0.6$ and 1.0, the horse-shoe is confined to a wall-normal distance of $0.2y/h$ and span-wise distance of $1.2z/h$, whereas for $h/\delta_o = 0.2$ it extends to $0.3y/h$ and $1.3z/h$ in the wall-

Cube height (h/δ_o)	C_d	Separation length (X_s/h)	Reattachment length (X_r/h)
0.2	0.6	1.3	1.5
0.6	0.9	1.2	1.6
1.0	1.0	1.3	1.6

Table 3.2: Drag coefficient (C_d), and separation and reattachment length normalized by cube height for a spatially evolving turbulent boundary layer flow over a wall-mounted cube.

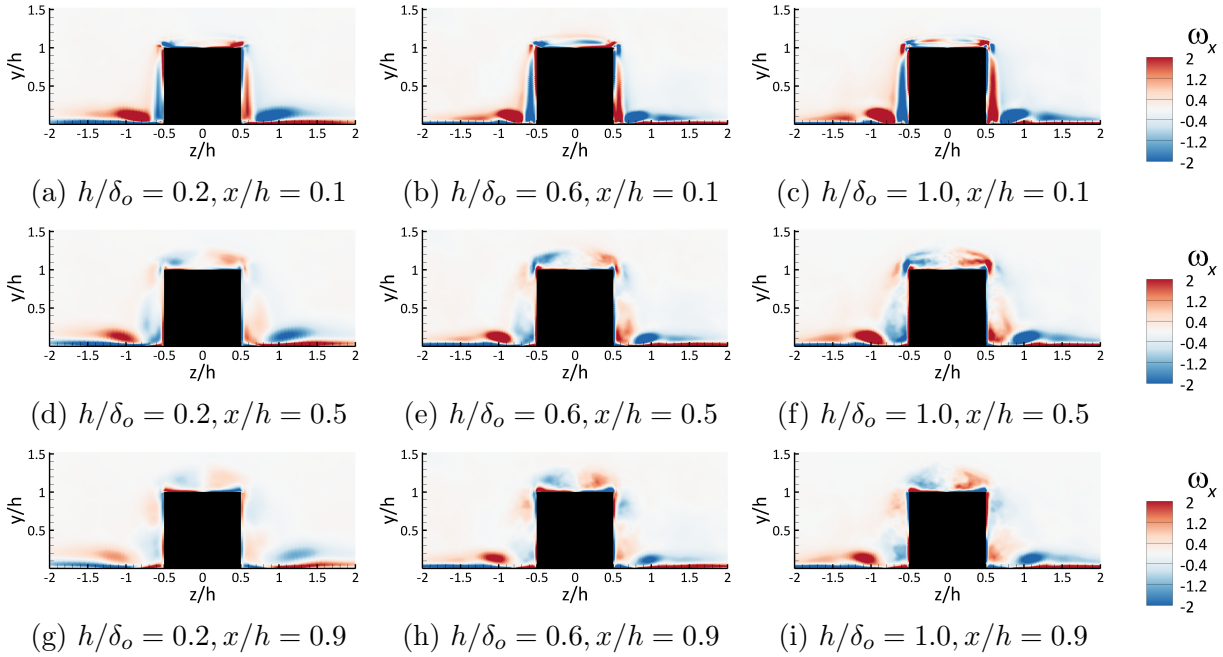

(a) $h/\delta_o = 0.2, x/h = 0.1$ (b) $h/\delta_o = 0.6, x/h = 0.1$ (c) $h/\delta_o = 1.0, x/h = 0.1$

(d) $h/\delta_o = 0.2, x/h = 0.5$ (e) $h/\delta_o = 0.6, x/h = 0.5$ (f) $h/\delta_o = 1.0, x/h = 0.5$

(g) $h/\delta_o = 0.2, x/h = 0.9$ (h) $h/\delta_o = 0.6, x/h = 0.9$ (i) $h/\delta_o = 1.0, x/h = 0.9$

Figure 3.5: Span-wise contours of streamwise component of the mean vorticity at $x/h = 0.1, 0.5$ and 0.9 along the cube, with the cube outlined in black

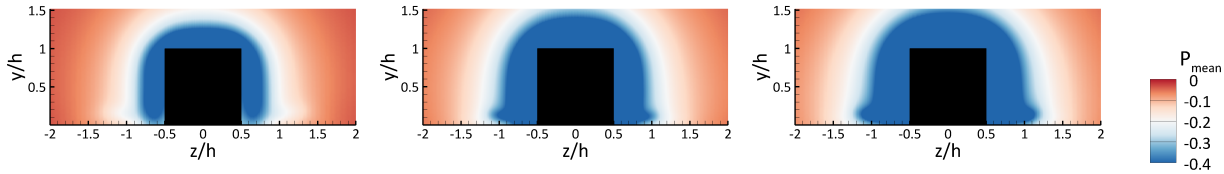

(a) $h/\delta_o = 0.2, x/h = 0.5$ (b) $h/\delta_o = 0.6, x/h = 0.5$ (c) $h/\delta_o = 1.0, x/h = 0.5$

Figure 3.6: Mean pressure contours in the $y - z$ plane at $x/h = 0.5$, with the cube outlined in black.

normal and span-wise directions respectively. Yakhot *et al.* [61] performed a direct numerical simulation (DNS) of flow over a cube placed inside a channel at a far lower $Re = 1870$ and $h/\delta_o = 1.0$, and reported a horse-shoe vortex extending from $0.35y/h$ to $1.4z/h$ towards the rear face of the cube, which is close to our results for the $h/\delta_o = 0.2$. We believe this agreement is because the $h/\delta_o = 0.2$ cube is located deeper inside the boundary layer, and therefore surrounded by lower velocity fluid. In our simulations the Reynolds number based on cube height in this region is 3920, which is much closer to the Reynolds number from Yakhot *et al.* than our free-stream Reynolds number of 19,600. The slower rate of spreading of the horse-shoe vortex for larger cube heights can be explained from the mean pressure

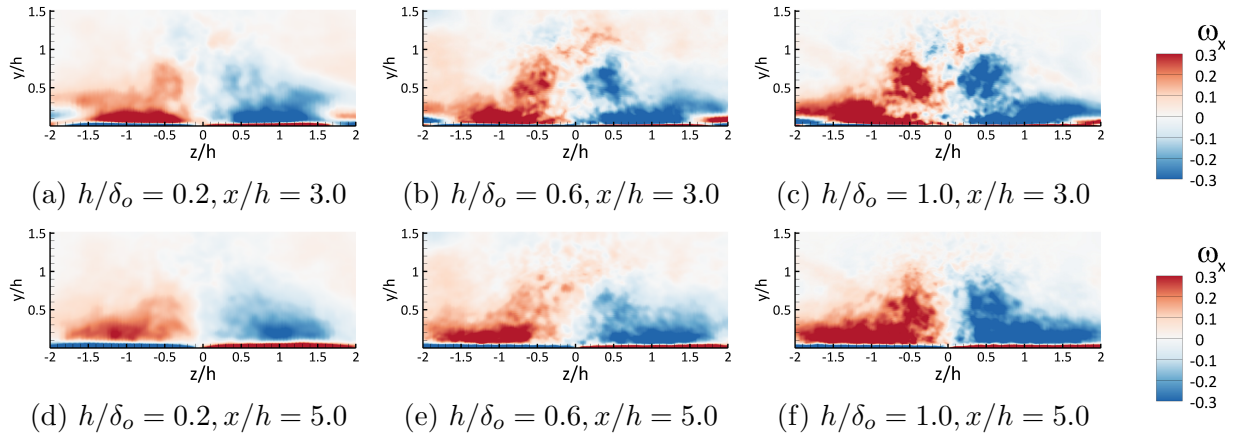

(a) $h/\delta_o = 0.2, x/h = 3.0$ (b) $h/\delta_o = 0.6, x/h = 3.0$ (c) $h/\delta_o = 1.0, x/h = 3.0$

(d) $h/\delta_o = 0.2, x/h = 5.0$ (e) $h/\delta_o = 0.6, x/h = 5.0$ (f) $h/\delta_o = 1.0, x/h = 5.0$

Figure 3.7: Span-wise contours of stream-wise mean vorticity at $x = 3h$ and $5h$ downstream of the cube.

contours represented in Fig. 3.6. For greater cube heights, there exists a stronger pressure gradient between the side-walls of the cube and the free-stream flow. This increased pressure gradient forces the horse-shoe to remain closer to the side-walls, thereby decreasing the rate of spreading. In summary, the strength of the horse-shoe vortex decreases with decrease in cube height, but the rate of spreading increases with decrease in cube height. The reason for this behavior is the lower, mean pressure gradient in case of smaller cube heights.

In Fig. 3.7 we consider the evolution of the horse-shoe vortex in the wake of the cube. Expectedly, the strength of the horse-shoe vortex continues to decrease with stream-wise distance and cube height. At $x = 3h$, the plane lies just behind the arc-type vortex behind the cube which can be observed in the center. At this location the horse-shoe vortex has spread over a larger wall-normal and span-wise distance of $y \approx 0.4h$ and $z \approx 1.8h$ respectively. As we move further downstream ($x = 5h$), the horse-shoe vortex continues to spread in the $y-z$ plane to $y \approx h$.

3.3.4 Mean velocity and Reynolds stress

The span-wise variation of the mean velocity and Reynolds stresses for $h/\delta_o = 1.0$ are plotted in Fig. 3.8. We consider the results from the simulation for largest cube height to analyze the important flow characteristics because the effects are most pronounced, and

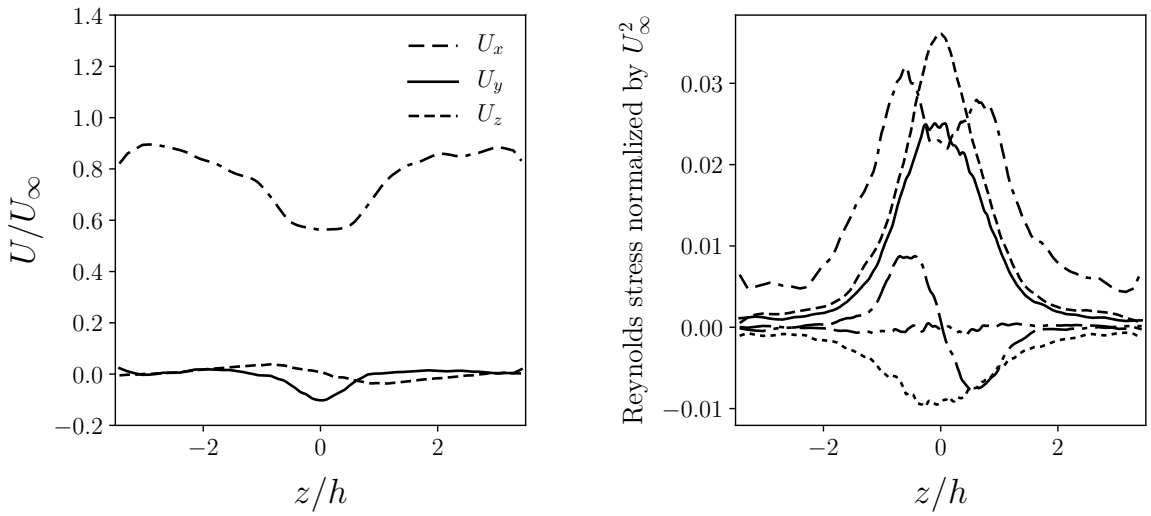

(a) Normalized mean velocity vs. normalized span-wise coordinate.

(b) Normalized Reynolds stress vs. normalized span-wise coordinate.

Figure 3.8: Mean velocity and Reynolds stress profiles at $y = 0.5h$, $x = 4h$ for $h/\delta_o = 1.0$: – – · –, $\overline{u'^2}$; ———, $\overline{v'^2}$; – – – –, $\overline{w'^2}$; ·····, $\overline{u'v'}$; — · —, $\overline{u'w'}$; — · · —, $\overline{v'w'}$.

similar trends are observed for the smaller cube heights. The figures correspond to the stream-wise location of $x = 4h$ and a height of $y = 0.5h$. In Fig. 3.8a we observe that the stream-wise component of velocity is an order of magnitude larger than the other two components and exhibits two peaks at the centers of the two counter-rotating vortices. The stream-wise velocity is lower at the center of the domain, which corresponds to the region in between the counter-rotating vortex pair. The counter-rotating nature of the vortex pair results in a net sweep of high-momentum fluid from the outer region to the near-wall region. This is evident from the negative value of the wall-normal component of velocity in the center of domain. The $z-$component of velocity exhibits a wave-like pattern with a small magnitude and a period of approximately h which is consequence of the vortex-pair. It signifies a net transport of momentum by the $z-$component of velocity towards to the center of the domain.

The components of the Reynolds stress at $x = 4h$, $y = 0.5h$ are plotted for $h/\delta_o = 1.0$ as a function of the span-wise coordinate in Fig. 3.8b. The $\overline{u'^2}$ and $\overline{u'w'}$ components have peaks at the center of the horse-shoe vortex, whereas the $\overline{v'^2}$, $\overline{w'^2}$ and $\overline{u'v'}$ components have

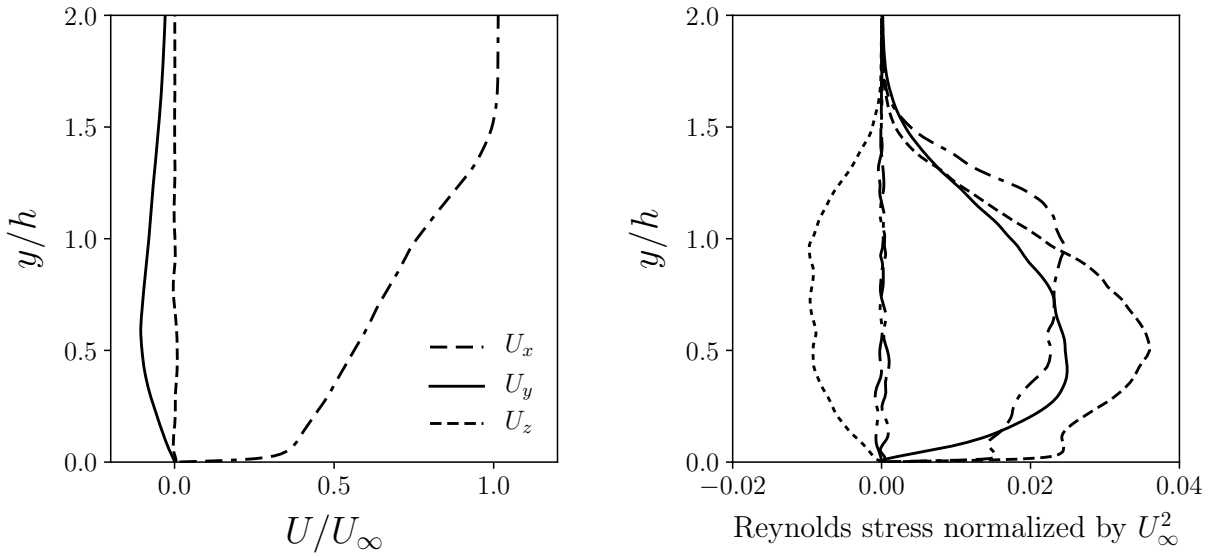

(a) $z = 0$, centerplane.

(b) $z = 0$, centerplane.

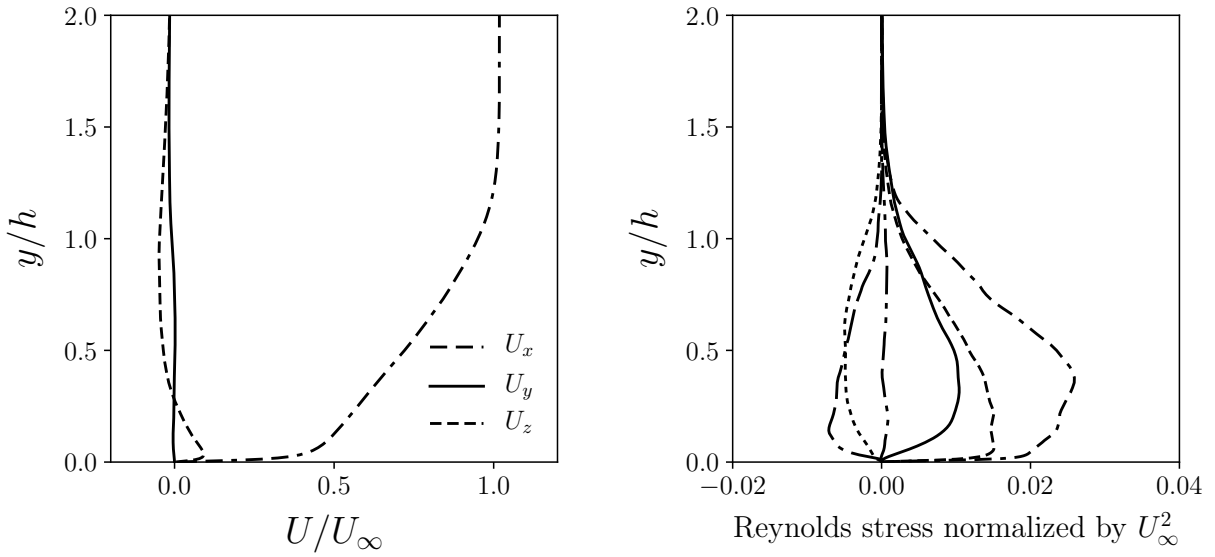

(c) $z = h$.

(d) $z = h$.

Figure 3.9: Mean velocity and Reynolds stress profiles in the centerplane and at $z = h$ for $h/\delta_o = 1.0$ at $x = 4h$: – – · – –, $\overline{u'^2}$; ———, $\overline{v'^2}$; – – – – –, $\overline{w'^2}$; ·····, $\overline{u'v'}$; — · —, $\overline{u'w'}$; — · · —, $\overline{v'w'}$.

peaks at the center of the domain. A increase in $\overline{u'^2}$ at the center of the vortices is a result of turbulent transfer of momentum in the stream-wise direction, and has been observed before for a counter-rotating vortex pair [117]. The peak in $\overline{v'^2}$ and $\overline{w'^2}$ at the center of the domain is because of the wall-normal and span-wise turbulent transport of momentum to the near-wall region and center-plane respectively. The negative peak of $\overline{u'v'}$ is a consequence of the

turbulent transport of momentum ($u' \geqslant 0$) to the negative wall-normal direction ($v' \leqslant 0$). The $\overline{u'w'}$ component has a magnitude comparable to the $\overline{u'v'}$ component which indicates its significance. On the left side of the center-plane high momentum fluid ($u' \geqslant 0$) is carried towards to positive span-wise direction ($w' \geqslant 0$), giving rise to a positive peak in $\overline{u'w'}$. The opposite arguments apply for the negative peak on the right side of the center-plane.

The variation of the mean velocity profile and Reynolds stress in the wall-normal direction in the center-plane and $z = h$, at a stream-wise location of $x = 4h$ for $h/\delta_o = 1.0$ in presented Fig. 3.9. From the $x-$component of mean velocity in Fig. 3.9a and Fig. 3.9c we observe that the boundary layer thickness is greater in the center-plane because boundary layer has not completely recovered, and process of momentum transfer to the center-plane is still underway. In the center-plane the $y-$component of velocity is negative as the high momentum fluid is carried by the counter-rotating vortex pair to the near-wall region. The $z-$component of mean velocity is zero in the center-plane. At $z = h$, the $y-$component of mean velocity of zero however, the $z-$component is positive near the wall and becomes negative away from the wall, this behavior is because of the direction of rotation of the vortex on the right hand side of the center-plane (Fig. 3.7f). The point at which U_z becomes zero ($y = 0.25h$), corresponds to the center of the vortex. The $\overline{u'w'}$ component of the time-averaged Reynolds stress in the center-plane is negligible whereas its magnitude is comparable to the $\overline{u'v'}$ component at $z = h$. This increase in magnitude is because of the span-wise turbulent transport of momentum by the horse-shoe vortex on the right hand side of the center-plane. The $\overline{u'v'}$ and the $\overline{u'w'}$ components are responsible for major production of turbulent kinetic energy at the center of the two vortices, as explained later.

3.3.5 Turbulent kinetic energy

To understand the energy transfer and dissipation in the wake of the cube we show the turbulent kinetic energy (TKE) per unit area for different cube heights as a function of the stream-wise coordinate in Fig. 3.10a. For the three h/δ_o ratios, average the TKE over an

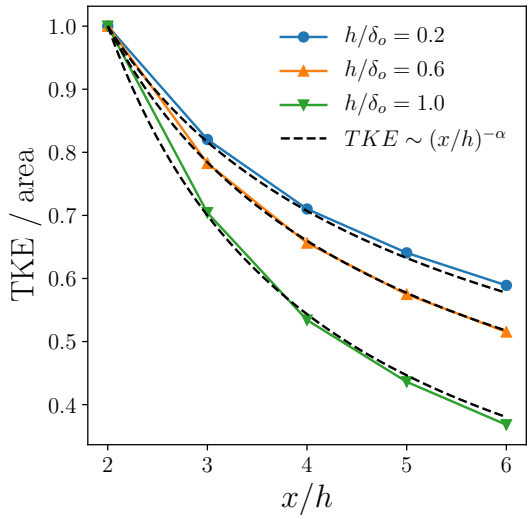

(a) Normalized TKE per unit area vs. normalized stream-wise distance. The dotted line corresponds to the power law behavior with a different value of α for each cube height.

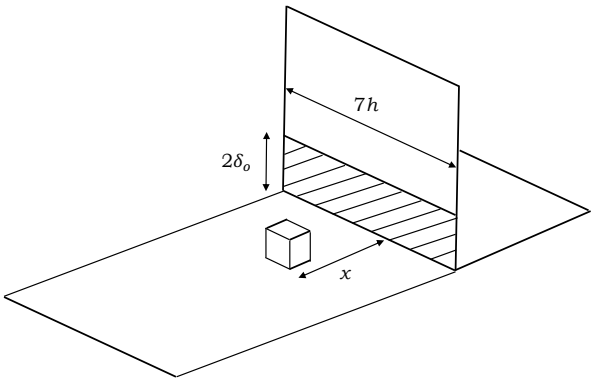

(b) Schematic showing area over which TKE is averaged

Figure 3.10: TKE area density as a function of stream-wise location for different h/δ_o ratios.

area of height $2\delta_o$ and width $7h$ is considered, as illustrated in Fig. 3.10b. This particular height is chosen to ensure that the kinetic energy produced by the shear-layer at the edge of the cube's top surface is accounted for. It height of the shaded area scales with the boundary layer thickness (δ_o) as opposed to the cube height (h) because we intend to capture the effect of interaction between the vortices produced by the cube with the vortices inside the TBL. The vortices produced by the cube scale with h, and the large scale coherent structures inside the TBL scale with δ_o. The interaction between vortices with these two length scales will have an effect on the TKE distribution around the cube, and even for the smallest cube height ($h/\delta_o = 0.2$) will affect the outer region of the TBL. An area with height $2\delta_o$ allows us to capture the effect of this interaction on the TKE distribution inside the TBL. From Fig. 3.10a two important observations stand out: (i) the TKE area density decays in increasing stream-wise distance in a power law manner, and (ii) the rate of decay depends on h/δ_o. The TKE area density decay is summarized by Eq. 3.1.

$$\frac{TKE^*}{area} = \left(\frac{x}{h}\right)^{-\alpha} \tag{3.1}$$

where the " * " denotes that the TKE per unit area is normalized by its value at $x = 2h$, x is the stream-wise coordinate, h is the cube height and, α is the power law exponent. We observe that the TKE area density decay scales with h in the near-wake of the cube. Since we consider the average TKE over the entire span of the domain, the only terms from the TKE budget that should contribute to its decay are the production (P_k) and the dissipation (ϵ_k) of TKE. Hussein *et al.* [11] experimentally showed that P_k and ϵ_k individually decay in a power law manner in the center-plane in near-wake of the cube. In their work, the cube was placed in fully developed channel flow, with h equal half channel height, and the Reynolds number was 80,000 (based on channel height and mean velocity). They reported a decay rate which lies between α =-2 and -2.3 in the center-plane for both, P_k and ϵ_k. However, in our case we observe that $\alpha < 1$, and the reason for this lower values of α is that the decay of P_k and ϵ_k in the center-plane is more rapid as compared to that over the entire shaded area. The greater decay rate in the center-plane is a consequence of larger gradients in velocity and velocity fluctuations in the center-plane. The lower decay rate observed in our work represents an average effect that spans the entire width of the domain. A value of $\alpha < 1$ also implies that the integration of Eq. 3.1 with x/h ranging from 0 to ∞ would diverge, further confirming the at fact that the observed power law decay is a near-wake phenomenon. Physically, as the TBL recovers the TKE area density should remain constant with x/h in the far-wake, and that behavior is not captured by the power law decay.

In Fig. 3.11a we illustrate non-linear increase in the power law exponent with increasing h/δ_o. A 2^{nd} order polynomial can be fit through the three data points using a least squares method leading to Eq. 3.2.

$$\frac{\alpha}{\alpha_o} = 0.6 - 0.2\left(\frac{h}{\delta_o}\right) + 0.6\left(\frac{h}{\delta_o}\right)^2 \tag{3.2}$$

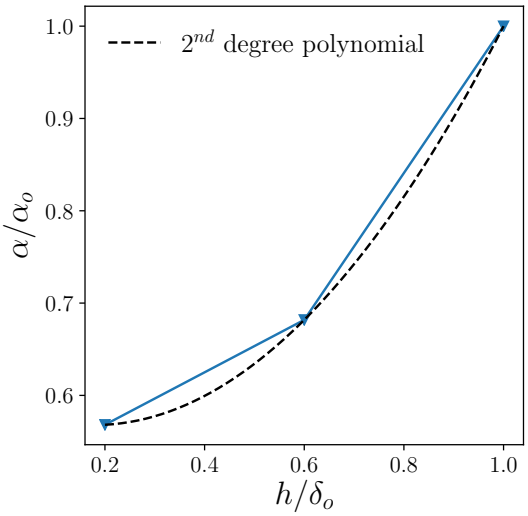

(a) Normalized power law exponent (α/α_o) vs. cube height to boundary layer thickness ratio (h/δ_o), where α_o is the power law exponent corresponding to $h/\delta_o = 1.0$.

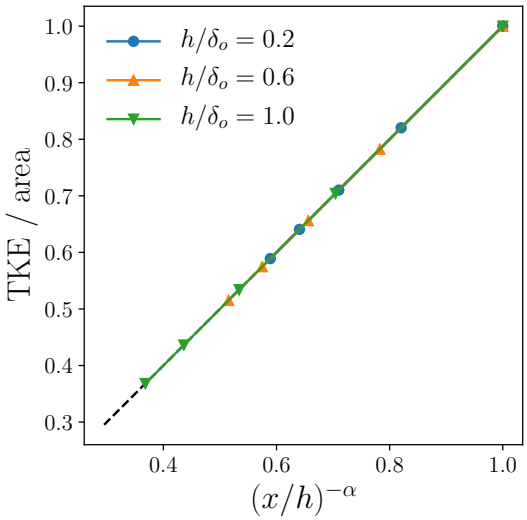

(b) Normalized TKE per unit area vs. cube height to boundary layer thickness ratio (h/δ_o) to the power of $-\alpha$.

Figure 3.11: TKE area density dependence on the normalized stream-wise coordinate.

where $\alpha_o = 0.9$ is the power law exponent corresponding to $h/\delta_o = 1.0$. It is important to note that the fit is non-linear, but does not obey an exponential or a power law expression. The rate of decay increases with increasing h/δ_o which leads us to propose the following hypothesis: (i) P_k and ϵ_k, individually scale with h, and (ii) P_k and ϵ_k decay in a power law manner with x/h. The first hypothesis is confirmed by examining the P_k contribution to the TKE budget of the three h/δ_o ratios. The second hypothesis holds true in the center-plane for the flow over a cube in a turbulent channel [11], and needs to be confirmed for the present flow configuration. A larger cube produces greater TKE because of the greater gradients in velocity present in the outer region, which also represents a greater departure of the flow from the state of equilibrium. A higher decay rate facilitates a faster return to equilibrium state. We believe the rate of decay of TKE in the near-wake is a function of the measure of departure of the flow from equilibrium. A turbulent flow is said to be in equilibrium when the production (P_k) of TKE is balanced by its dissipation (ϵ_k). In Fig. 3.11b, we present the collapsed TKE area density curves for the three cases when the values are scaled with

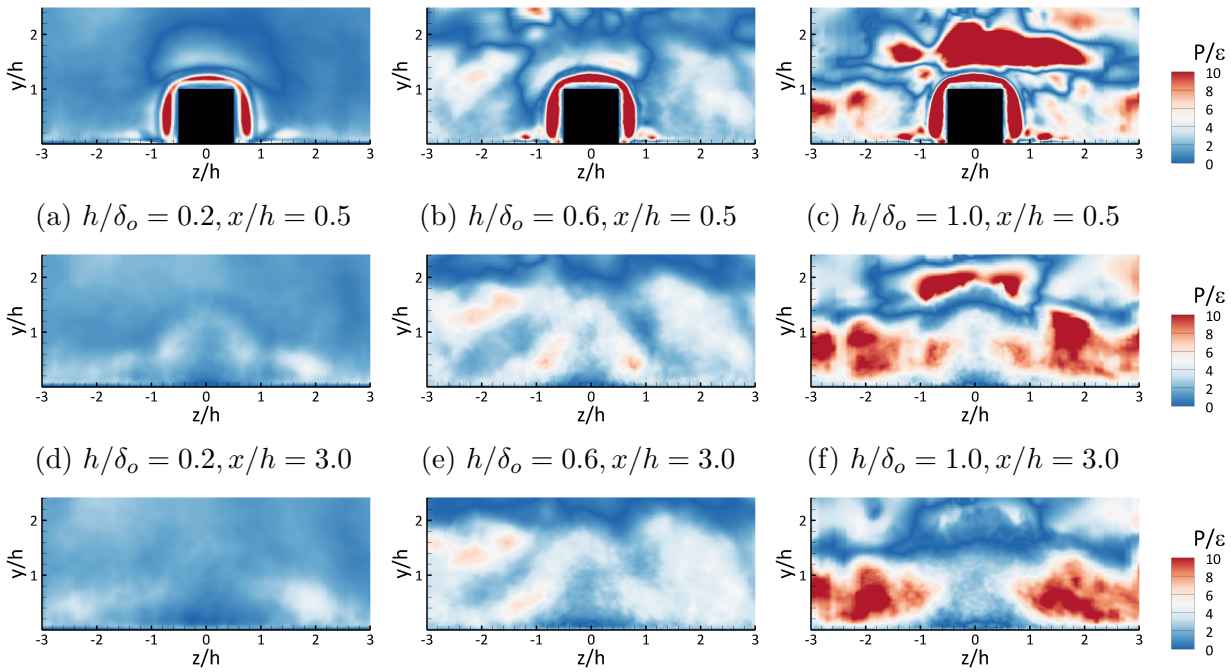

(a) $h/\delta_o = 0.2, x/h = 0.5$ (b) $h/\delta_o = 0.6, x/h = 0.5$ (c) $h/\delta_o = 1.0, x/h = 0.5$

(d) $h/\delta_o = 0.2, x/h = 3.0$ (e) $h/\delta_o = 0.6, x/h = 3.0$ (f) $h/\delta_o = 1.0, x/h = 3.0$

(g) $h/\delta_o = 0.2, x/h = 6.0$ (h) $h/\delta_o = 0.6, x/h = 6.0$ (i) $h/\delta_o = 1.0, x/h = 6.0$

Figure 3.12: TKE production to dissipation ratio contours in the $y-z$ plane at $x/h = 0.5, 2$ and 5.

the power law decay of the stream-wise distance behind the cube.

To better understand the energy transfer, we consider the turbulent kinetic energy budget given by,

$$\begin{aligned}\frac{\partial(\frac{1}{2}q^2)}{\partial t} = &\underbrace{-\frac{1}{2}U_k\overline{(u_l'u_l')}_{,k}}_{C_k}\underbrace{-\overline{(u_l'u_k')}U_{l,k}}_{P_k}\underbrace{-\frac{1}{2}\overline{(u_l'u_l'u_k')}_{,k}}_{T_k}\\ &\underbrace{+\frac{1}{2}\left(\frac{1}{Re}+\nu_\tau\right)\overline{(u_l'u_l')}_{,kk}}_{D_k}\underbrace{-\left(\frac{1}{Re}+\nu_\tau\right)\overline{u_{l,k}'u_{l,k}'}}_{\epsilon_k}\underbrace{-\overline{u_l'p_{,l}'}}_{\Pi_k},\end{aligned} \tag{3.3}$$

where

$$\frac{1}{2}q^2 = \frac{1}{2}(\overline{u'^2}+\overline{v'^2}+\overline{w'^2}) \tag{3.4}$$

$\frac{1}{2}q^2$ is the turbulent kinetic energy, $Re = \frac{U_m\delta}{\nu}$ is the Reynolds number based on mean velocity

(U_m) and boundary layer thickness (δ), ν_τ is the eddy viscosity in the LES model. The over-bar represents a time average. The terms on the right hand side of Eq. D.1 are: convection (C_k), production (P_k), turbulence transport (T_k), viscous diffusion (D_k), viscous dissipation (ϵ_k) and velocity-pressure gradient (Π_k).

Fig. 3.12 depicts the absolute ratio of turbulent kinetic energy (TKE) production to dissipation terms (P_k/ϵ_k) in the $y-z$ plane at three stream-wise locations. The ratio P_k/ϵ_k helps us to quantify the departure from the state of equilibrium. In a turbulent flow, equilibrium is defined as the state in which the production of TKE is balanced by dissipation, therefore, large values of P_k/ϵ_k represent regions of greater non-equilibrium. In Fig. 3.12 we observe that the P_k/ϵ_k values decrease with decreasing cube heights. The contribution to the production term ($\overline{(u_l'u_k')}U_{l,k}$) comes from the gradient of velocity tensor and the Reynolds stress tensor. The no-slip boundary condition imposed on the surface of the cube results in large velocity gradients which in turn is responsible for the increased production of TKE. A bigger cube results in larger velocity gradients, and therefore, large values of P_k/ϵ_k. At $x = 0.5h$ in Fig. 3.12a - 3.12c we observe a region of high P_k/ϵ_k around the surface of the cube. In case of $h/\delta_o = 1.0$, we observe a region of large P_k/ϵ_k at $y \approx 1.4$ to 2.2, and the reason for this increase in the ratio is explained later. As we move along the stream-wise direction at $x = 3h$ and $x = 6h$, we observe an increase in P_k/ϵ_k at the center of the horse-shoe vortex at $z \approx h$, and a relatively smaller magnitude of the ratio in the center of the domain behind the cube. We learned in Sec. 3.3.4 that the span-wise gradient of velocity ($\partial U/\partial z$) is zero at the center of the domain therefore, the only term contributing to P_k in the center-plane is $\overline{u'v'}U_{x,y}$. On the other hand, in the center of the horse-shoe vortex, the $\overline{u'w'}U_{x,z}$ term also contributes the production of TKE. This term is a result of span-wise turbulent transport of momentum caused by the counter-rotating vortex pair.

To understand the large increase in P_k/ϵ_k for $h/\delta_o = 1.0$ between $y/h \approx 1.4$ and 2.2 in Fig. 3.12c and 3.12f, we look at the distribution of the terms individually in the center-plane of the domain in Fig. 3.13. We observe that the regions with $P_k > \epsilon_k$ are present in front

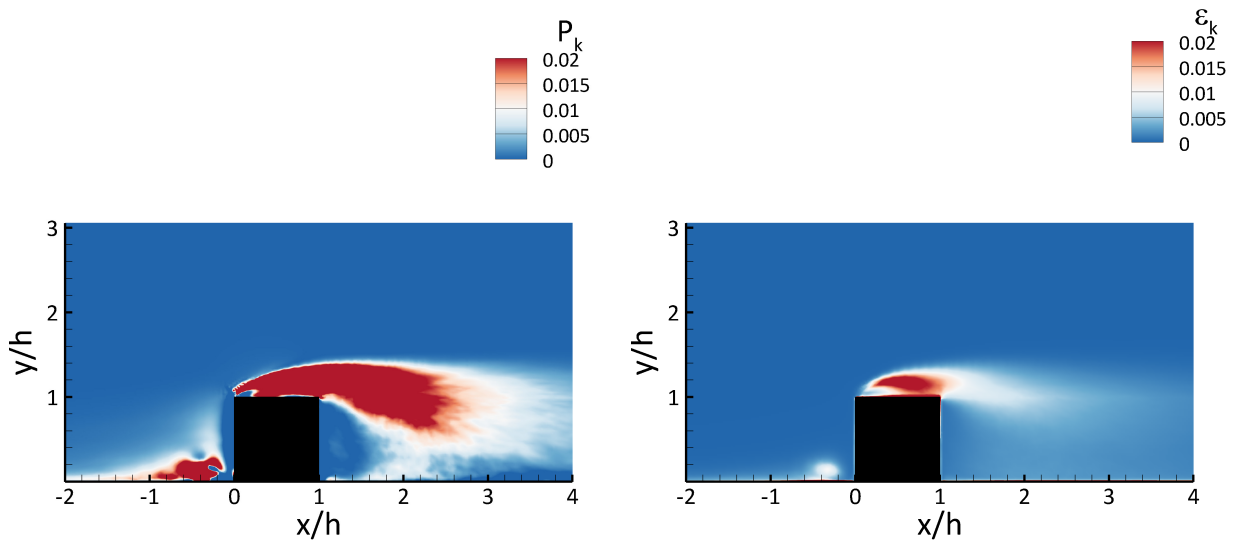

(a) Production term (P_k) (b) Absolute value of the dissipation term (ϵ_k)

Figure 3.13: Contours of the production term and absolute value of the dissipation term from the TKE budget of $h/\delta_o = 1.0$ in the center-plane.

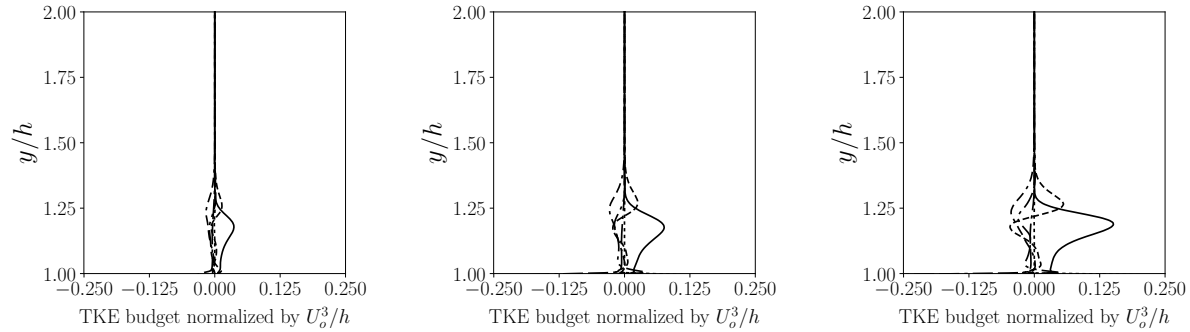

(a) $h/\delta_o = 0.2$ (b) $h/\delta_o = 0.6$ (c) $h/\delta_o = 1.0$

Figure 3.14: Normalized span-wise averaged terms on the right hand side of the TKE budget equation at $x = 0.5h$: – – - - -, convection; ———, production; ------, turbulence transport; ·····, viscous diffusion; — · —, viscous dissipation; — · · —, velocity-pressure gradient.

of the cube at the center of the horse-shoe vortex, and inside the shear-layer emanating from the front edge of the cube. This is because the major contribution to the production term comes from the velocity gradient tensor, whereas the dissipation term depends on the gradient of velocity fluctuations which are an order of magnitude smaller than the gradients in velocity. At the height of $y/h \approx 1.4$ to 2.2 we notice that both P_k and ϵ_k have negligible magnitudes, and therefore, the large increase in P_k/ϵ_k at that height is a numerical artifact

of dividing a small value of P_k by an order of magnitude smaller value of ϵ_k. The regions where P_k is not balanced by ϵ_k are recognized as regions of non-equilibrium.

We examine the normalized, span-averaged terms on the right-hand-side of TKE budget equation at $x = 0.5h$ in Fig. 3.14. The magnitude of each term increases with increasing cube height on account of the increased gradients across the shear-layer. A large spike in the production term is observed at $y \approx 1.2h$, which lies inside the shear layer. This spike correlates with the location of the negative spike in the transport term, indicating the transfer of TKE from the shear layer to regions close to cube top-wall and away from the shear-layer. The magnitude of dissipation inside the shear layer is negligible relative to the that of the production term, thereby implying non-equilibrium. The commonly used assumption in the eddy viscosity parameterization, that production is balanced by dissipation, is not applicable in this region, further justifying the use of the dynamic $k-$equation LES model. The convective term shows a distinct negative peak inside the shear layer, which implies that the velocity and gradient of TKE point in the same direction at $x = 0.5h$. We can therefore conclude that the magnitude of the TKE decreases in the stream-wise direction on the top of the cube.

Fig. 3.15 depicts the normalized, span-averaged TKE budget at $x = 2h$; outer coordinates are used in Fig. 3.15a - 3.15c, and inner coordinates in Fig. 3.15d - 3.15f. The reason to normalize the TKE budget terms using the outer and inner coordinates separately is that the large scale outer structures are governed by the outer variables (mean velocity U_o, and cube height h), whereas the near-wall behavior is governed by the inner variables (friction velocity u_τ, and kinematic viscosity ν). This plane lies just after the point of reattachment behind the cube. In the outer region we observe that the magnitude of the production term, and the location of its peak value inside the shear layer increases with increasing cube height. The profile of the production term in the outer region has two distinct peaks; first, near the wall, and second, away from the wall inside the shear layer. The peak inside the shear layer is mainly due to the contribution of $\overline{u'v'}\partial U/\partial y$ to the longitudinal stress, P_{11}. This observation

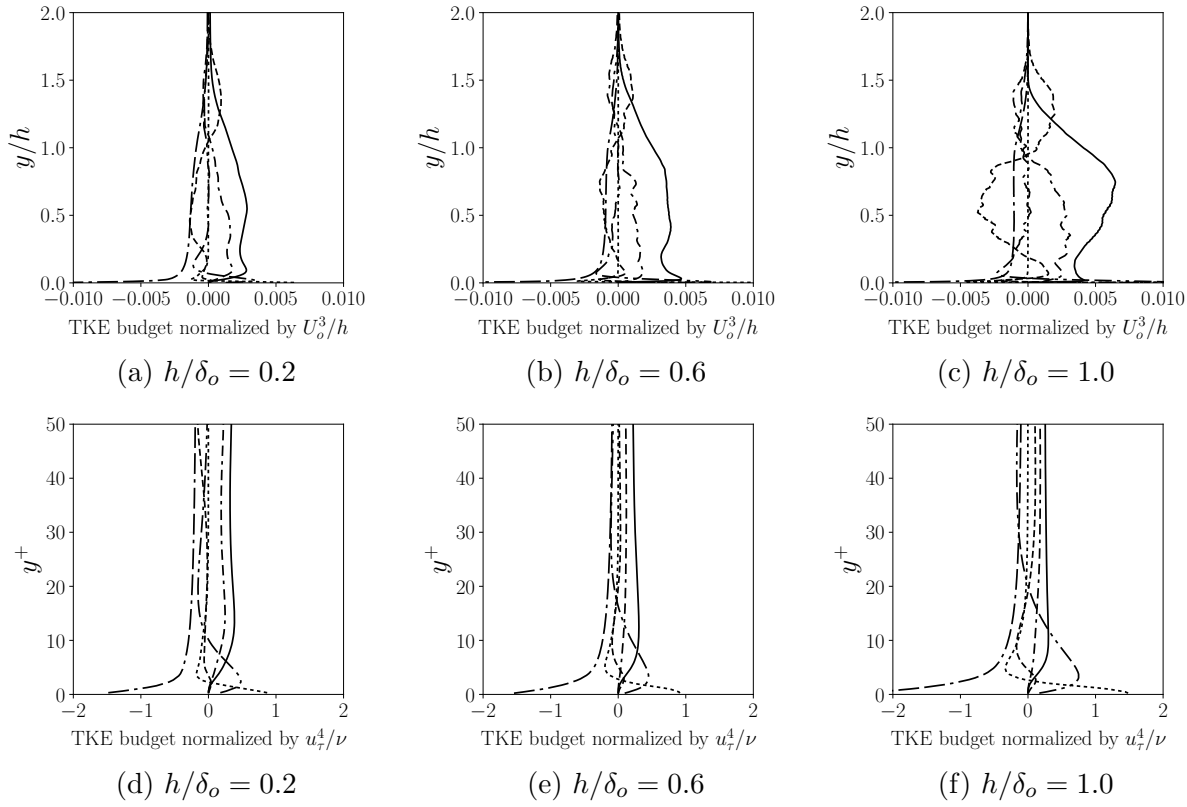

(a) $h/\delta_o = 0.2$ (b) $h/\delta_o = 0.6$ (c) $h/\delta_o = 1.0$

(d) $h/\delta_o = 0.2$ (e) $h/\delta_o = 0.6$ (f) $h/\delta_o = 1.0$

Figure 3.15: Normalized span-averaged terms on the right-hand-side of the TKE budget equation at $x/h = 3$: – – - – -, convection; ———, production; ------, turbulence transport; ·····, viscous diffusion; — · —, viscous dissipation; — · · —, velocity-pressure gradient.

is similar to that of a shear layer formed from a backward facing step [118] although, there is an enhancement in the production term close to the wall in our case. We observed in Sec. 3.3.4 that near the wall at the center of the horse-shoe vortex the $\overline{u'w'}\partial U/\partial z$ term has a significant magnitude, which also contributes to increased production along with the $\overline{u'v'}\partial U/\partial y$ term. Peak value of the production term is not balanced by the dissipation term, implying non-equilibrium. The transport term continues to transfer energy from the shear layer to the low-speed and the high-speed sides of the shear layer, with greater magnitudes in case of the $h/\delta_o = 1.0$. The convective term has become positive inside $y/h < 1.0$, from a distinct negative value seen in Fig. 3.14. This positive value implies that the direction of velocity and the direction of TKE gradient vectors are opposite. TKE introduced in the flow by the cube is convected in the stream-wise direction, to the near-wall region and towards the

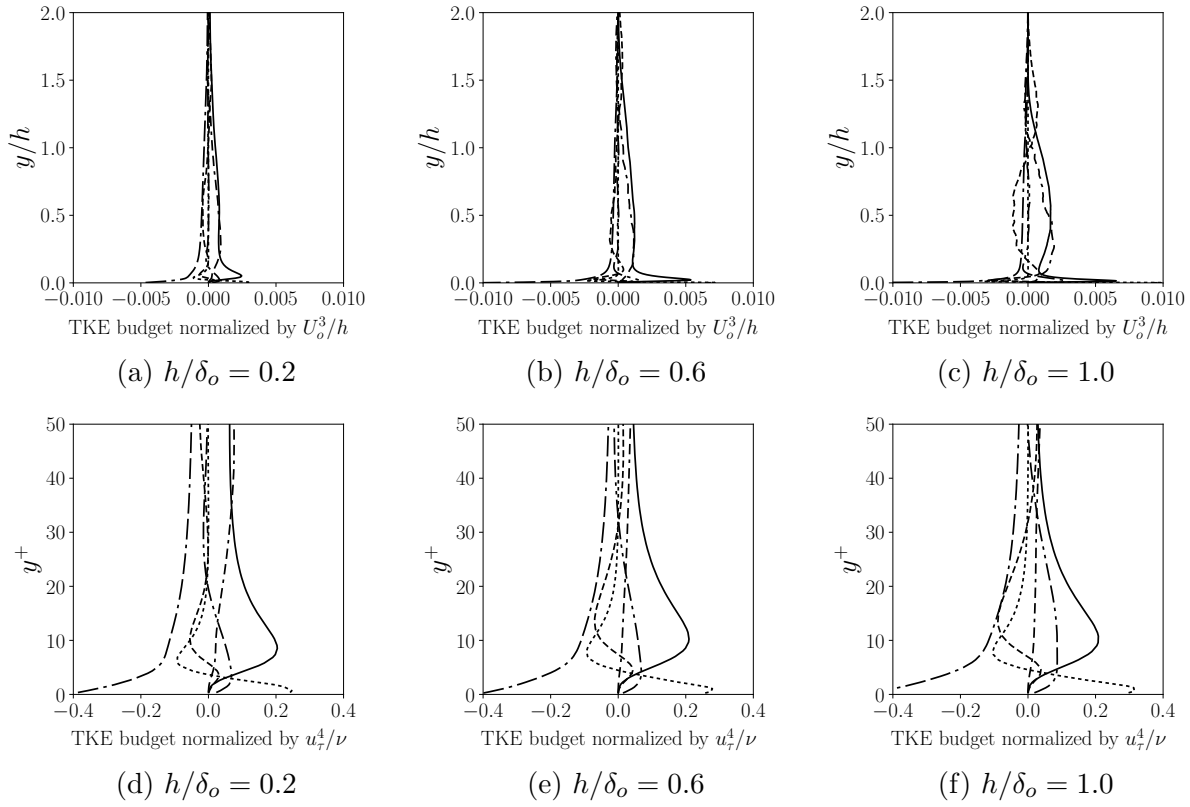

(a) $h/\delta_o = 0.2$ (b) $h/\delta_o = 0.6$ (c) $h/\delta_o = 1.0$

(d) $h/\delta_o = 0.2$ (e) $h/\delta_o = 0.6$ (f) $h/\delta_o = 1.0$

Figure 3.16: Normalized span-averaged terms on the right-hand-side of the TKE budget equation at $x/h = 6$: – – - - -, convection; ———, production; ------, turbulence transport; ·····, viscous diffusion; — · —, viscous dissipation; — · · —, velocity-pressure gradient.

center-plane of the domain. In the region close to the wall in Fig. 3.15d - 3.15f, we observe that dissipation dominates as expected. However, the velocity-pressure gradient term has a large magnitude at $y^+ < 5$. The adverse pressure gradient gives rise to the large spike in Π_k.

We investigate the TKE budgets in the recovery region in Fig. 3.16. We observe a sharp decrease in the magnitude of P_k inside the shear layer compared to Fig. 3.15. This drop is mainly due to the transport of TKE to the regions away from the shear layer. However, this drop is not as significant near the wall because the velocity gradients which contribute to P_k, are still strong. Comparing the profiles to those corresponding to a zero-pressure-gradient flat plate boundary layer [118], the recovery of the boundary layer is more effective in $h/\delta_o = 0.2$ case, compared to that of the larger cubes. The magnitude of P_k is balanced closely by ϵ_k for $h/\delta_o = 0.2$ for $y > 0.2h$. The TKE budget profiles look identical to the zero-pressure

gradient boundary layer for the three cube heights in the inner region, indicating that the boundary layer has recovered in the near-wall region. However, the recovery of the TBL is incomplete in the outer region at $x = 6h$, for $h/\delta_o = 0.6$ and 1.0 because: (i) the transport term has a non-zero magnitude for $h/\delta_o = 1.0$ in the outer region, indicating transport of TKE from the shear to the low-speed and high-speed sides of the shear layer, (ii) a large spike in the production term close to wall, and (iii) non-zero value of the convection term, with a peak at $y \approx 0.5h$.

3.4 Conclusions

Wall-resolved large eddy simulations of a wall-mounted cube placed inside a spatially evolving turbulent boundary layer (SETBL) are performed. The Reynolds number of the flow based on mean velocity and incoming boundary layer thickness is 19,600. The key novelty of this work is the use of SETBL to analyze the effect of varying the cube height (h) to boundary layer thickness ratio (δ_o) on the near-wake characteristics. Separation distances and reattachment lengths are similar to those observed in previous experiments and direct numerical simulations of a cube in a fully developed channel flow. We observe that the size of the recirculation region behind the cube scales with the cube height (h), which is in agreement with previous studies [119, 61]. On the other hand, mean vorticity contours indicate that several properties of the horse-shoe vortex depend on h/δ_o. For $h/\delta_o = 0.6$ and 1.0, the horse-shoe vortex extends to $0.2y/h$ and $1.2z/h$, whereas, for $h/\delta_o = 0.2$, it extends to $0.3y/h$ and $1.3z/h$. The slower rate of spreading of the horse-shoe for larger cubes is attributed to the presence of a strong, span-wise pressure gradient. The strength of the horse-shoe vortex decreases with decreasing cube height and in the stream-wise direction, as the velocity behind the cube increases with decreasing lateral pressure gradients.

The turbulent kinetic energy (TKE) per unit area exhibits a power law decay in the near-wake for all the h/δ_o ratios, and the power law exponent increases in a non-linear fashion with increasing h/δ_o. We believe this observation is a near-wake phenomenon, similar to

the observations of Hussein *et al.* [11] for flow over a cube in a turbulent channel. A larger cube results in stronger gradients in velocity, which in turn leads to greater production of TKE. The production of TKE is not balanced by its dissipation inside the shear layer in the wake and this imbalance is a measure of the departure from the state of equilibrium. The greater decay rate facilitates a faster recovery of the TBL, as it transitions to equilibrium. An investigation of the TKE budget indicates that the TKE production to dissipation ratio (P_k/ϵ_k) increases inside the shear layer emanating from the top surface of the cube. This ratio also increases with increasing h/δ_o. This behavior is explained by the large velocity gradients inside the shear layer for larger cube heights. A detailed look at the TKE budget terms reveals high values of P_k close to the wall on account of the near-wall velocity gradients, but these high levels are overshadowed by far greater viscous dissipation. The shear layer transports TKE to regions close to the wall and away from the shear layer as the boundary layer recovers. The recovery of the turbulent boundary layer is not complete at $x = 6h$, as exemplified by large values of transport and convection due to the opposite nature of velocity and TKE gradient vectors inside the boundary layer.

CHAPTER IV

Understanding the dependence of near-wake characteristics on the spacing between adjacent cubes in a turbulent boundary layer

4.1 Introduction

Flow over wall-mounted cubes has been an active research topic for decades. The cube has been studied in an open channel to mimic external flow scenarios, as well as in a closed channel to represent internal flow configurations. The need to understand air flow over buildings or flow over objects mounted on moving bodies (e.g., aircraft, automobile, submarine, etc.) has motivated researchers to study flow over a wall-mounted cube in an open channel. Furthermore, gaining a deeper understanding of physics of flow over a cube in a fully developed channel flow has implications in designing of circuit boards, heat exchangers with cooling fins, turbines with rotor and blades, etc.

For a single cube placed in a turbulent boundary layer (TBL) the relevant parameters that affect the flow physics are the cube height to boundary layer thickness ratio (h/δ) [108], Reynolds number based on the cube height and mean flow velocity (Re_h), level of free-stream turbulence (FST) [119], and the orientation of the cube with respect to the flow direction. Researchers have investigated the influence of each of these parameters on the flow physics through experimental [108, 54, 11] and numerical studies [59, 12, 61]. Castro *et al.*

[108] investigated the effect of upstream turbulence and shear on the wake characteristics for changing cube height (h) to boundary layer thickness ratio (δ), where h/δ varied from 0.1 to 2.3. They concluded that for $h/\delta \lesssim 0.7$ the reattachment length achieved a certain degree of Reynolds number independence. Varying the h/δ ratio and keeping the TBL properties constant led to the cube intersecting the TBL at different locations, which in turn varied with the level of turbulence at the cube height. They postulated that the wake properties should depend on the shear layer formed on the top surface of the cube. Martinuzzi *et al.* [54] varied the aspect ratio (W/H) from 1 to 24 for flow over an obstacle placed in fully developed channel flow. The obstacle height was half channel height and the Reynolds number of the flow was 40,000. They discovered that the for $W/H > 6$ the wake of the obstacle was nominally two-dimensional. For flow over a single cube in a turbulent channel flow with $h = 0.5H$, where H is the channel height, and a $Re_h = 40,000$, Hussein *et al.* [11] investigated the TKE budget in the center-plane in the wake of cube and concluded that the production and dissipation terms of TKE budget decay in a power law manner in the plane of symmetry. Hearst *et al.* [119] investigated the effect of varying free-stream turbulence on the wake characteristics for a cube placed in a SETBL for $h/\delta = 0.5$. They observed a monotonic reduction in the wake length with increasing free-stream turbulence. Aforementioned studies and several others [120, 121, 122] also report the existence of time-averaged flow features like the horse-shoe vortex formed in front of the cube, the arch-type vortex formed in the wake of the cube, and the hair-pin vortices on the top surface.

With the increase in computational power in the past two decades, scientists have used numerical methods to study the fluid mechanics in this complex problem. A variety of numerical approaches like Reynolds-Averaged Navier-Stokes (RANS), detached-eddy simulation (DES), large-eddy simulation (LES), and direct numerical simulation (DNS) have been used. Krajnovic *et al.* [59, 12] performed LES of flow over a cube placed inside a fully developed channel flow at a Reynolds number of $40,000$, where the cube height was half the channel height. They surveyed different LES models and concluded that the one-equation

LES model is better capable to capture the non-equilibrium turbulent flow around the cube than the Smagorinsky model. Yakhot *et al.* [61, 10] in their DNS of the same flow configuration, but at a lower Reynolds number of 1870 (based on the cube height and mean velocity), reported negative turbulence production in the region in front of the cube, and attributed the unsteadiness observed in the flow to the viscous-inviscid interaction between the horse-shoe vortex and a narrow band of positive vorticity in front of the cube. Liakos *et al.* [60] studied the onset of unsteadiness in the flow as it transitions from laminar to turbulent flow regimes for $h = 0.1H$, where H is the channel height. From these studies it is clear that DNS of this flow configuration at high Reynolds number is still beyond our computational grasp. LES is the most accurate numerical alternative for tackling this problem, and hence the preferred tool for investigation in this study.

In addition to the parameter discussed above for turbulent flow over an array of cube-like objects stretching in the stream-wise, span-wise, or both the directions the spacing between these objects also affects the flow physics. To understand the atmospheric boundary layer flow over an urban landscape (Belcher *et al.* [68], Lee *et al.* [75], Coceal *et al.* [69]), past work investigated the flow over an array of obstacles stretching in the stream-wise and span-wise directions on smooth walls. The height of the obstacles is much smaller as compared to the boundary layer thickness, with height $h < 0.2\delta$, causing minimal interaction of the cube-like obstacles with the large-scale and very-large-scale structures in the outer region of the TBL. On the other hand, for $h < 0.1\delta$, researchers treated the array of obstacles as a rough surface, and investigated the effect of roughness on the coherent structures in a TBL (Tomkins *et al.* [123], Orlandi *et al.* [124]). However, the effect of spacing between adjacent cubes on the interaction between horse-shoe vortices, and its effect on the turbulent kinetic energy (TKE) distribution in the near-wake is poorly understood. A deeper understanding of the effect of spacing between adjacent cubes on TKE distribution can be leveraged to control flow separation on aircrafts, automobiles, turbo-machineries, etc. Therefore, in the present work we consider a single row of cubes in a turbulent boundary layer, and study

the near-wake characteristics. An infinite line of cubes placed adjacent to each other and normal to the flow direction is replicated using periodic boundary conditions in the span-wise direction. The cube height is equal to the boundary layer thickness at its front face, causing a significant perturbation of the large-scale structures in the boundary layer. In Chapter III we considered the turbulent wake characteristics of a single cube in a spatially evolving turbulent boundary layer for varying h/δ. We discovered that the decay of TKE area density obeys a power law equation, and the power law exponent increases in a non-linear manner with increasing h/δ. In this chapter, we investigate the effect of interaction between vortices from adjacent cubes on the near-wake behavior when an infinite line of cubes is placed normal to the flow direction. We expect that the power law decay of the TKE area density holds true for regions close to the cube in its wake, before the horse-shoe vortices from adjacent cubes interact with each other. We further expect an increase in the TKE area density after the onset of these interactions.

4.2 Computational approach

4.2.1 Geometry and mesh

We simulate a SETBL over a flat plate of length $18\delta_o$, where δ_o is the boundary layer thickness at the inlet boundary. As illustrated in Fig. 4.1, a cube of height $h = \delta_o$ is placed at a distance of $12\delta_o$ from the inlet boundary, and the reason for choosing this distance is explained later. The height of the domain is $5\delta_o$, so that we can capture all the effects of the turbulent shear layer formed on top of the cube, at the same time avoid any influence of the top-wall on the vortices generated by the cube. To examine the effect of spacing between adjacent cubes on the near-wake, we vary the width (w) of the computational domain with periodic span-wise boundary conditions. In the present work we consider three different domain widths, so that w/h is 3, 5, and 7. The dotted lines in Fig. 4.1 represent a infinite repetition of the computational domain on both sides, achieved via a cyclic boundary

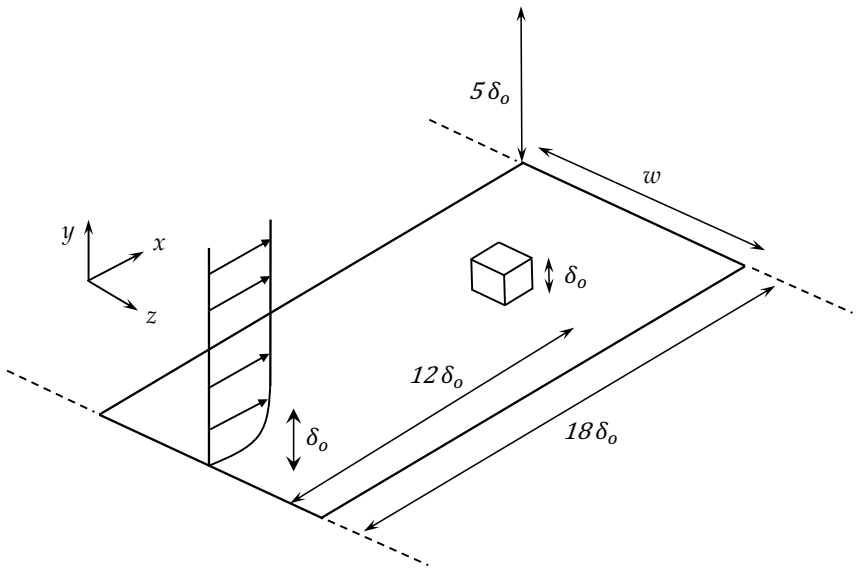

Figure 4.1: Problem setup.

condition imposed on the side-walls. The SETBL is simulated using a time-varying inflow boundary condition (Sec. 2.4.2) for the velocity field at the inlet, with a free-stream turbulence of 1%. The time-varying inflow field does not obey the filtered Navier-Stokes equations at the inlet and requires a transition length of $12\delta_o$ to regain the boundary layer thickness and develop into a realistic TBL. Hence, the cube is placed at a distance of $12\delta_o$ from the inflow boundary. In the absence of the cube, the boundary layer thickness at $x = 12\delta_o$ is also δ_o.

The Reynolds number (Re_h) of the flow is 19,600 based on the mean velocity and the cube height, whereas the Reynolds number (Re_τ) based on friction velocity (u_τ) and the cube height is 800. The choice of the Reynolds number is influenced by two factors: (i) it should be small enough, so that it is feasible to perform wall-resolved LES, and (ii) it should be large enough for our results to be Reynolds number independent. Castro *et al.* [108] found that there are no discernible Reynolds number effects of incoming turbulent conditions if $Re_h > 4000$, and the Re_h in this study is an order of magnitude higher. The bottom-wall and the cube surface are treated as no-slip walls, and a zero-gradient boundary condition is used at the outlet. As demonstrated in Fig. 4.2, the mesh is non-uniform with smaller

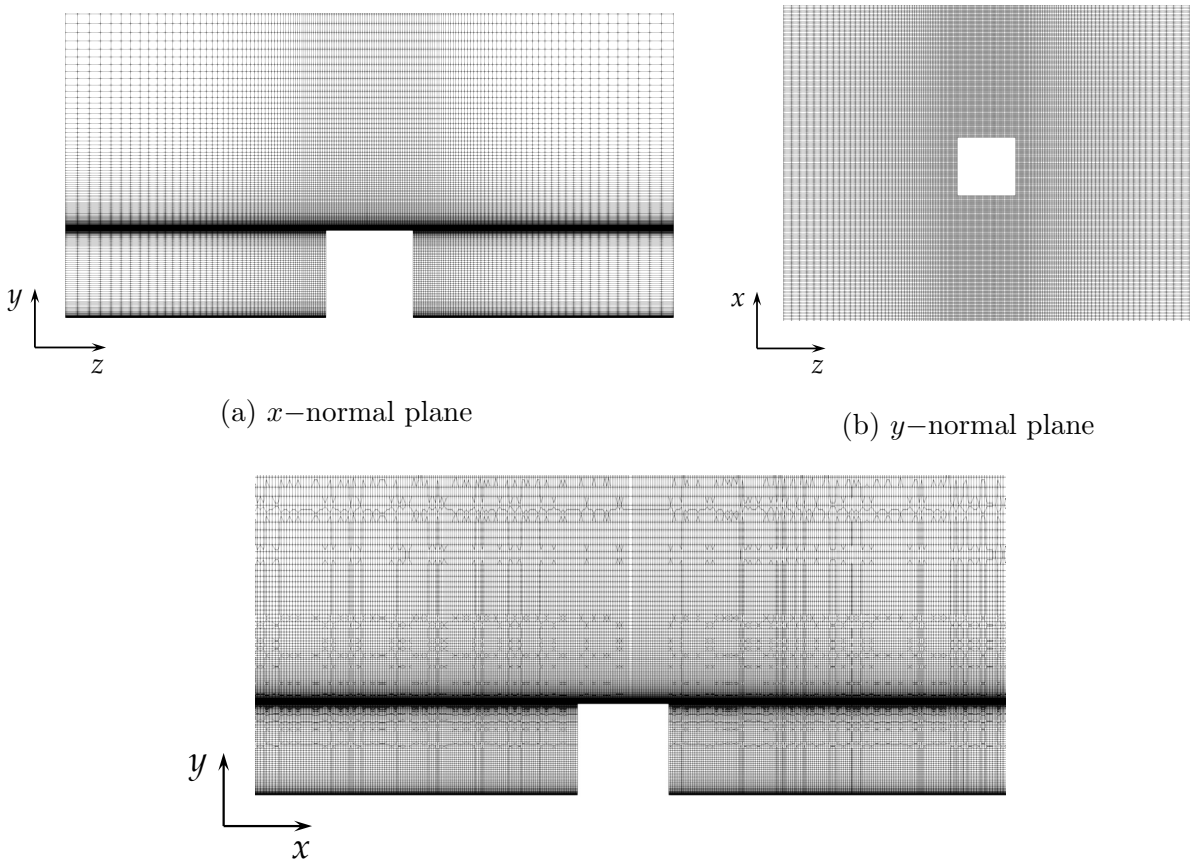

(a) $x-$normal plane

(b) $y-$normal plane

(c) $z-$normal plane

Figure 4.2: Computational grid for $w = 7h$.

cells near the bottom-wall and the cube, and larger cells away from the wall and towards the periphery of the domain. A grid convergence study is performed using three (coarse, medium, fine) different mesh resolutions for the $w = 7h$ case, and the results are presented in Appendix C. From this study we conclude that grid independence is achieved on the fine mesh. The cell spacings for the three grids are reported in Table 3.1.

4.2.2 Numerical methods

The incompressible filtered Navier-Stokes equations are solved with a finite volume approach using the OpenFOAM libraries [77]. The effect of the sub-grid scales is accounted for with the dynamic $k-$equation eddy-viscosity LES model [81]. The reason to use this model

is its ability to capture back-scatter of turbulent kinetic energy[1], a phenomenon observed in the region in front of the cube [12]. This model can also accurately simulate the periodicity of the vortices formed around the cube [12]. A second-order central scheme is used for the viscous and pressure terms, whereas as the LUST (Linear Upwind Stabilized Transport) [84] scheme is used to discretize the convection term. LUST scheme a linear combination of the central and linear upwind schemes with weights 0.75 and 0.25 respectively. Mittal *et al.* [87] reported that for LES of turbulent flows, the computational grids and boundary conditions should be designed with extreme care when using a central scheme for the convective term. To overcome this problem, a more robust LUST scheme is used in the present work. The solution is advanced in time using a second-order implicit backward time-marching scheme. The numerical framework is validated by comparing its accuracy with experimental results for flow over a cube in a turbulent channel flow (Appendix C). The simulations are carried out for a total time period of $1100\delta_o/U_m$ with variable time-step and a maximum Courant number of 1. The turbulent statistics are averaged starting from $100\delta_o/U_m$ for a time period of $1000\delta_o/U_m$, to avoid contamination of the results by the initial transient.

4.3 Results and discussion

The basic flow features described in Sec. 3.3.1 for flow over a single cube in a SETBL like the horse-shoe vortex formed around the front-face of cube, the lateral vortices formed on the sides of the cube, and the vortex shedding from the top surface of the cube, are also observed in case of multiple cubes. It is difficult to quantify the effect of w/h on these flow features by examining volumetric distribution of quantities. Therefore, in this section we focus our attention on line and contour plots of quantities of interest, to understand the dependence of the near-wake characteristics on the inter-cube spacing.

[1]Back-scatter of turbulent kinetic energy is a phenomenon in which energy is transferred from the smaller scales to the larger scales in a direction opposite to that of the energy cascade in an equilibrium TBL.

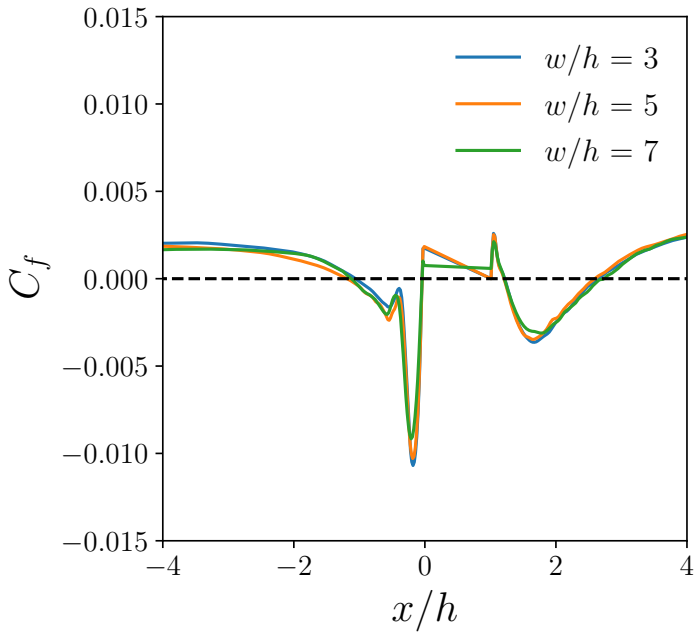

Figure 4.3: Skin friction coefficient vs. normalized stream-wise coordinate.

4.3.1 Separation and reattachment lengths

In Fig. 4.3, we depict the variation of the skin-friction coefficient (C_f) along the bottom-wall of the domain in the center-plane for the three cube spacings. C_f is defined by Eq. 4.1,

$$C_f = \frac{\tau_w}{\frac{1}{2}\rho U_\infty^2} \qquad \tau_w = \mu\left(\frac{\partial u}{\partial y}\right)_{y=0} \tag{4.1}$$

where, τ_w is the wall shear stress, ρ is the fluid density, U_∞ is the free-stream velocity of the fluid, μ is the dynamic viscosity of the fluid, u is the fluid velocity parallel to the bottom-wall, and y is the wall-normal coordinate. C_f gives a measure of the velocity gradient close to the wall. We observe a similar variation of C_f in the three cases. In the region in front of the cube, C_f is almost constant up to $x \approx -2h$, because the TBL is attached to the bottom-wall. Close to the front face of the cube the flow separates from the bottom-wall at distance of $X_s = 1.3h$ from the front face, where X_s is the separation length. The separated region is marked by a negative value of C_f which is a result of the negative stream-wise

velocity component in the region occupied by the horse-shoe vortex [12]. The recirculation region also identified by negative value of C_f is located immediately downstream of the cube. The flow reattaches at a distance of $X_r = 1.6h$, where X_r is the reattachment length. X_r is measured as the distance from the back-face of the cube to a point where $C_f = 0$. The separation and reattachment lengths are unaffected by the inter-cube spacing in the span-wise direction for the spacings considered in this study. X_s and X_r are controlled by the horse-shoe vortex in front of the cube and the shear-layer emanating from the top surface of the cube. We know from our study of flow over a single cube that these flow features scale with the cube height (Sec. 3.3.2). The inter-cube spacing (w) is much greater than h even for $w = 3h$. As a result there are negligible interactions between vortices from adjacent cubes in the immediate vicinity of the cube. Hence, X_s and X_r are unaffected by w/h.

4.3.2 Mean velocity and Reynolds stress

To understand the dependence of mean velocity and turbulent transport of momentum in the span-wise direction on varying w/h in Fig. 4.4 and 4.5, we examine the mean velocity and Reynolds stress profiles near the end of the domain at $x = 5.5h$ and at half cube height from the bottom-wall. For the $w = 7h$ case, the variation of the stream-wise component of mean velocity is different than that observed in case of a single cube with $w = 7h$ and slip boundary conditions on the side-walls. The magnitude of the velocity is mostly uniform with small peaks toward the edge of the domain because the cube forces high speed fluid to the periphery of the domain, and the region behind the cube is characterized by low momentum flow. The variation of U_x informs us that the outer flow has not completely recovered at $x = 5.5h$. A similar behavior is observed for the $w = 5h$ case, whereas for $w = 3h$ the peak velocity lies at the center of the domain. Pujals *et al.* [8] observed a sine wave-like variation in the mean velocity in the wake of periodically spaced cylinders with a spacing of $\lambda_z = 4d$, where λ_z is the spacing between adjacent cylinders, and d is the diameter of the cylinders. At a stream-wise distance of $4\lambda_z$ in the wake of the cylinders,

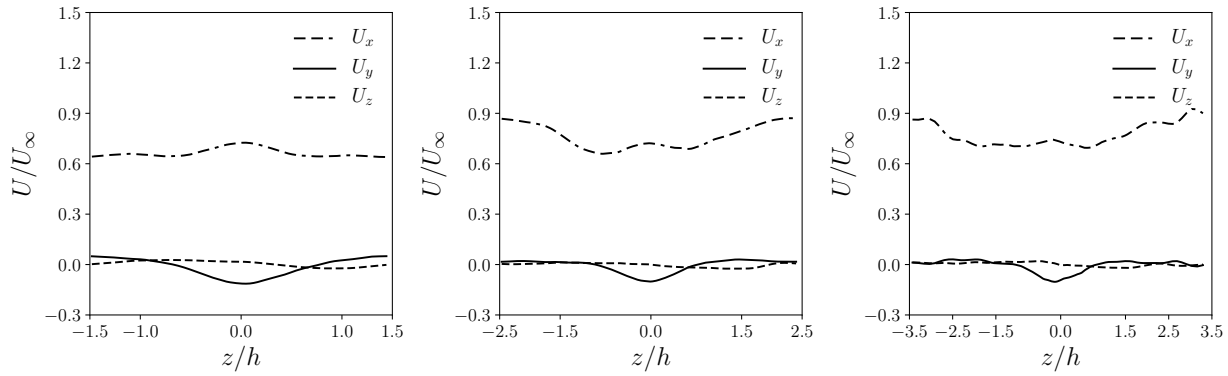

(a) $w = 3h$ (b) $w = 5h$ (c) $w = 7h$

Figure 4.4: Normalized mean velocity vs. normalized span-wise coordinate at $x = 5.5h$ in the stream-wise direction and $y = 0.5h$ in the wall-normal direction.

they observed a peak in the mean velocity (approximately $0.9U_\infty$), and a trough in between the cylinders (approximately $0.7U_\infty$). We believe the behavior observed in the Fig. 4.4 is a precursor to the sine variation, with a small peak appearing at the center of the domain in all the cases. The stream-wise length of the domain is insufficient to reflect the full interaction between vortices from adjacent cubes, and a longer domain length would help us capture the sine variation of the mean velocity. The $y-$component of velocity exhibits a similar variation in all the cases, with a negative peak at the center of the domain. The negative peak corresponds to the entrainment of high-momentum fluid from the outer region to the near-wall region by the shear layer and the counter-rotating vortices present in the wake of the cube. For $w = 3h$, the $y-$component of mean velocity is slightly positive in the periphery of the domain, whereas it is zero in the other two cases. This implies a net ejection of low momentum fluid to the outer region. These ejections could be responsible for the amplification of outer scales motions with a span-wise spacing of approximately $3h$, as explained in detail in subsequent sections.

The Reynolds stress components on the other hand illustrate similar behavior along the span-wise direction for all cases. The $\overline{u'^2}$ and $\overline{u'w'}$ components have a peak value at the center of the horse-shoe vortex at $z \approx \pm 1.2h$, and the value decays in both directions away from the center of the vortex. This variation is similar to that observed in case of a single

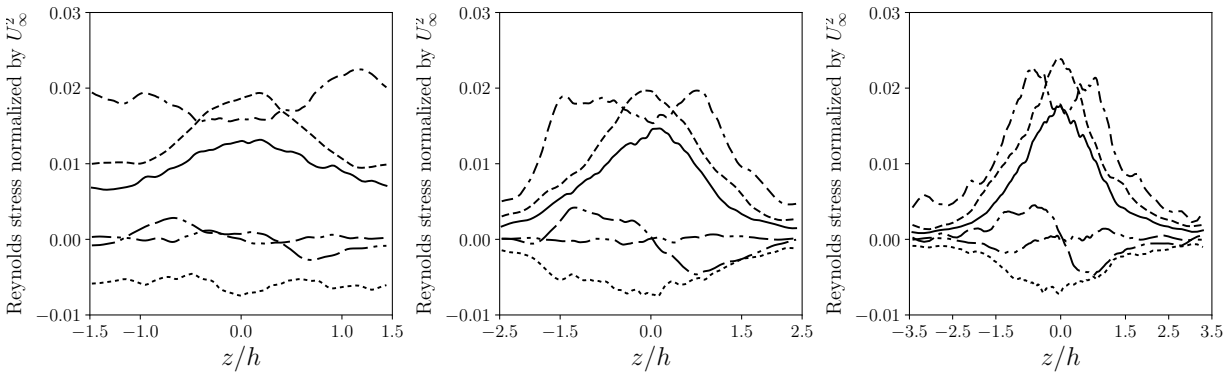

(a) $w = 3h$ (b) $w = 5h$ (c) $w = 7h$

Figure 4.5: Normalized Reynolds stresses vs. normalized span-wise coordinate at $x = 5.5h$ and $y = 0.5h$. – – - – -, $\overline{u'^2}$; ———, $\overline{v'^2}$; - - - - - -, $\overline{w'^2}$; ·····, $\overline{u'v'}$; — · —, $\overline{u'w'}$; — · · —, $\overline{v'w'}$.

cube (Sec. 3.3.4), and the reason is a strong coupling between the $\overline{u'}$ and the $\overline{w'}$ components inside the horse-shoe vortex. The $\overline{v'^2}$, $\overline{w'^2}$ and $\overline{u'v'}$ components exhibit a peak at the center of the domain because of the wall-normal and the span-wise turbulent transport of momentum to the near-wall region and the center-plane. In case of $w = 3h$, the $\overline{u'v'}$ component has an almost constant negative value across the domain. The negative correlation between the $\overline{u'}$ and the $\overline{v'}$ components is due to the "sweep" of high momentum fluid to the near-wall region and the "ejection" of low momentum fluid to the outer region [25] in a TBL. The downward sweep of high momentum to the near-wall region in the center-plane is responsible for the negative value of $\overline{u'v'}$ at the center of the domain in all the cases. For $w = 3h$, the exact reason for the large value of $\overline{u'v'}$ observed at the edge of the domain in the span-wise direction is not known. The ejection of low-momentum fluid to the outer region observed toward the edge of the domain in Fig. 4.4a could be responsible for the negative value.

The normalized velocity profiles depicted in Fig. 4.6 and Fig. 4.7 exhibit an similar behavior for the three cases. The boundary layer thickness is greater in the center-plane ($\delta \approx 1.5h$) as compared to its value at $z = h$ ($\delta \approx 1.2h$). The velocity profiles in the center-plane have not recovered completely from the momentum deficit created by the presence of the cube, as indicated by a higher value of the boundary layer thickness. The mean velocity profiles do not match with those in an equilibrium TBL because of the non-zero U_y and

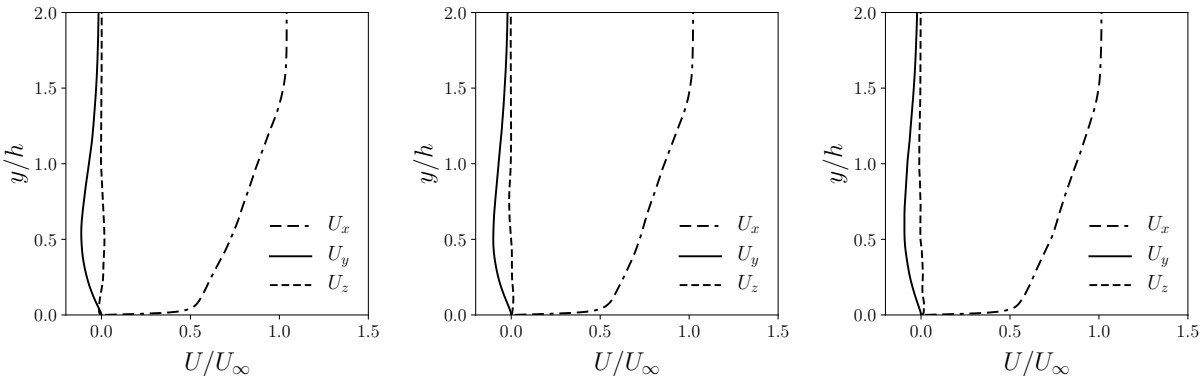

(a) $w = 3h$ (b) $w = 5h$ (c) $w = 7h$

Figure 4.6: Normalized mean velocity vs. normalized wall-normal coordinate at $x = 5.5h$ in the stream-wise direction and in the center-plane ($z = 0$).

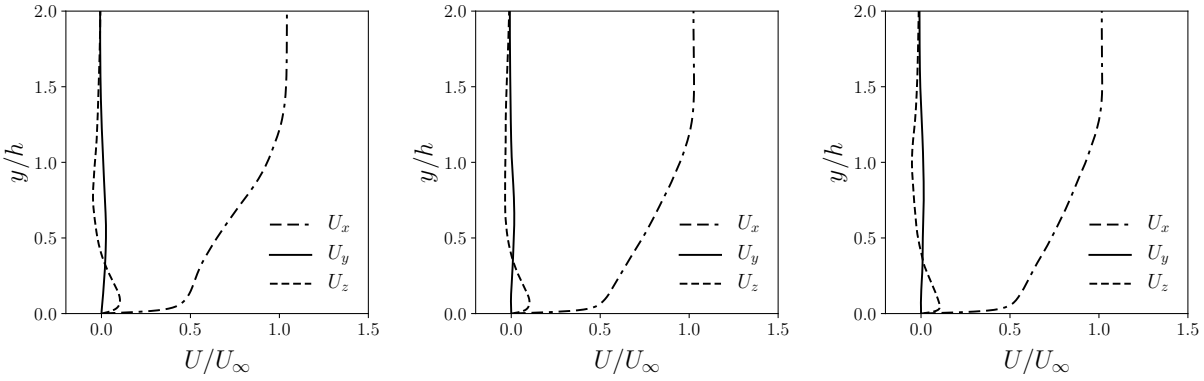

(a) $w = 3h$ (b) $w = 5h$ (c) $w = 7h$

Figure 4.7: Normalized mean velocity vs. normalized wall-normal coordinate at $x = 5.5h$ in the stream-wise direction and at $z = h$ in the span-wise direction.

U_z components. In the center-plane, the entrainment of high momentum fluid to the near wall region is indicated by the negative U_y component. The U_z component is zero because there is no net transfer of fluid from the center-plane to the periphery of the domain, and vice-versa. In Fig. 4.7, the U_z component of velocity shows an inflection point as the mean span-wise velocity on the two sides of the center of the horse-shoe vortex points in opposite directions. The center of the horse-shoe vortex is at $y \approx 0.4h$, where U_z is zero.

In Fig. 4.8 and 4.9, we present the variation of Reynolds stresses in the wall-normal direction at $z = 0$ and $z = h$ respectively. The former demonstrates, that the magnitude of the $\overline{w'}$ component is greater than the $\overline{u'}$ component, unlike that observed in an equilibrium

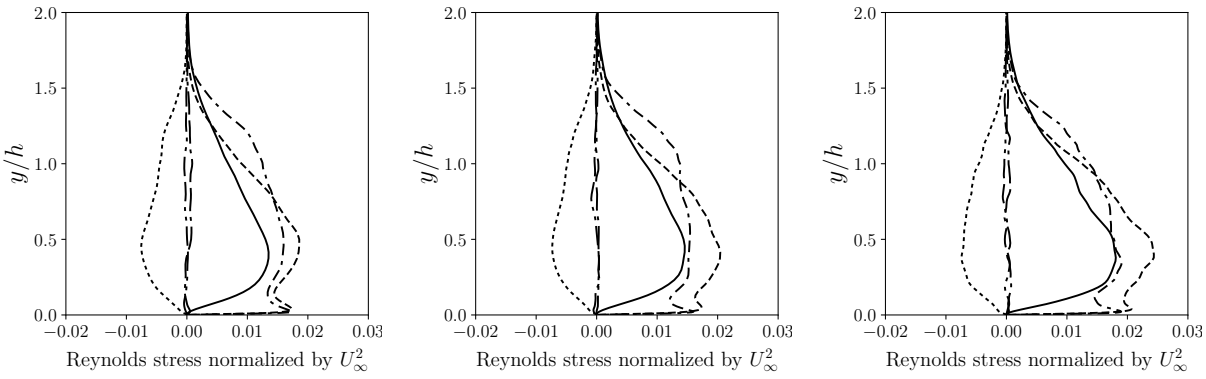

(a) $w = 3h$ (b) $w = 5h$ (c) $w = 7h$

Figure 4.8: Normalized Reynolds stresses vs. normalized wall-normal coordinate at $x = 5.5h$ in the center-plane ($z = 0$). – – - – -, $\overline{u'^2}$; ———, $\overline{v'^2}$; - - - - - -, $\overline{w'^2}$; ·····, $\overline{u'v'}$; — · —, $\overline{u'w'}$; — · · —, $\overline{v'w'}$.

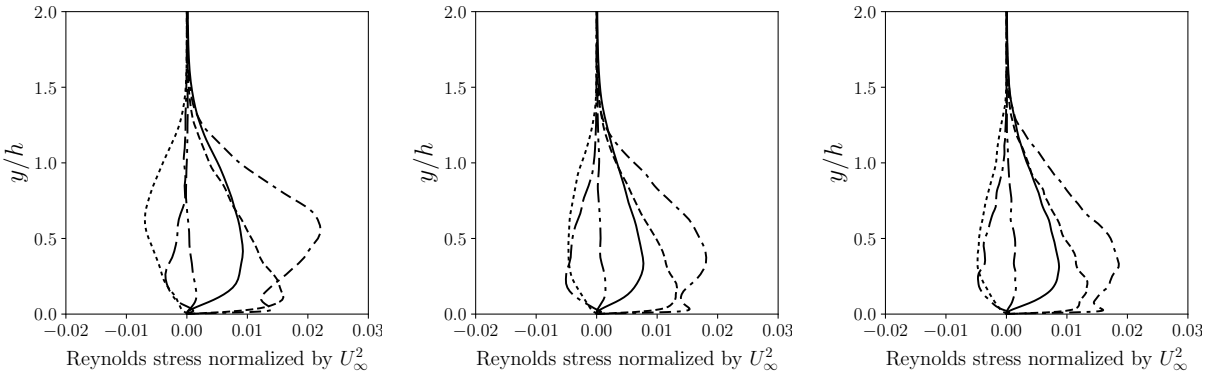

(a) $w = 3h$ (b) $w = 5h$ (c) $w = 7h$

Figure 4.9: Normalized Reynolds stresses vs. normalized wall-normal coordinate at $x = 5.5h$ and $z = h$. – – - – -, $\overline{u'^2}$; ———, $\overline{v'^2}$; - - - - - -, $\overline{w'^2}$; ·····, $\overline{u'v'}$; — · —, $\overline{u'w'}$; — · · —, $\overline{v'w'}$.

TBL. The span-wise turbulent transport of momentum is responsible for this increase in $\overline{w'}$. The $\overline{v'}$ component is also comparable to the $\overline{u'}$ due to the transport of turbulent momentum from the outer region to the near-wall region. This same phenomenon is responsible for the negative correlation between the $\overline{u'}$ and the $\overline{v'}$ components inside the TBL. We observe two peaks in the $\overline{u'}$ and $\overline{w'}$ profiles: the near wall peak due to the turbulent transport of momentum by the horse-shoe vortex, and the peak in the outer region caused by the TKE produced by the shear layer generated along the top surface of the cube. At $z = h$, the $\overline{u'w'}$ component has a magnitude comparable to the $\overline{u'v'}$ term, unlike that in the center-plane.

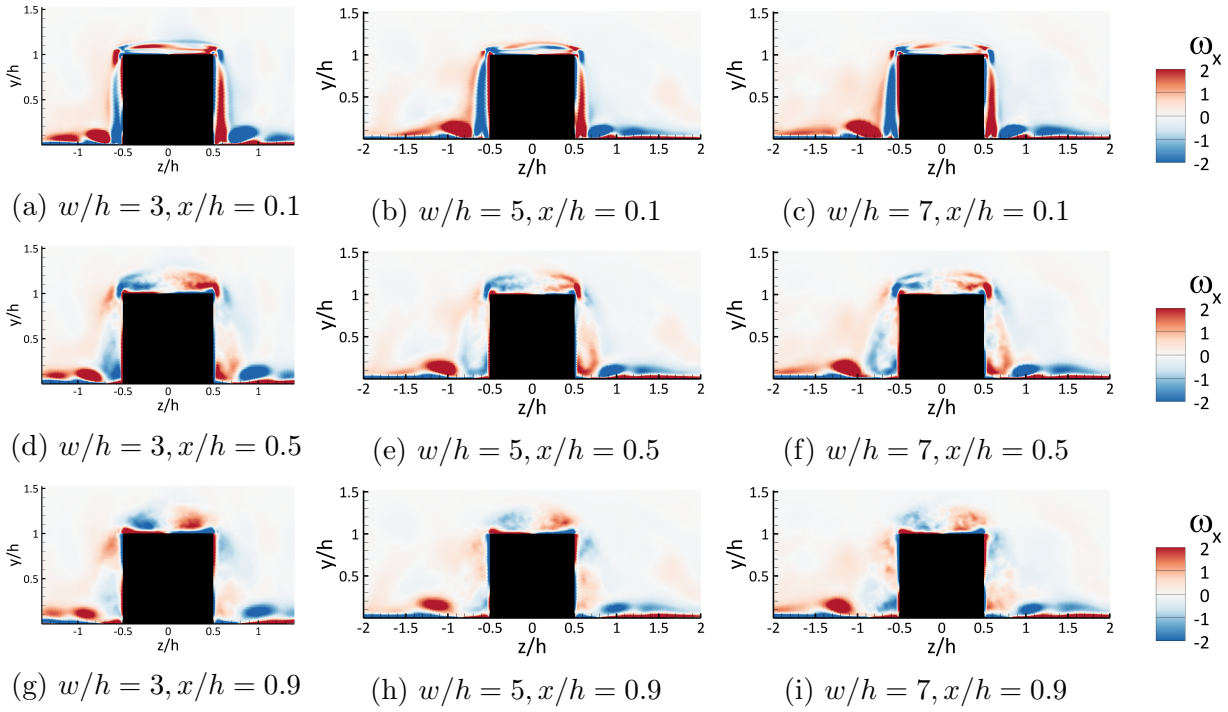

(a) $w/h = 3, x/h = 0.1$ (b) $w/h = 5, x/h = 0.1$ (c) $w/h = 7, x/h = 0.1$

(d) $w/h = 3, x/h = 0.5$ (e) $w/h = 5, x/h = 0.5$ (f) $w/h = 7, x/h = 0.5$

(g) $w/h = 3, x/h = 0.9$ (h) $w/h = 5, x/h = 0.9$ (i) $w/h = 7, x/h = 0.9$

Figure 4.10: Span-wise contours of streamwise component of the mean vorticity at $x/h = 0.1, 0.5$ and 0.9 along the cube, with the cube outlined in black.

This location lies inside the horse-shoe vortex which is characterized by the strong coupling between the $\overline{u'}$ and $\overline{w'}$ components. The magnitude and the variation of the $\overline{u'}$ component at $z = h$ for $w = 5h$ and $w = 7h$ is similar to that observed in the center-plane. However, for $w = 3h$ we observe an increase in the magnitude of $\overline{u'}$ in the outer region. The periodic arrangement of cubes with a span-wise spacing of $3h$ artificially imposes large-scale coherent structures in the outer region of the TBL. We believe this increase is a consequence of the amplification of these large scales in the outer region, as explained in Sec. 4.3.4.

4.3.3 Horse-shoe vortex

The horse-shoe vortex is a characteristic of flow past wall-mounted obstacles. We examine the extend to which the horse-shoe vortex spreads as w/h is varied in Fig. 4.10. Qualitatively, for the three inter-cube spacings, we observe a primary horse-shoe vortex formed closer to the cube, and a secondary horse-shoe vortex formed at a greater span-wise distance from the

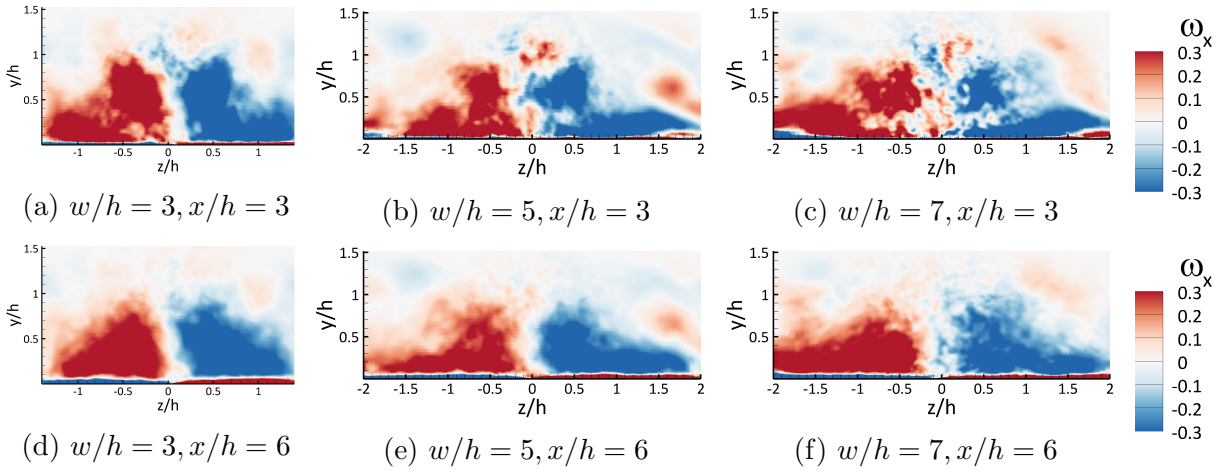

(a) $w/h = 3, x/h = 3$ (b) $w/h = 5, x/h = 3$ (c) $w/h = 7, x/h = 3$

(d) $w/h = 3, x/h = 6$ (e) $w/h = 5, x/h = 6$ (f) $w/h = 7, x/h = 6$

Figure 4.11: Span-wise contours of streamwise component of the mean vorticity at $x/h = 3$ and 5 in the wake of the cube.

cube. The strength of both of these horse-shoe vortices decreases with increasing stream-wise distance because of the diffusion of the vortex in the $y - z$ plane. Quantitatively, the span-wise positioning of the horse-shoe vortex is affected by the smaller inter-cube spacing in case of $w = 3h$. Both the primary and the secondary vortices are closer to cube in this case, with a stronger secondary vortex compared to the $w = 5h$ and $7h$ cases. We believe these differences are a result of the blockage created by the smaller inter-cube spacing driving the vortices closer to the cube.

In Fig. 4.11, we present the $x-$component of mean vorticity at $x = 3h$ and $6h$ in the wake of the cube. The strength of the horse-shoe vortex decreases with increasing stream-wise distance behind the cube. The decrease in strength can be attributed to vorticity diffusion in the $y - z$ plane which is evident from the increased spreading of the red and blue spots. The range of the color-bar in Fig. 4.11 is smaller than that in Fig. 4.10 by an order of magnitude. Along the surface of the bottom wall, a vortex sheet of opposite sign vorticity (compared to that of the horse-shoe vortex) develops. Given the sign of the vorticity, this vortex sheet is a consequence of the horse shoe vortex, and thus the cube, rather than turbulent boundary layer dynamics. As illustrated in Fig. 4.11, the right leg of horse-shoe vortex exhibits anti-clockwise rotation, whereas the right half of the vortex

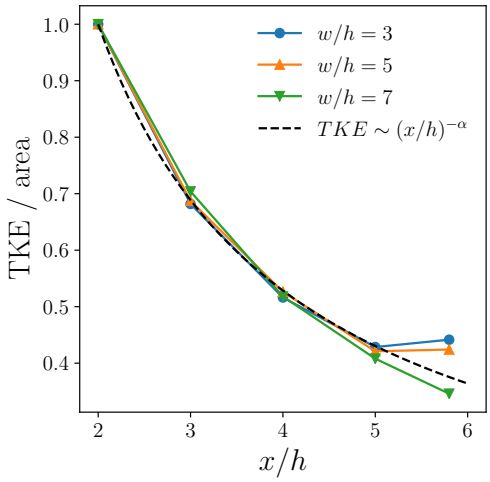

(a) Normalized TKE per unit area vs. normalized stream-wise distance. The dotted line corresponds to the power law behavior with $\alpha = 0.9$.

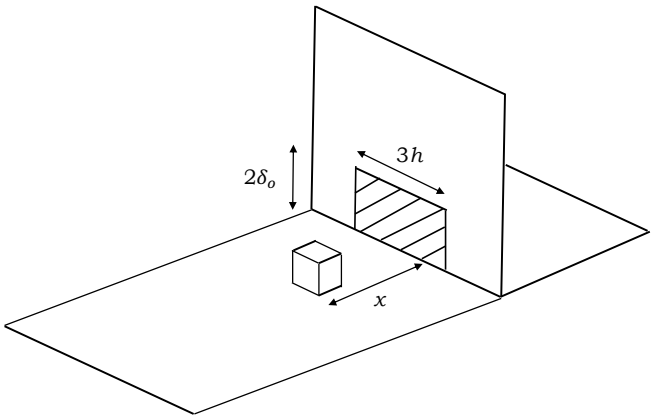

(b) Schematic showing the area over which TKE is averaged.

Figure 4.12: TKE area density as a function of the stream-wise distance for different inter-cube spacings.

sheet exhibits clockwise rotation. On account of the opposite rotation directions, the fluid in between the horse-shoe vortex and the vortex sheet experiences a net force in the span-wise direction away from the center-plane. Furthermore, the anti-clockwise rotation of the right leg of the horse-shoe vortex corresponding to the cube under consideration, and the clock-wise rotation of the left leg of the horse-shoe vortex corresponding to the cube on the right, results in a net force acting on the fluid in between the two vortices in the positive $y-$direction, which explains the ejection process observed in Sec. 4.3.2. In the wake of the cube, the span-wise spreading of the horse-shoe vortex depends on the inter-cube spacing as the horse-shoe vortex is more concentrated for $w = 3h$ than for larger spacings.

4.3.4 Turbulent kinetic energy

The analysis of the turbulent kinetic energy (TKE) per unit area in the wake of a single cube with slip walls imposed on the span-wise boundary demonstrated a power law decay with an increasing stream-wise coordinate, and a power law exponent (α) increasing with increasing h/δ in a non-linear fashion (Sec. 3.3.5). In case of multiple cubes with varying

inter-cube spacing, the TKE per unit area in the wake of the cubes in presented in Fig. 4.12a. TKE is averaged over the shaded region depicted in Fig. 4.12b at different stream-wise locations. The shaded area symmetrically spans a distance of $3h$ in the $z-$direction, and $2\delta_o$ in the wall-normal direction, where δ_o is the turbulent boundary layer thickness at the front face of the cube. The span-wise width of the smallest domain is $3h$, hence the choice for the width of the shaded area in the span-wise direction. The area extends up to $2\delta_o$ in $y-$direction to capture the TKE production inside the shear layer emanating from the top surface of the cube. We observe that the decay of TKE/area obeys the same power law behavior up to $x = 5h$ for the three cases, with the power law exponent $\alpha = 0.9$, as given below,

$$\frac{TKE^*}{area} = \left(\frac{x}{h}\right)^{-0.9} \tag{4.2}$$

where the "$*$" denotes that TKE/area is normalized by its value at $x = 2h$. We conclude that TKE/area is independent of the inter-cube spacing (w/h) for constant h/δ up to a stream-wise distance of $5h$ behind the cube. Qualitatively, the rate of decay of TKE/area is a measure of the departure from the state of equilibrium of the TBL, which in turn is governed by the TKE produced by the cube. Furthermore, TKE production depends on the TBL properties and the height at which the cube intersects the TBL (Sec. 3.3.5). Because the TBL properties and the h/δ ratio are same in all the cases, we expect the three curves in Fig. 4.12a to collapse on top of each other. The observation that $\alpha < 1$ implies that this decay in the turbulent kinetic energy is a near-wake phenomenon, because integration of Eq. 4.2 in x from zero to infinity would diverge. The TKE area density should be constant with respect to x/h as the TBL recovers and reaches equilibrium. Toward the end of the domain at $x = 5.8h$, the TKE/area increases for the $w = 5h$ and $w = 3h$ cases because of interaction between vortices from adjacent cubes.

To understand the distribution of TKE, we examine the absolute value of the production (P_k) to dissipation (ϵ_k) ratio in the $y-z$ plane in Fig. 4.13. At stream-wise location $x = 0.5h$

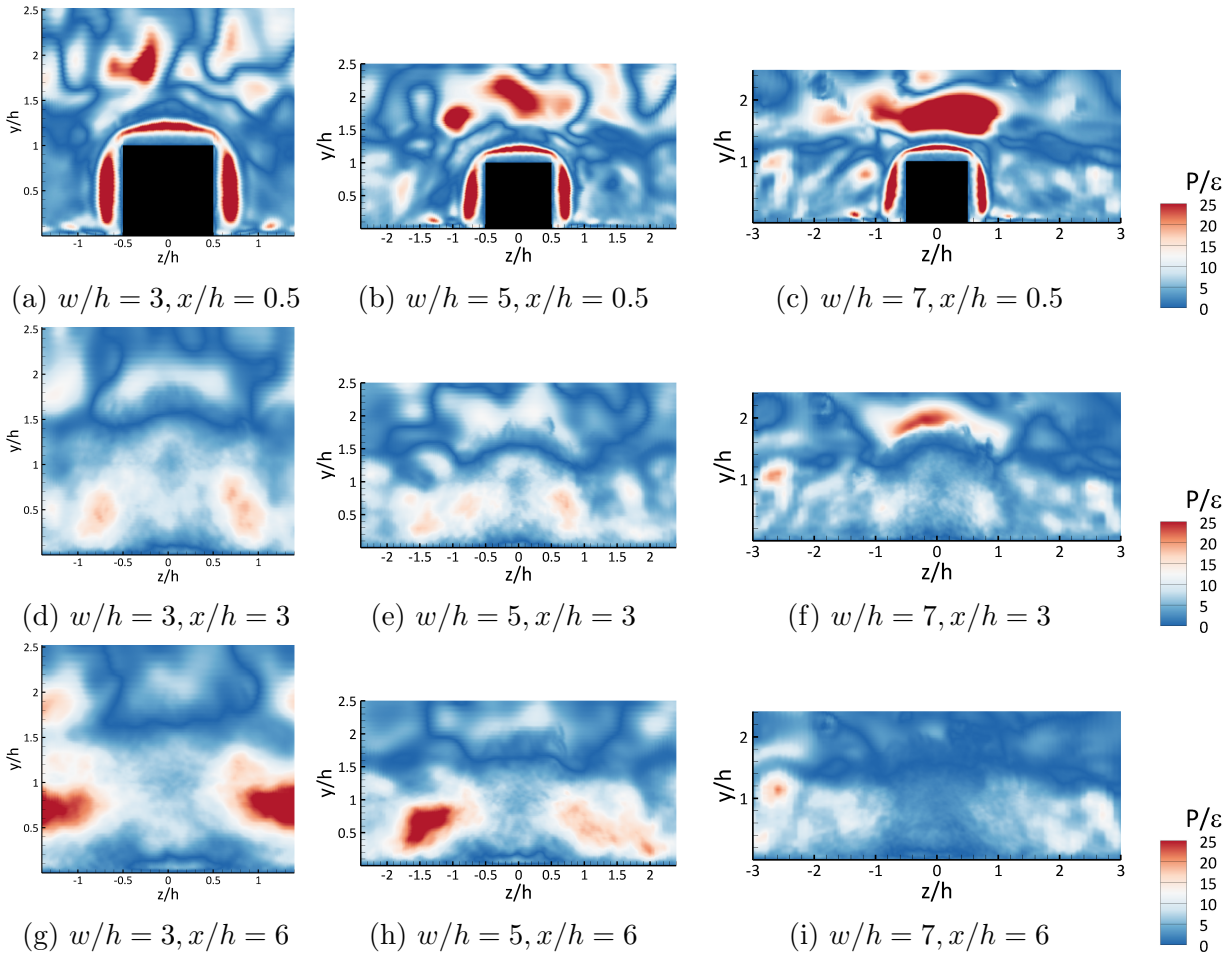

(a) $w/h = 3, x/h = 0.5$ (b) $w/h = 5, x/h = 0.5$ (c) $w/h = 7, x/h = 0.5$

(d) $w/h = 3, x/h = 3$ (e) $w/h = 5, x/h = 3$ (f) $w/h = 7, x/h = 3$

(g) $w/h = 3, x/h = 6$ (h) $w/h = 5, x/h = 6$ (i) $w/h = 7, x/h = 6$

Figure 4.13: Absolute value of TKE production to dissipation ratio contours in the $y - z$ plane at $x/h = 0.5, 3$ and 6, with the cube outlined in black.

(half-way along the cube), we observe large values of P_k/ϵ_k around the cube. The dominant contribution to production term around the cube is expected due to the large gradients in velocity along the surface on account of the no-slip boundary condition. The large patch of high P_k/ϵ_k at a height $y \approx 2h$ over the cube is a numerical artifact of dividing small value of P_k by an order of magnitude smaller value of ϵ_k, as was observed in case of the single cube (Sec. 3.3.5). The reason is P_k depends on the gradient of velocity, whereas ϵ_k depends on the gradient in velocity fluctuations, which decay much faster in the outer region than the outer scale velocity. Further downstream at a stream-wise location of $x = 3h$, the magnitude of P_k/ϵ_k has decreased on account of dissipation and diffusion of the TKE. At $x = 6h$, however, we observe an increase in P_k/ϵ_k. These peaks are separated by a span-wise

distance of approximately $3h$ and originate as a result of the amplification of large scale structures, artificially imposed by a periodic span-wise arrangement of the cubes.

A growth analysis of optimal linear modes using the Orr-Sommerfeld-Squire equations for the mean turbulent profile [125] suggests that the largest transient growth is observed for large-scale global structures with a span-wise spacing of approximately $3h$. This claim was verified numerically by Hwang *et al.* [126]. In case of our simulations with $w = 3h$, we are artificially imposing large-scale structures with a span-wise separation of $3h$. We believe that these coherent structures undergo amplification as we move along the stream-wise direction, in a manner similar to that observe by Pujals *et al.* [8] with a periodic arrangement of span-wise wall-mounted cylinders. For $w = 3h$, the observation station at $x = 6h$ is located at a distance of $2w$ behind the periodic array of cubes, which is long enough for the onset of amplification of the imposed coherent streaks [8]. This amplification of the dominant mode results in an increased value of P_k/ϵ_k. In case of $w = 5h$ and $7h$, imposed modes have a period of $5h$ and $7h$ respectively, so the domain is not long enough for the coherent structures to interact with each other. Nevertheless, we do observe similar peaks for the $w = 5h$ case, which could be a precursor to the amplification of coherent streaks, spreading further in the span-wise direction as we move downstream.

To understand the physics behind the distribution of TKE in the wake of the cube, we examine the TKE budget,

$$\begin{aligned}\frac{\partial(\frac{1}{2}q^2)}{\partial t} = &\underbrace{-\frac{1}{2}U_k\overline{(u_l'u_l')_{,k}}}_{C_k}\underbrace{-\overline{(u_l'u_k')}U_{l,k}}_{P_k}\underbrace{-\frac{1}{2}\overline{(u_l'u_l'u_k')_{,k}}}_{T_k}\\ &\underbrace{+\frac{1}{2}\left(\frac{1}{Re}+\nu_\tau\right)\overline{(u_l'u_l')}_{,kk}}_{D_k}\underbrace{-\left(\frac{1}{Re}+\nu_\tau\right)\overline{u_{l,k}'u_{l,k}'}}_{\epsilon_k}\underbrace{-\overline{u_l'p_{,l}'}}_{\Pi_k},\end{aligned} \tag{4.3}$$

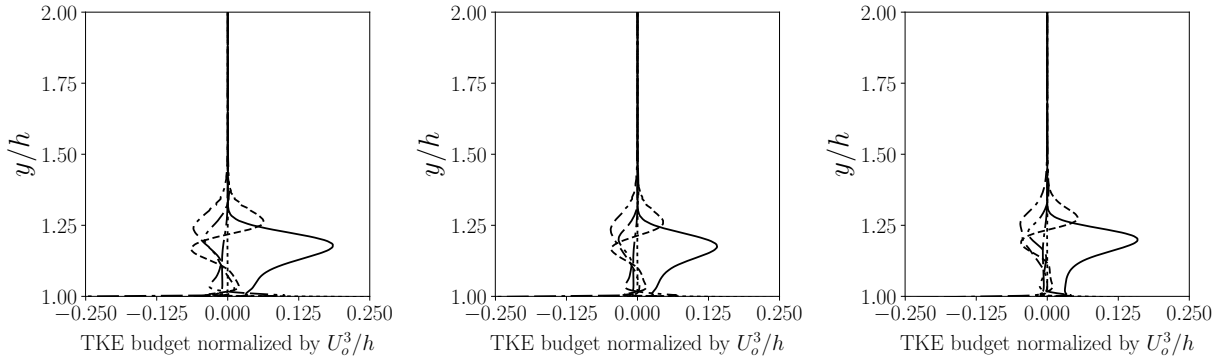

(a) $w = 3h$ (b) $w = 5h$ (c) $w = 7h$

Figure 4.14: Span-wise averaged TKE budget normalized using outer coordinates at $x = 0.5h$: – – – –, convection; ———, production; ------, turbulence transport; ---------, viscous diffusion; — · —, viscous dissipation; — · · —, velocity-pressure gradient.

where

$$\frac{1}{2}q^2 = \frac{1}{2}(\overline{u'^2} + \overline{v'^2} + \overline{w'^2}) \tag{4.4}$$

$\frac{1}{2}q^2$ is the turbulent kinetic energy, $Re = \frac{U_m \delta}{\nu}$ is the Reynolds number based on mean velocity (U_m) and boundary layer thickness (δ), ν_τ is the eddy viscosity given by the LES model, and the over-bar represents a time average. The terms on the right hand side of Eq. 4.3 are: convection (C_k), production (P_k), turbulence transport (T_k), viscous diffusion (D_k), viscous dissipation (ϵ_k) and velocity-pressure gradient (Π_k).

We examine the variation in the contribution of each of the terms in Eq. 4.2 at different stream-wise locations. Fig. 4.14 shows the TKE budget on the top surface of the cube at $x = 0.5h$. The profiles are averaged in the span-wise direction and in time, and normalized by the outer coordinates (free-stream velocity U_o and cube height h). We observe a large spike in the production term (P_k) at a wall-normal distance of $y = 1.2h$, which is a consequence of the turbulent shear layer emanating from the top surface of the cube. The large velocity gradients inside the shear layer are responsible for the production of TKE. The magnitude of P_k is identical in the three cases because at $x = 0.5h$ the coherent structures produced on the top of the cube scale with the cube height itself, and the length scales associated

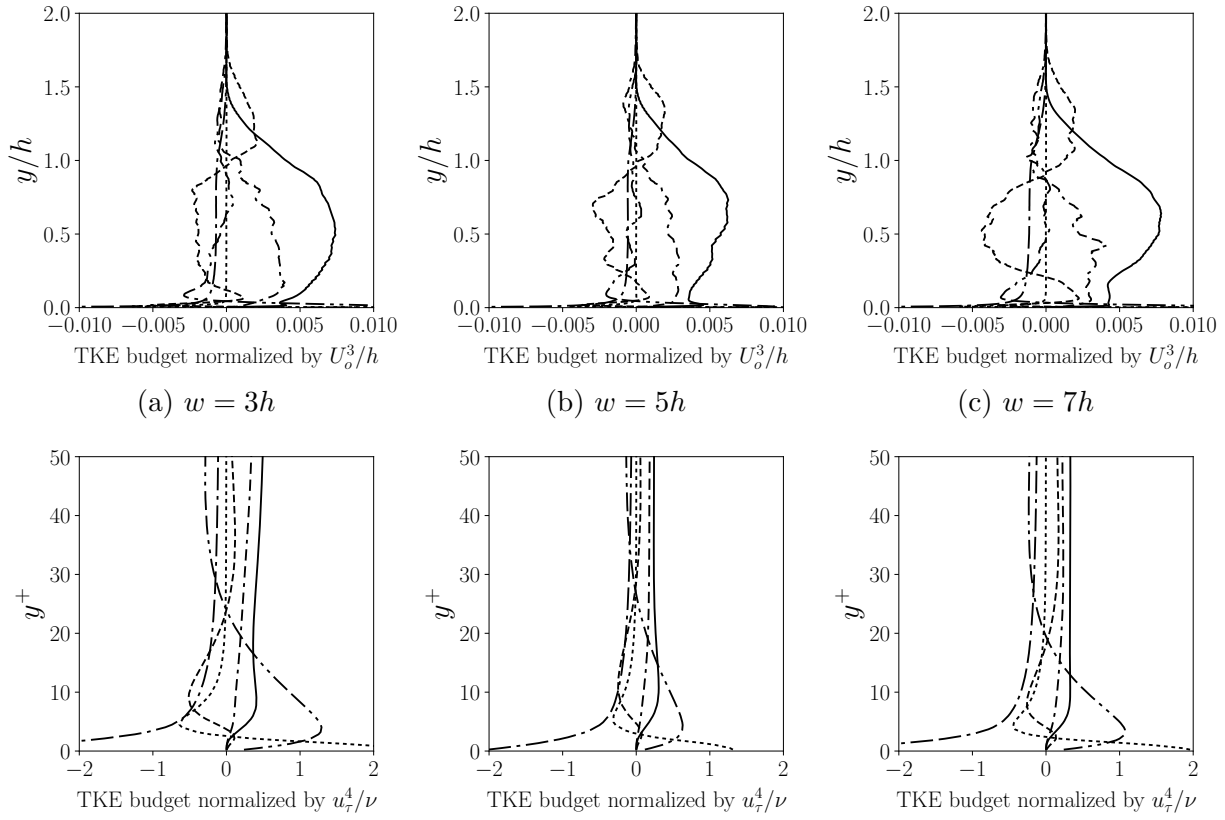

(a) $w = 3h$ (b) $w = 5h$ (c) $w = 7h$

(d) $w = 3h$ (e) $w = 5h$ (f) $w = 7h$

Figure 4.15: Span-wise averaged TKE budget normalized using inner and outer coordinates at $x = 3h$: – – – –, convection; ———, production; ------, turbulence transport; ·····, viscous diffusion; —·—, viscous dissipation; —··—, velocity-pressure gradient.

with the spacing between adjacent cubes is not relevant. The negative peak in the transport term (T_k) corresponds to the positive peak in P_k in terms of its wall-normal distance. T_k is positive in both directions moving away from the center of the shear layer, which implies that TKE is transported from the shear layer to the low speed and high speed sides of the shear layer.

As we move along the stream-wise direction at $x = 3h$, the spacing (w) begins to affect the TKE budget, as illustrated in Fig. 4.15. In the outer region at $y \approx 0.8h$ we observe a peak in the P_k profile, which corresponds to the shear layer production of TKE. For the $w = 5h$ and $w = 7h$ cases, the value of P_k decreases with decreasing y-coordinate, however, there exists another peak close to the wall. This near wall peak is a result of the strong

velocity gradients in the wall-normal direction at that height. For the case with the smallest inter-cube spacing ($w = 3h$), the P_k profile does not exhibit an inflection point at $y \approx 0.2h$, observed in the other two cases. This higher P_k value is a consequence of two effects: (i) large production of TKE at the center of the horse-shoe vortex, and (ii) a major portion of the domain width being occupied by the horse-shoe vortex, unlike the other two cases. The transport term behaves in a similar fashion as observed at $x = 0.5h$, transporting TKE from the shear layer to the near-wall region and the region away from the wall. The convection term (C_k) is positive inside the boundary layer, because the TKE values are highest inside the boundary layer, and TKE produced by the cube is convected by the mean flow in the stream-wise direction. In the inner region of the TBL, the TKE budget terms show similar variation in the wall-normal direction. We know that viscosity dominates in the inner region, which is illustrated by the large magnitudes of the viscous diffusion (D_k) and viscous dissipation terms (ϵ_k). In the outer region $P_k > \epsilon_k$, whereas, in the inner region the situation is reversed. This informs us that at $x = 3h$ the TBL is in a state of non-equilibrium. A turbulent flow is said to in equilibrium when the production of TKE is balanced by its dissipation.

Toward the end of the domain in the stream-wise direction, at $x = 6h$, the vortices from adjacent cubes are interacting strongly for the $w = 3h$ and $w = 5h$ cases, and its effects on the TKE budget are depicted in Fig. 4.16. The P_k peak in the outer region is still noticeable but is smaller than its value at $x = 3h$. This decrease is due to the transport, diffusion and dissipation of TKE from the shear layer and the center of the horse-shoe vortex, as we move along the stream-wise direction. However, the most interesting observation is the large increase in the convection (C_k) of TKE in the outer region. We suspect this increase is due to the amplification of large-scale, coherent structures in the outer region of the TBL, as explained in Sec. 4.3.3. An obvious question arises: why does this increase in TKE appear in C_k, as opposed to an increase in the transport (T_k) term similar to the shear layer? The transport term is a third-order correlation in the velocity fluctuations, whereas C_k is defined directly in terms of the outer scale velocity (U). If the dominant mode is amplified as

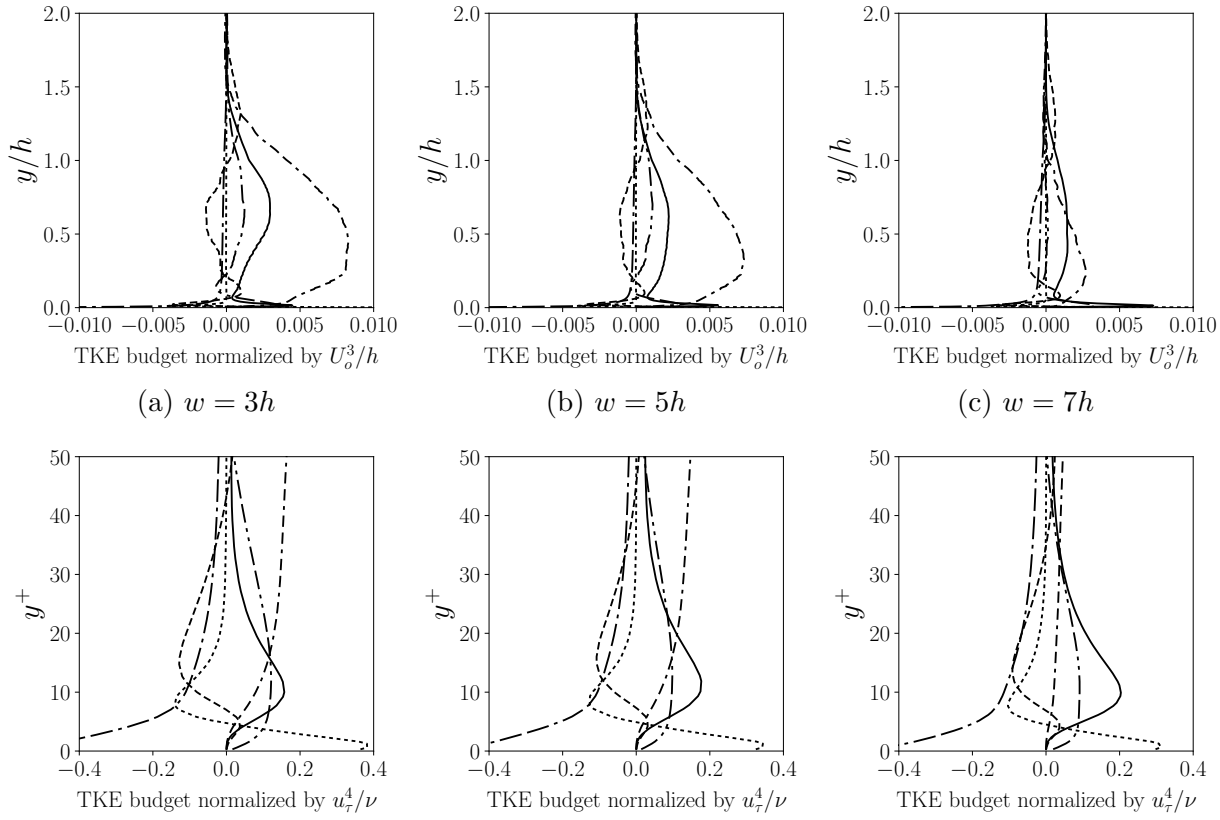

(a) $w = 3h$ (b) $w = 5h$ (c) $w = 7h$

(d) $w = 3h$ (e) $w = 5h$ (f) $w = 7h$

Figure 4.16: Span-wise averaged TKE budget normalized using inner and outer coordinates at $x = 6h$: – – – –, convection; ———, production; ------, turbulence transport; ·····, viscous diffusion; — · —, viscous dissipation; — · · —, velocity-pressure gradient.

suggested it would as an outer scale phenomenon naturally convect TKE in the stream-wise direction, resulting in an increased C_k. The P_k term is not balanced by the ϵ_k term in the outer region implying non-equilibrium. The magnitude of C_k is larger in the inner region than that observed in an equilibrium flat plate TBL [118], thus suggesting, the TBL is still in a state of non-equilibrium at $x = 6h$.

4.4 Conclusions

A high-fidelity LES of flow over a single row of equally spaced, wall-mounted cubes placed in SETBL is performed at a Reynolds number of 19,600, based on the mean velocity and the cube height (h). The cube height is set equal to the boundary layer thickness at its front

face. We investigate the impact of the inter-cube spacing ($w = 3h, 5h$, and $7h$) on the fluid dynamics by varying the domain width, whose boundaries are prescribed as periodic.

The variation of the skin friction coefficient along the bottom-wall of the domain reveals that the flow separates at a distance of $1.3h$ in front of the cube, and reattaches at a distance of $1.6h$ behind the cube, consistent with those obtained for a single cube in a SETBL. This observation implies the separation and reattachment lengths are independent of the inter-cube spacing for the values considered in this study. On the other hand, the span-wise location of the horse-shoe vortex is affected by the inter-cube spacing (w). In the near-wake of the cube the horse-shoe vortex is more concentrated for $w = 3h$, as compared to the other two cases because of the blockage created by the smaller inter-cube spacing driving the vortices closer. The center of the horse-shoe vortex exhibits a strong correlation between the $\overline{u'}$ and $\overline{w'}$ components of velocity fluctuations on account of span-wise transport of turbulent momentum. For all the cases, TKE/area decrease in a power law manner up to a stream-wise distance of $5h$, with a power law exponent $\alpha = 0.9$ implying that α is independent of the inter-cube spacing, and is only a function of the h/δ amongst the parameters considered in our work.

An important observation is the periodic increase in TKE production, and an increase in TKE convection in between adjacent cubes in the outer region of the TBL at a stream-wise distance of $5h$ in the wake of the cube with $w = 3h$. This observation suggests an amplification of large-scale, coherent structures, similar to the findings of Pujals *et al.* [8] for flow over a single row of wall-mounted cylinders. We believe the ejection of low momentum fluid to the outer region in between horse-shoe vortices from adjacent cubes is responsible for this amplification.

CHAPTER V

Conclusions and future work

5.1 Summary and key findings

The objective of this work is to understand the basic physics of flow over a wall-mounted cube placed in a spatially evolving turbulent boundary layer (SETBL) using high-fidelity Large Eddy Simulations (LES). We investigated (i) the fundamental physics of flow over a cube in a SETBL, (ii) the effect of cube height (h) to boundary layer thickness (δ) ratio on the near-wake characteristics like, separation and reattachment lengths, spreading of the horse-shoe vortex, and turbulent kinetic energy (TKE) distribution, and (iii) the effect of spacing between adjacent cubes when a single row of cubes is placed normal to the flow direction on the aforementioned parameters. The understanding achieved through this basic physics study will enable the development of improved strategies for flow control using passive vortex generators in a variety of applications, such as reducing pressure drag on road vehicles, improving efficiency of turbo-machinery, etc. The keys findings are:

1. The major part of our initial effort was dedicated to developing the tools necessary to conduct high-fidelity numerical simulations of flow over a wall-mounted cube in a SETBL. A physics-based approach was implemented to prescribe a time-varying inflow boundary condition for the velocity field, which is necessary to simulate a SETBL. The implementation revealed that for a Reynolds number of 19,600 based on the mean

velocity and inlet boundary layer thickness. The flow requires a transition length of $x \approx 12\delta_o$ to recover the boundary layer thickness and develop into a realistic TBL. Furthermore, we propose a novel approach to prescribe a synthetic inflow boundary condition for LES of a SETBL based on kernel density estimation machine-learning (ML) technique. However, this proposed method gives poor results in its current form because the three dimensional time and space correlations between the turbulent structures are neglected. A modified ML approach is proposed to address this drawback, whereby the ML is performed in the Fourier domain as opposed to the physical domain.

2. We validated the LES solver of the open-source software OpenFOAM against experiments of flow over a cube in a fully developed turbulent channel flow. We use this framework to first study the basic fluid mechanics, and later to understand the effect of cube height to boundary layer thickness (h/δ) ratio on the near-wake characteristics for a single cube placed in a SETBL at a Reynolds number (Re_δ) of 19,600. Re_δ is based on the mean velocity and the boundary layer thickness at the front face of the cube and is constant across the three h/δ cases considered in this work. At the center of the horse-shoe vortex in the wake we observe a greater mean stream-wise velocity than the center-plane, and a strong coupling between the $\overline{u'}$ and $\overline{w'}$ components of velocity fluctuations. The span-wise gradient of mean stream-wise velocity and the strong coupling is responsible for higher turbulent kinetic energy (TKE) production at the center of the vortex for all h/δ ratios. The separation length in front of the cube and the reattachment length behind the cube scale with h with values of $1.3h$ and $1.6h$ respectively. The span-wise spreading of the horse-shoe vortex exhibits a slight dependence on h/δ, with a greater spreading rate for smaller h/δ on account of a weaker span-wise pressure gradient. The counter-rotating vortex pair generated by the cube in its wake diffuses in the stream-wise direction. An important finding is the discovery of a power law decay of TKE per unit area in the near-wake of the cube, and the non-linear dependence of the power law exponent on the h/δ ratio. The TKE

production in the wake scales with the cube height and is a measure of the deviation from the state of equilibrium of the TBL. The power law exponent of the decay rate increases with increasing h/δ which implies that more significant departure from the state of equilibrium results in a more drastic decay of TKE area density. If we consider the average TKE over the entire width of the domain in the near-wake of the cube, then the only significant terms from the TKE budget are the production (P_k) and the dissipation (ϵ_k) terms. Our results potentially imply that both of these terms also decay in a power law manner in the near-wake, in agreement with the findings of Hussein *et al.* [11].

3. The investigation of flow over a single row of wall-mounted cubes extending in the span-wise direction, with their front-face normal to the flow direction is carried out at the same Re_δ of 19,600, with $h/\delta = 1$. Three different inter-cube spacings (w) are considered with $w = 3h, 5h$ and $7h$. We observed the same separation (X_s) and reattachment (X_r) lengths for the three cases ($X_s = 1.3h$ and $X_r = 1.6h$) which are identical to those observed for the single cube case. This finding also implies that X_s and X_r scale with the cube height (h) and are independent of the inter-cube spacing up to $w = 3h$. However, the span-wise spreading of the horse-shoe vortex is influenced by the inter-cube spacing. The vorticity field is more concentrated in the wake of more closely spaced cubes, and interactions between horse-shoe vortices from adjacent cubes are more prominent. These interactions result in a strong coupling between the $\overline{u'}$ and $\overline{v'}$ components of velocity fluctuations in the region in between the cubes. The TKE area density obeys the same power law decay with $(x/h)^{-0.9}$, up to five cube heights downstream as observed for the single cube case with $h/\delta = 1.0$. Beyond five cube heights downstream for the $w = 3h$ and $w = 5h$ cases, the TKE per unit area increases on account of the interaction between the horse-shoe vortices from adjacent cubes. The periodic arrangement of cubes in the span-wise direction artificially imposes large scale structures in the outer region of the TBL. The large-scale coherent structures spaced

$3h$ apart get amplified after approximately five cube heights downstream in the wake region. We hypothesize, the ejection of low momentum fluid from the near wall region to the outer region in between horse-shoe vortices from adjacent cubes is responsible for the amplification. This amplification results in an increasing TKE production to dissipation ratio in the region in between two cubes and in an increasing convection of TKE in the outer region of the TBL six cube heights downstream. We find that the stream-wise length of the domain is insufficient to capture the entire amplification process and far-wake properties.

5.2 Suggestions for future work

The flow over a wall-mounted cube is an active research area, and our present work naturally lends itself to be extended in a number of directions. In this section, we discuss the design implications of our physics-based findings in reducing pressure drag on automobiles. We also discuss potential improvements to the numerical framework using machine learning, future studies investigating the effect of other parameters and physical phenomenon for flow over a single cube, and an array of cubes placed in a TBL.

5.2.1 Reducing pressure drag on road vehicles using a single row of cubes

Pujals *et al.* [8] experimentally showed that a single row of wall-mounted cylinders can be used to reduce pressure drag on an Ahmed body by nearly 10%. Similarly, if we plan to use a single row of wall-mounted cubes for the same purpose, there are three important questions: (i) how should one choose the height (h) of the cubes as compared to the boundary layer thickness (δ), (ii) how should one choose the spacing between adjacent cubes (w)?, and (iii) how should one choose the distance of the row of cubes from the rear edge of the car model (x)? Based on our physics-based discoveries we can make well-informed estimates for these lengths.

We believe that $0.6\delta < h < \delta$, and this estimate is drawn from our findings from the single

cube and row of cubes studies. From the single cube study we know that the production (P_k) of turbulent kinetic energy (TKE) increases with increase in h with the caveat that as h increases the form-drag associated with the cube also increases. The magnitude of P_k depends on the gradient of velocity, and the velocity gradient is highest at the surface of the cube. The maximum value of the velocity gradient can be achieved when $h = \delta$, beyond which the velocity gradient remains the same, however, the form-drag increases. From the LES of flow over a row of cubes we discovered that an amplification of the large scale structures is observed in the outer region of the TBL. To leverage the increase in TKE due to the amplification in reducing pressure drag the cube should lie in the outer region of the TBL, i.e., $h \geqslant 0.2\delta$. From the production of TKE and amplification considerations we believe $0.6\delta < h < \delta$.

The investigation of flow over a row cubes revealed that the amplification of TKE occurs for an inter-cube spacing (w) approximately between $3h$ and $5h$. Therefore, we believe $w \approx 3h$ to $5h$ should be the spacing between adjacent cubes when using a row of cubes. Finally, though we did not explicitly calculate the distance (x) of the row of cubes from the rear edge of the car, we believe $x \approx 5w$, where w is the inter-cube spacing. For a row of cylinders placed inside a TBL on a flat plate Pujals *et al.* [53] observed that the amplification of periodic streaks reaches maximum value at a distance of $5w$ behind the row. If the amplification of large scale outer structures observed in case of row of cubes in the present work is similar to that observed in case of the row of cylinders, then the row of cubes should be placed at $x \approx 5w$. The estimates for h, w and x need to be verified by studying the effect of the row of cubes on the separated region on a car model.

5.2.2 Improving the numerical framework and models

The machine-learning based approach we proposed did not yield accurate results because the spatial and temporal correlations between the coherent turbulent structures are completely neglected. If we transform the training data from the physical space to the

wave-number space and then apply machine-learning, we expect the performance to improve significantly. The proposed method has the potential to reduce the transition length required for the flow to develop into a realistic TBL, as well as reduce the computation time without any significant modification to the flow solver.

Prior research [55, 56] demonstrates the inability of the Reynolds Averaged Navier-Stokes (RANS) approach in accurately simulating flow over a wall-mounted cube in a TBL. The failure of RANS models is attributed to their inability to capture the unsteady effects in front of the cube and the near-wake region, large-scale eddy structures that dominate the turbulent transport, vortex shedding, and bi-modal fluctuation frequencies reported in front of the cube [55]. In order to address the inability in capturing the unsteady flow features, researchers have turned to the Unsteady RANS (URANS) approach, which provides a significant improvement in predicting mean flow quantities on top and in the wake of the cube [56]. However, even with the state-of-the-art implementation of the RNG $k-\epsilon$ URANS model, we observe poor prediction of the reattachment length on the top surface and in the wake of the cube [127]. From the URANS study of flow over a building in a TBL by Tominaga [127] we observe that the lack of clear spectral separation between the periodic motions and turbulent fluctuations may prevent URANS models from being successfully implemented for such flows. On a more fundamental level, the physical processes that govern the mathematical dependence of the Reynolds stress tensor on the turbulent transport by large-scale structures and superpositioning of multiple shedding frequencies are unknown, it may be possible that a closed form equation that captures this dependence may not even exists. One may be able to leverage machine-learning to address this problem. Singh *et al.* [128] used a neural-network-augmented Spalart-Allmaras model to improve RANS predictions of separated flow over an airfoil. Flow over a single wall-mounted cube and an array of cubes provides an ideal test case to apply ML augmented RANS/URANS models to improve mean flow predictions.

Investigation of fundamental physics of flow over a cube in a TBL at high or very-

high Reynolds numbers using wall-resolved LES or DNS is still beyond our scope. There are two possible approaches to realize these studies: $p-$refinement and $h-$refinement. In $p-$refinement we increase the number of degrees of freedom per computational cell, which in the context of Galerkin-type methods would imply using a higher order polynomial to interpolate the solution inside a cell. A potential study could develop a numerical framework based on a Galerkin-type approach to arbitrarily increase the order of accuracy of the framework. This will enable us to achieve the same order of accuracy as existing 2^{nd} order approaches using fewer grid points, or achieve the same order of accuracy using the same number of grid points for higher Reynolds number flow configurations. On the other hand, in $h-$refinement we increase the number of grid points in the computation to either resolve smaller length scales or increase the order of accuracy. Exa-scale computing will enable us to perform such massive simulations, and the scientific community needs to address multiple issues in order to realize this objective. We need to build robust computer architectures, smart compilers, develop fault tolerant and efficient CFD codes, consider power consumption requirements while developing our codes, etc., all of which are possible research avenues.

5.2.3 Investigating fundamental physics

An important accomplishment in the present work is the discovery of the power law decay of the turbulent kinetic energy (TKE) per unit area in the near-wake of the cube, and the non-linear dependence of the power law exponent on the cube height to boundary layer thickness ratio (h/δ). An immediate next step could be investigating the reason for this power law decay rate. Efforts can be focussed on examining whether the power law decay represents a non-linear process governed by a differential equation observed in other flow configurations or physical systems.

We know that the h/δ ratio affects the wake characteristics for a single cube placed in a TBL. A recent experimental study by Hearst *et al.* [119] demonstrates that the level of free-stream turbulence (FST) (separate from the shear) also affects the wake characteristics for a

constant h/δ. They identify that FST (u'_h/U_h) and normalized shear ($\widehat{\tau} = (h/U_h)(\partial U/\partial y)|_h$) contain information about the major aspects of flow at the cube height, including the turbulence intensity, the mean velocity, the shear, and the characteristic dimensions. They investigate the effect of varying the FST on the wake characteristics and TBL recovery. A potential study could investigate the effects of FST and normalized shear ($\widehat{\tau}$), individually, on the decay rate of TKE area density in the near-wake. Castro *et al.* [108] found that there are no discernible effects of Reynolds number on the mean flow properties if $Re_h > 4000$, however the effect of Re_h on the TKE area density decay rate is not known, which could be a potential research problem. The power law decay of the average TKE in the near-wake of wall-mounted obstacles is a novel finding, and it would be interesting to examine if the same decay rate applies to obstacles of other shapes like cylinders, bumps, rollers, etc. Another possible extension of the present work is studying the local heat transfer from a cube placed in a TBL. Investigating the convective heat transfer dependence of factors like h/δ, Reynolds number, FST, etc., has been an active research topic for decades with applications in designing of circuit boards, and understanding heat transfer from a building [107, 129].

Our work examined the TBL flow over a single row of cubes placed adjacent to each other in the span-wise direction, with their front-face normal to the flow direction. Varying the inter-cube spacing (w) revealed, large scale coherent structures get amplified in the outer region of the TBL for the $w = 3h$ case. However, the effects are visible only after a stream-wise distance of $2w$ behind the cube. The domain length was found to be insufficient to analyze the entire amplification process. An obvious next step could be to study the same problem in a longer domain to capture the amplification and a subsequent decay to the amplification factor with increasing stream-wise distance. It would be helpful to employ a modal decomposition method like Proper Orthogonal Decomposition (POD), Dynamic Mode Decomposition (DMD), or Koopman Operator to investigate the span-wise periodic amplification of the larges-scale structures.

Pujals *et al.* [53] observed a similar amplification of artificially imposed large-scale struc-

tures by a single row of wall-mounted cylinders. They leveraged the higher TKE of the large scale structures to reduce flow separation on the rear end of an Ahmed body[1]. Similarly, an array of span-wise wall-mounted cubes arranged in a single row can be used to reduce flow separation by imposing large scale coherent structures. A potential test case could be flow separation control on an Ahmed body, a backward-facing step or a backward-facing ramp [115, 130].

The single row of cubes can be extended in the stream-wise direction to form a three dimensional array of cubes. If the cube height $h \leqslant 0.1\delta$, the flow configuration can represent flow over a rough-wall in TBL [75, 73, 131]. A matrix of cubes with height $0.1\delta \leqslant h \leqslant 0.5\delta$ placed in a turbulent channel flow has been used to study the local convective heat transfer. Investigating this flow configuration has applications in the efficient designing of circuit boards [106, 132, 133]. On the other hand, cubes of the same height placed inside a TBL mimics the atmospheric boundary layer flow over vegetative canopies and urban landscape [65, 66, 67, 69]. All of the above mentioned flow configurations are active research areas in terms of analyzing the flow physics, developing modeling techniques, improving high-performance computing architectures to perform DNS of more complex flows, etc. The ideas and the tools developed in the present study can be applicable in investigating the aforementioned problems.

[1]Ahmed body is a simplified car model, first proposed by Ahmed *et al.* [49]

APPENDICES

APPENDIX A

Validation of our implementation of the conventional synthetic inflow method

A.1 Introduction

Our work investigates flow over a wall-mounted cube placed in a spatially evolving turbulent boundary layer (SETBL) at a Reynolds number of 19,600. The Reynolds number is based on the mean boundary layer velocity and the inlet boundary layer thickness. A physics-based approach given by Le [1] is implemented to prescribe a time-varying inflow velocity field to simulate the SETBL. The method is described in detail in Sec. 2.4.2. We scrutinize the fundamental physics of the turbulent flow in the near-wake of the cube, and an accurate representation of the near-wake flow physics hinges on the accurate simulation of the turbulent boundary layer (TBL) at the Reynolds number of interest. The objective of this appendix is to demonstrate the accuracy of our numerical framework in simulating a SETBL at a Reynolds number of 19,600.

A.2 Computational approach

LES of a spatially evolving turbulent boundary layer on a flat plate is performed, at a Reynolds (Re_δ) number of 19,600, and a free-stream turbulence (FST) of 1%. Re_δ is based

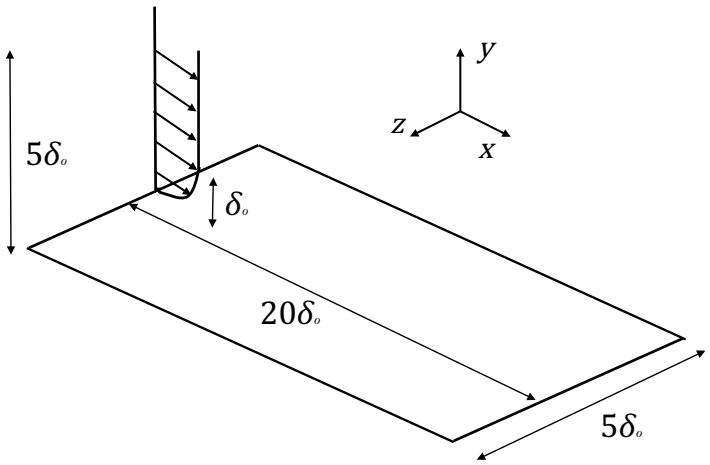

Figure A.1: Schematic of the problem setup.

on the mean boundary layer velocity (U_m) and inlet boundary layer thickness (δ_o). The Reynolds number and the level of FST is maintained constant across all the simulations of flow over a cube presented in this work. The geometrical setup of the flow configuration is depicted in Fig. A.1. The dimensions of the domain in the stream-wise (x), wall-normal (y), and span-wise (z) directions are $20\delta_o$, $5\delta_o$, and $5\delta_o$ respectively. The non-dimensional grid spacing[1] is $\Delta_x^+ = 15$, $\Delta_y^+ = 1$, and $\Delta_z^+ = 15$ in the x, y, and z directions respectively. The grid spacing is uniform in the x and z-directions, while we use a hyperbolic tangent stretching in the $y-$direction, with the smallest cells close to the wall. The computational approach, LES model and discretization schemes are same as those explained in Sec. 3.2. The bottom-wall is treated as a no-slip wall, whereas a slip (no-stress) wall boundary condition is imposed on the top-wall. The domain is periodic in the span-wise direction, and a zero-gradient boundary condition is prescribed on the outlet. A time-varying inflow boundary condition is imposed for the velocity field on the inlet boundary (Sec. 2.4.2).

A.3 Results and discussion

We consider the time-averaged velocity field and further average it in the span-wise

[1]The grid spacing is non-dimensional using inner variables: friction velocity (u_τ) and kinematic viscosity (ν).

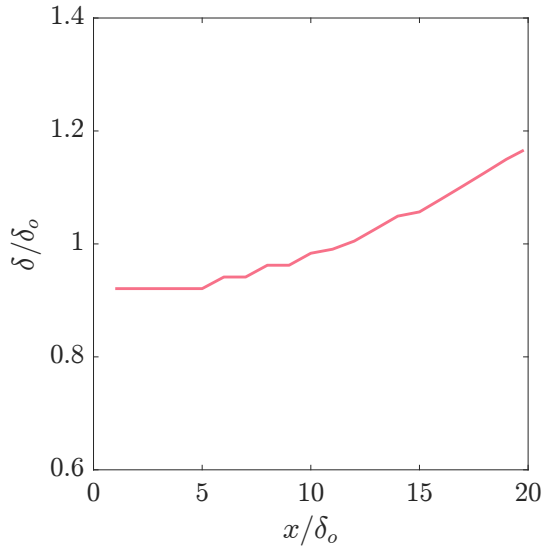

(a) Normalized boundary layer thickness vs. normalized stream-wise coordinate.

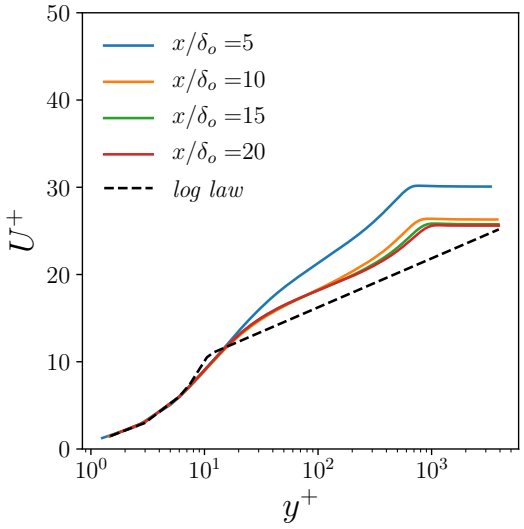

(b) Normalized mean velocity vs. normalized wall-normal coordinate (semi-log) at different stream-wise locations.

Figure A.2: Mean quantities averaged in time and the span-wise direction.

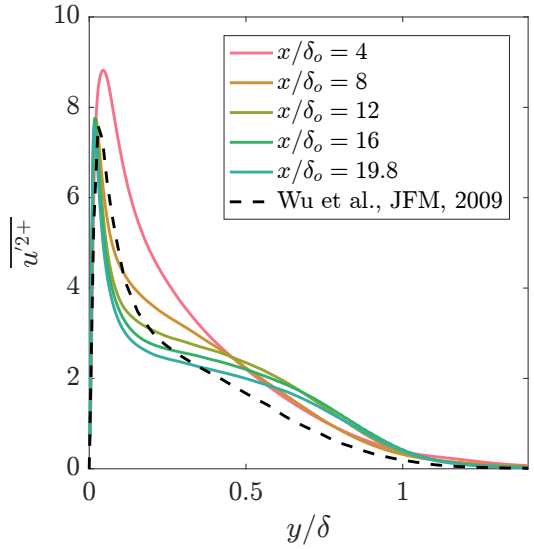

(a) $xx-$component.

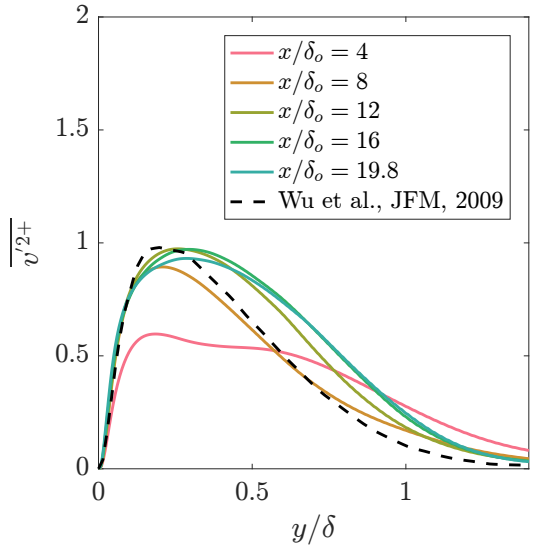

(b) $yy-$component.

Figure A.3: Normalized Reynolds stresses averaged in time and the span-wise direction.

direction. The averaged velocity field is used to estimate the boundary layer thickness ($99\%U_\infty$) as a function of the stream-wise coordinate, as demonstrated in Fig. A.2a. We observe that the boundary layer recovers its inlet value, δ_o, at a stream-wise distance of

$12\delta_o$ from the inlet. After $x = 12\delta_o$, the boundary layer thickness increases in a near-linear manner with increasing stream-wise distance. This observation is in agreement with the DNS of a SETBL on a flat plate [96]. The average velocity profiles are compared to the log law of the wall in Fig. A.2b. The profiles converge to a value which shows excellent agreement up to the buffer region ($y^+ < 10$), however, there is a small deviation in the logarithmic region. The mean velocity values are greater than those predicted by the log law, because of a favorable pressure gradient in the stream-wise direction. An ideal scenario to test the inflow method would be to have a zero pressure gradient in the stream-wise direction, however, it is numerically impossible to achieve a strictly zero pressure gradient [95]. The time-varying inflow velocity field does not obey the filtered Navier-Stokes equations at the inlet, and therefore, the solution to the poisson equation for pressure adjusts the pressure field to converge the system of equations. In Fig. A.3, we compare the time averaged and span-wise averaged velocity fluctuation profiles at different stream-wise locations with the DNS results of Wu *et al.* [95]. The stream-wise and wall-normal velocity fluctuations are in good agreement with the DNS results after $x \approx 12\delta_o$. Small discrepancies in the outer region of the boundary layer could be attributed to LES modeling errors, as the mesh is coarser in the outer region as compared to the near-wall region. From the results demonstrated in Fig. A.2 and Fig. A.3, we are confident that the boundary layer recovers its initial thickness (δ_o), and is fully turbulent at a stream-wise distance of $12\delta_o$ from the inlet. Hence, the cube is placed at a distance of $12\delta_o$ from the inlet boundary in all the simulations performed in this work.

APPENDIX B

Validation of the OpenFOAM numerical framework

B.1 Introduction

In the present work we solve the filtered Navier-Stokes equations with a finite volume approach using the open-source libraries of OpenFOAM [77]. The problem of interest is, flow over a wall-mounted cube placed inside a spatially evolving turbulent boundary layer (SETBL). The Reynolds number of the flow is $19,600$, based on the mean velocity and the incoming boundary layer thickness. Although the flow configuration is canonical in nature, this specific configuration has not been studied with either a high-fidelity numerical or an experimental approach for a similar Reynolds number. On the other hand, the flow over a wall-mounted cube placed in a fully developed channel flow has been investigated with similar parameters by many researchers in great detail [108, 54, 59, 10]. These studies demonstrate that flow over the cube is highly three-dimensional and unsteady with regions that exhibit back-scatter of turbulent kinetic energy. The large eddy simulation (LES) approach is most suited to accurately capture all the complex unsteady features of this flow. Before using the numerical framework provided by OpenFOAM to investigate turbulent flow physics, we deem it necessary to validate the framework for its ability to simulate this complex flow.

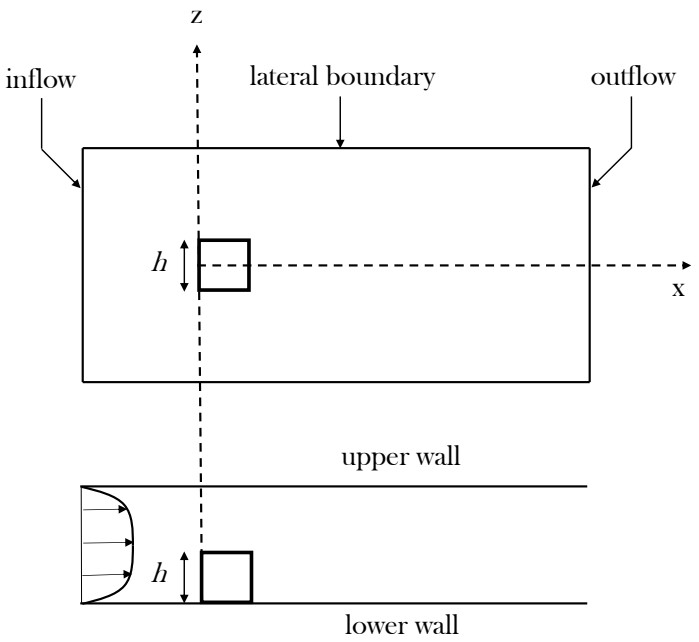

Figure B.1: Problem setup.

We chose to replicate the work done by Krajnovic *et al.* [12], and simulated the flow over a wall-mounted cube placed in a fully developed channel flow at a Reynolds number of 40,000. Our choice is motivated by the following facts: (i) Krajnovic *et al.* used similar LES models, (ii) the Reynolds number is of the same order of magnitude, and (iii) these computational results are validated against high quality experimental data for the same flow configuration from Hussein *et al.* [11].

B.2 Computational approach

Full details about the geometry and the numerical setup can be found in Krajnovic *et al.* [12]. The problem setup is shown in Fig. B.1 which depicts flow over a cube of height h, placed at a distance of $3h$ from the inflow boundary. The cube is placed inside a channel of height, $2h$, with no-slip boundary conditions imposed on the top and bottom-walls, and the cube surface. A zero-gradient boundary condition is imposed on the outflow boundary, and the side walls are treated with the slip boundary condition. The inflow boundary condition is a fully developed turbulent channel flow velocity profile, obtained from a precursor simulation

at $Re_h = 40,000$. The computational grid spacing mimics the finest resolution employed by Kranjnovic *et al.*, such that, $\Delta x^+ = 28.5$, $\Delta y^+ = 4.6$ and $\Delta z^+ = 23.7$, in the vicinity of the cube[1]. The discretization schemes are same as those described in Sec. 3.2. The dynamic $k-$equation LES model is used to account for the SGS influence [81].

B.3 Results and discussion

The separation (X_s) and reattachment (X_r) lengths from our simulation as presented in Table B.1. X_s and X_r are calculated from the skin-friction coefficient $C_f = \frac{\tau_w}{1/2\rho U_b^2}$, in the center-plane, along the bottom-wall of the domain. We obtain a 10% error in X_s and a 13% error in X_r relative to the experiments, by contrast to 9.1% error in X_s and 9.7% error in X_r, in the LES by Krajnovic *et al.* [12]. This discrepancy is partly due to the coarse nature of the grid near the separation and reattachment points, as local mesh resolution plays a larger role in accurately predicting X_s and X_r, than in predicting the flow over the top of the cube [12].

In figure B.2, we demonstrate the $x-$ and $y-$components of mean velocity, and the $xx-$ and $xy-$components of the Reynolds stress tensor. In general, the agreement of our results with the experiments is at least as good, if not better, than Krajnovic et al. [12], except for the $xy-$component. We expect that the agreement with experiments would be even better with simulations on a finer computational grid.

[1] the "+" symbol stands for dimensions expressed in wall-units, non-dimensionalized using friction velocity (u_τ), and kinematic viscosity (ν).

Contribution	LES Model	Grid	X_s/h	X_r/h
Martinuzzi and Tropea [11]	Experiment	—	1.04	1.61
Krajnovic *et al.* [12]	one equation	$210 \times 66 \times 114$	1.10	1.45
Krajnovic *et al.* [12]	localized dynamic one eqn.	$210 \times 66 \times 114$	1.13	1.44
Present simulations	one equation	$210 \times 66 \times 114$	0.936	1.82

* X_s: separation length in front of the cube, X_r: reattachment length behind the cube

Table B.1: Separation and reattachment lengths normalized by the cube height (h).

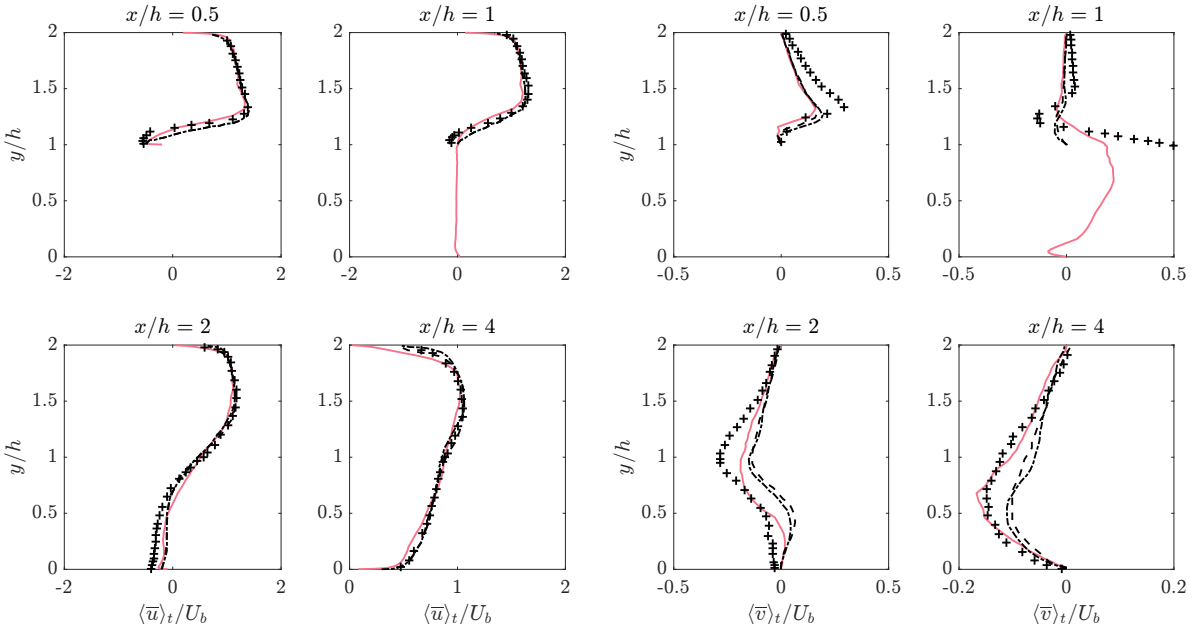

(a) x-component of mean velocity.

(b) y-component of mean velocity.

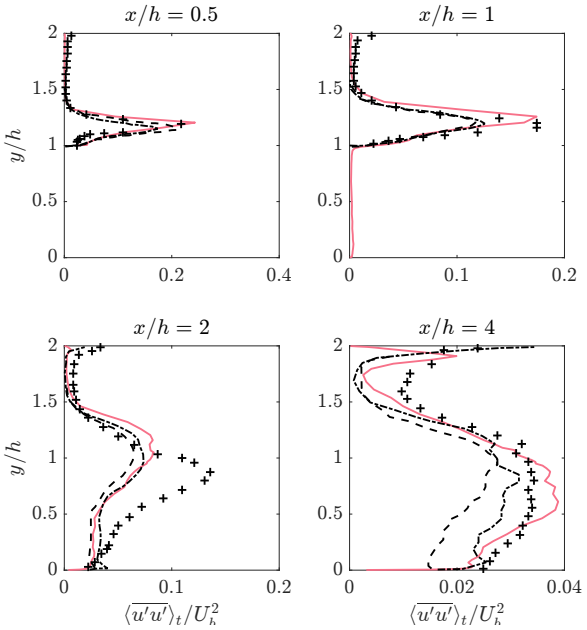

(c) xx-component of Reynolds stress.

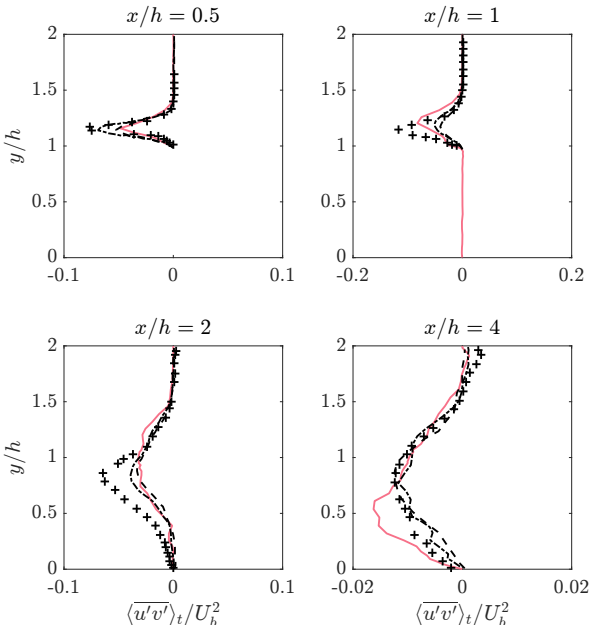

(d) xy-component of Reynolds stress.

Figure B.2: Mean velocity components and Reynolds stresses in the center plane for fully developed turbulent flow around a wall-mounted cube in a channel . +: experimental result [11]; dashed line: one equation model [12]; dash-dotted line: localized dynamic one equation model [12]; pink line: our results with dynamic $k-$equation model.

APPENDIX C

Grid refinement study of flow over a wall-mounted cube in a turbulent boundary layer

C.1 Introduction

The phenomenon of cascade of turbulent kinetic energy from larger scales to smaller scales, and dissipation of energy at the smallest scales (a.k.a. *kolmogorov scales*) is central to all turbulent flows. In wall-bounded turbulent flows, the kolmogorov length scales are governed by inner flow variables, namely, friction velocity (u_τ) and kinematic viscosity (ν). An accurate numerical simulation should ideally solve for all the length and time scales present in the flow, and such a simulation is called as Direct Numerical Simulation (DNS). In a DNS, the computational grid is of the order of the very fine kolmogorov length scales, with the grid spacing, $\Delta^+ \sim O(1)$[1]. Majority of turbulent flows of practical interest are at significantly high Reynolds numbers, including the flow under consideration in the present work. As the Reynolds number increases the kolmogorov length scales become smaller, and therefore, the very fine computational grid requirement renders DNS unusable for simulations

[1]the "+" indicates a quantity non-dimensionalized by the inner variables: friction velocity (u_τ), and kinematic viscosity (ν)

of such flows. In these situations, our best alternative for achieving high-fidelity is the Large Eddy Simulation (LES) approach. The physical intuition behind LES is explained in detail in Sec. 2.1.1, and essentially it involves resolving a major part of the turbulent kinetic energy (TKE) spectrum and accounting for the unresolved component using a LES model. The resolved scales correspond to the large length scales while the unresolved component represents the smallest length scales. This scale separation is achieved via a spatial filter. The accuracy of a LES depends on the percentage of the TKE spectrum resolved in the computation, which in turn is a function of the grid spacing.

In the present work we perform LES of a wall-mounted cube placed in a turbulent boundary layer (TBL). A TBL is characterized by very fine coherent structures near the wall, and a computational grid designed for such a simulation should take this into account. Therefore, we use a hyperbolic tangent stretching of grid cells in the direction normal to the no-slip walls, with the smallest cells placed near the wall. There are two important aspects to any numerical solution obtained with a LES,

1. *Accuracy*, is the measure of, how close the solution is to the true solution which may be obtained analytically or experimentally. We tested the accuracy of the numerical framework by comparing our simulation results with experimental data in Appendix B.

2. *Convergence* can be viewed as the robustness of the time-averaged quantities to changes in period of time-integration and grid spacing. A numerical solution obtained with a LES is considered to be converged, if any further refinement in the grid resolution does produce a significant change in the results. At this point the solution is said to be grid independent.

This is the rationale behind performing a grid refinement study. In this appendix, we demonstrate that grid independence is achieved on the fine mesh. All the observations presented in this thesis are obtained from the fine mesh simulations.

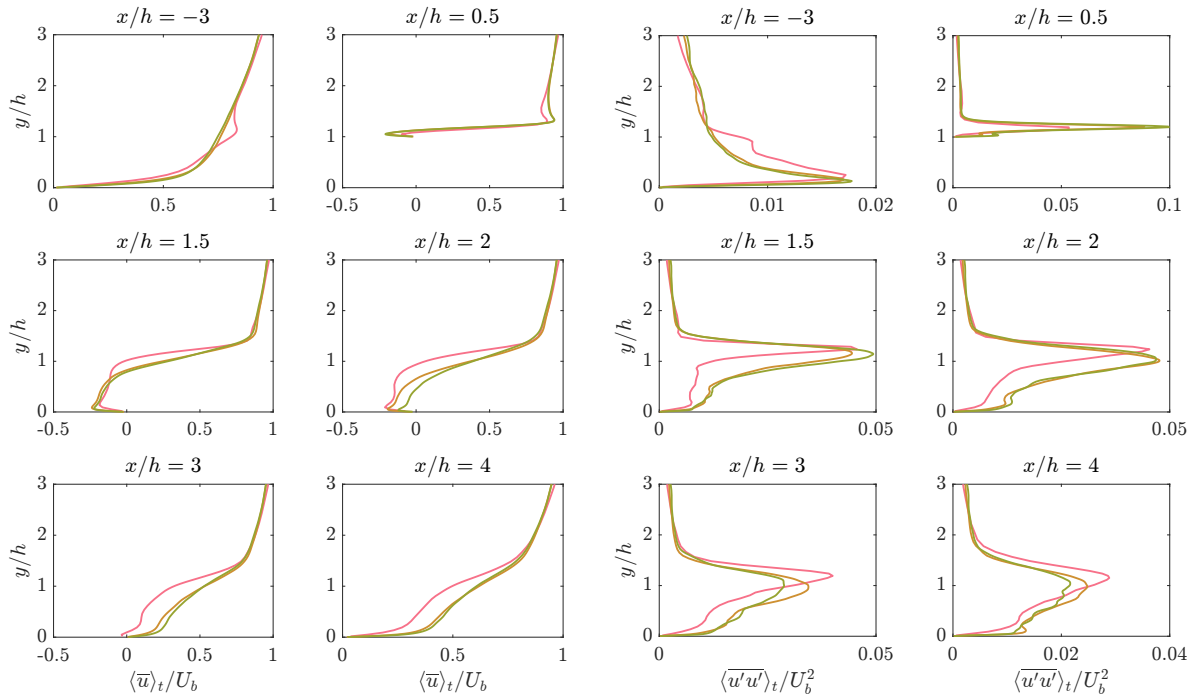

(a) x-component of mean velocity (b) xx-component of Reynolds stress

Figure C.1: Profiles of mean velocity (x-component) and Reynolds stress (xx-component) for spatially evolving turbulent boundary layer flow around a wall-mounted cube with $h/\delta_o = 0.2$. — coarse mesh, — medium mesh, — fine mesh.

C.2 Computational approach

To establish grid independence, we used three grids for each of the three different cube heights. The grids are labelled as coarse, medium, and fine. The non-dimensional grid spacing is same for the three cube heights. The details of the grid spacing are summarized in Table C.1. The computational approach, LES model, discretization schemes and boundary

Mesh	Δx^+_{min}	Δx^+_{max}	Δy^+_{min}	Δy^+_{max}	Δz^+_{min}	Δz^+_{max}
Coarse	21	104	2.5	200	21	146
Medium	18	80	0.5	200	18	125
Fine	16	74	0.5	200	16	110

* Δ^+ represents grid spacing in wall units. $\Delta^+ = \Delta u_\tau/\nu$

Table C.1: Non-dimensional grid spacing details.

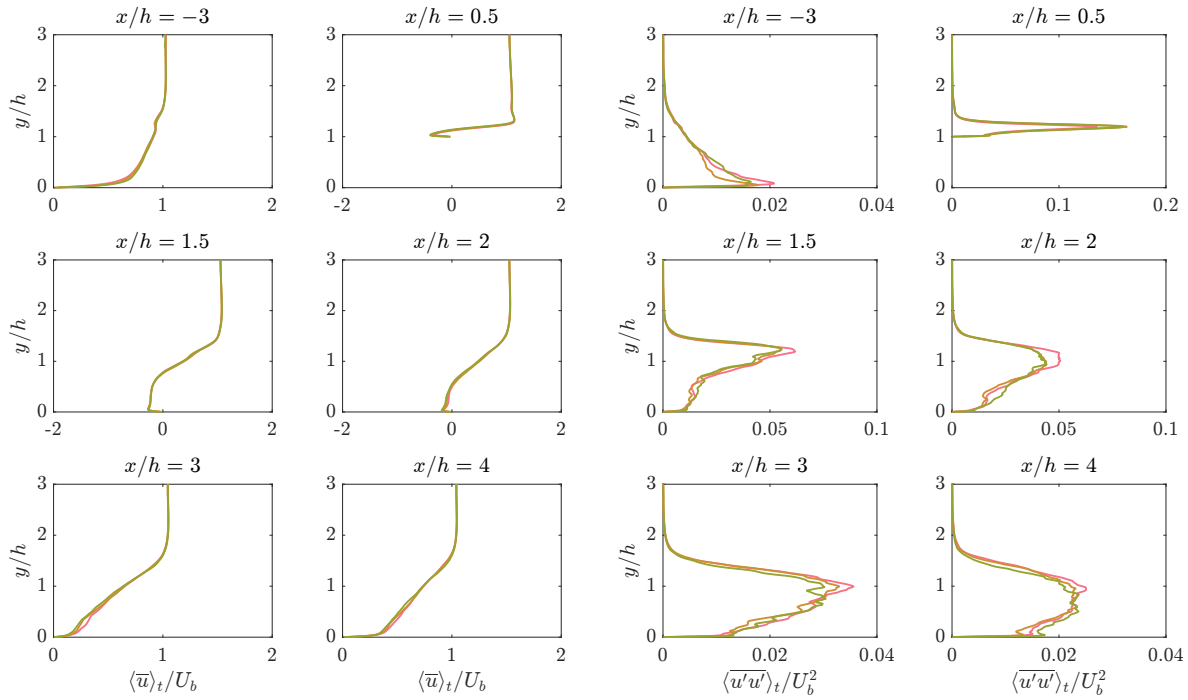

(a) x-component of mean velocity (b) xx-component of Reynolds stress

Figure C.2: Profiles of mean velocity (x-component) and Reynolds stress (xx-component) for spatially evolving turbulent boundary layer flow around a wall-mounted cube with $h/\delta_o = 0.6$. — coarse mesh, — medium mesh, — fine mesh.

conditions are explained in detail in Sec. 3.2.

C.3 Results and discussion

In Fig. C.1, C.2 and C.3, we present the streamwise component of mean velocity and $xx-$component of the Reynolds stress tensor, for three cube heights, $h/\delta_o = 0.2$, 0.6, and 1.0, on the coarse, medium, and fine mesh. For $h/\delta_o = 0.2$, we observe greater deviation in the $x-$component of mean velocity of the coarse mesh from the medium and fine mesh, than for the larger values of h/δ_o. For $h = 0.2\delta_o$, the coarse mesh has fewer cells across the cube height than for $h = 0.6\delta_o$ and $h = \delta_o$, resulting in poor agreement with the medium and fine mesh results. The results for $x-$component of mean velocity from medium and fine mesh cases are in good agreement for the three cube heights.

We observe noticeable deviations in the $xx-$component of Reynolds stress between the coarse, medium and fine mesh cases in Fig. C.1b, C.2b and C.3b. Since Reynolds stresses are

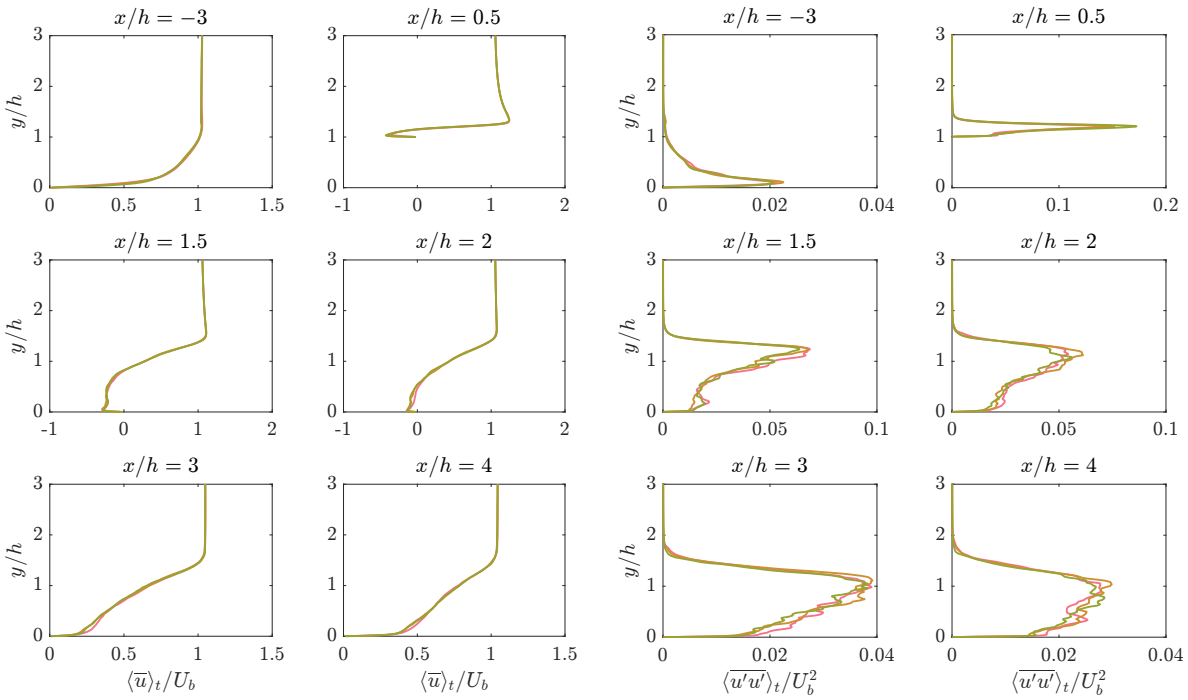

(a) x-component of mean velocity (b) xx-component of Reynolds stress

Figure C.3: Profiles of mean velocity (x-component) and Reynolds stress (xx-component) for spatially evolving turbulent boundary layer flow around a wall-mounted cube with $h/\delta_o = 1.0$. — coarse mesh, — medium mesh, — fine mesh.

calculated as the mean of the difference between instantaneous and time-average velocities, the magnitude of values under consideration are small. As a result any slight deviation from the mean gets amplified. From our experience and after a thorough literature review, we believe that the results in Fig. C.1b, C.2b and C.3b are acceptable, and that the fine mesh accurately represents the flow dynamics.

APPENDIX D

Validation of our calculation of the turbulent kinetic energy budget in OpenFOAM

In Chapter III and Chapter IV, we have put forward our observations regarding the variation of turbulent kinetic energy (TKE) and the individual terms in the TKE budget in the region around the cube. A utility was developed to perform these calculations in OpenFOAM, and we believe it is important to verify the accuracy of this implementation to support the validity of our observations. The purpose of this appendix is to validate our calculation of TKE budget in OpenFOAM. In order to achieve this objective we use the utility to calculate TKE budget for a spatially evolving turbulent boundary layer (SETBL) on a flat plate. The TKE budget is given by,

$$\begin{aligned}\frac{\partial(\frac{1}{2}q^2)}{\partial t} = &\underbrace{-\frac{1}{2}U_k\overline{(u_l'u_l')}_{,k}}_{C_k}\underbrace{-\overline{(u_l'u_k')}U_{l,k}}_{P_k}\underbrace{-\frac{1}{2}\overline{(u_l'u_l'u_k')}_{,k}}_{T_k}\\ &\underbrace{+\frac{1}{2}\left(\frac{1}{Re}+\nu_\tau\right)\overline{(u_l'u_l')}_{,kk}}_{D_k}\underbrace{-\left(\frac{1}{Re}+\nu_\tau\right)\overline{u_{l,k}'u_{l,k}'}}_{\epsilon_k}\underbrace{-\overline{u_l'p_{,l}'}}_{\Pi_k},\end{aligned} \tag{D.1}$$

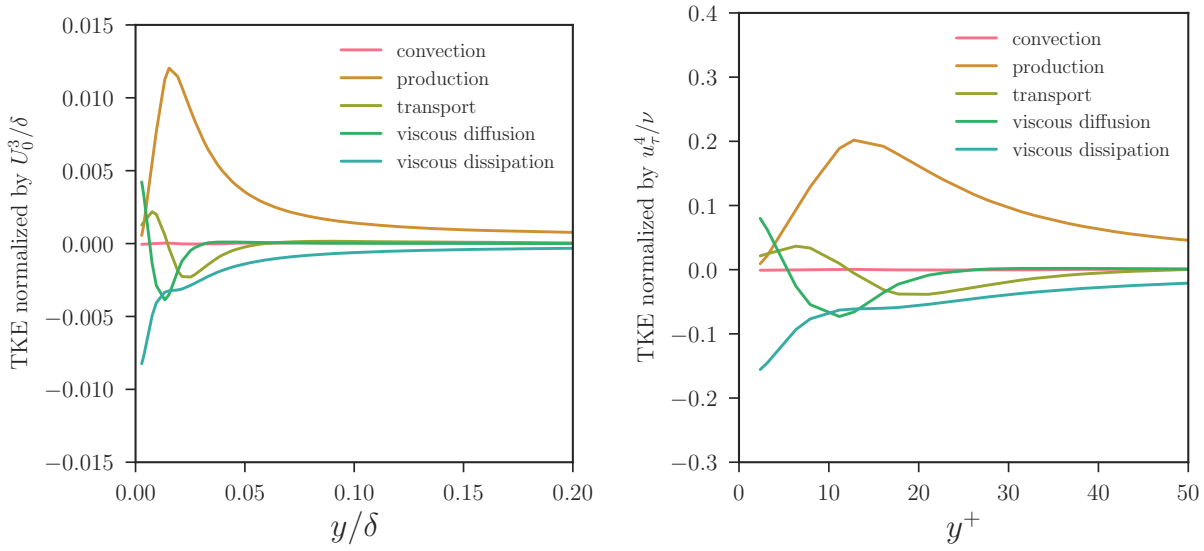

(a) Normalized by outer coordinates

(b) Normalized by inner coordinates

Figure D.1: TKE budget terms in a turbulent boundary layer on a flat plate at a stream-wise location of $x = 18\delta_o$ from the inlet.

where

$$\frac{1}{2}q^2 = \frac{1}{2}(\overline{u'^2} + \overline{v'^2} + \overline{w'^2}) \tag{D.2}$$

$\frac{1}{2}q^2$ is the turbulent kinetic energy, $Re = \frac{U_m \delta}{\nu}$ is the Reynolds number based on mean velocity (U_m) and boundary layer thickness (δ), ν_τ is the eddy viscosity in the LES model. The over-bar represents a time average. The terms on the right hand side of Eq. D.1 are: convection (C_k), production (P_k), turbulence transport (T_k), viscous diffusion (D_k), viscous dissipation (ϵ_k) and velocity-pressure gradient (Π_k).

A LES of a spatially evolving turbulent boundary layer on a flat plate is performed at a Reynolds number (Re_m) of 7000, based on the inflow boundary layer thickness and the mean velocity. The computational setup of the simulation is same as that explained in Sec. 2.4.2. We explain in Sec. 2.4.2 that the flow requires a transition length of approximately $12\delta_o$ for the flow to develop in a realistic turbulent boundary layer, where δ_o is the boundary layer thickness at the inlet. Therefore, we consider a plane after the transition distance at a

stream-wise location of $x = 18\delta_o$ and present the wall-normal variation of the TKE budget terms in Fig. D.1.

The TKE budget terms are normalized by the outer coordinates (mean TBL velocity, U_o, and boundary layer thickness, δ) in Fig. D.1a, and by the inner coordinates (friction velocity, u_τ, and kinematic viscosity, ν) in Fig. D.1b. The variation of the TKE budget terms in both these figures is in good agreement with those presented by Le *et al.* [118] for a SETBL on the upper surface of a backward-facing step before the flow separates. We are confident that our utility for the calculation of TKE budget in OpenFOAM gives accurate results.

BIBLIOGRAPHY

BIBLIOGRAPHY

[1] Hung Le. *Direct numerical simulation of turbulent flow over a backward facing step.* PhD thesis, Stanford University, 1995.

[2] J Lin. Review of research on low-profile vortex generators to control boundary-layer separation. *Progress in Aerospace Sciences*, 38(4):389–420, 2002.

[3] C Cuvier. *Active control of a separated turbulent boundary layer in adverse pressure gradient.* PhD thesis, Ecole Centrale de Lille, 2012.

[4] L Cattafesta III and M Sheplak. Actuators for active flow control. *Annual Review of Fluid Mechanics*, 43:247–272, 2011.

[5] R Barnard. *Road vehicle aerodynamic design-an introduction.* 2001.

[6] Learning can be a 'drag'. `https://www.nasa.gov/multimedia/imagegallery/image_feature_1622.html`. Accessed: 2018-04-07.

[7] C Hinterberger, M Garcia-Villalba, and W Rodi. Large eddy simulation of flow around the ahmed body. In *The Aerodynamics of Heavy Vehicles: Trucks, Buses, and Trains*, pages 77–87. Springer, 2004.

[8] G Pujals, S Depardon, and C Cossu. Drag reduction of a 3d bluff body using coherent streamwise streaks. *Experiments in Fluids*, 49(5):1085–1094, 2010.

[9] C Escauriaza and F Sotiropoulos. Reynolds number effects on the coherent dynamics of the turbulent horseshoe vortex system. *Flow, Turbulence and Combustion*, 86(2):231–262, 2011.

[10] A Yakhot, T Anor, H Liu, and N Nikitin. Direct numerical simulation of turbulent flow around a wall-mounted cube: spatio-temporal evolution of large-scale vortices. *Journal of Fluid Mechanics*, 566(1):1–9, 2006.

[11] H Hussein and R Martinuzzi. Energy balance for turbulent flow around a surface mounted cube placed in a channel. *Physics of Fluids*, 8(3):764–780, 1996.

[12] S Krajnovic and L Davidson. Large-eddy simulation of the flow around a bluff body. *AIAA Journal*, 40(5):927–936, 2002.

[13] A Kolmogorov. The local structure of turbulence in incompressible viscous fluid for very large reynolds numbers. In *Dokl. Akad. Nauk SSSR*, volume 30, pages 299–303, 1941.

[14] L Prandtl. Über flussigkeitsbewegung bei sehr kleiner reibung. *Verhandl. III, Internat. Math.-Kong., Heidelberg, Teubner, Leipzig, 1904*, pages 484–491, 1904.

[15] O Reynolds. O. reynolds, philos. trans. r. soc. london 174, 935 (1883). *Philos. Trans. R. Soc. London*, 174:935, 1883.

[16] O Reynolds. Study of fluid motion by means of colored bands. *Nature*, 50(1285):161–164, 1894.

[17] S Kline, W Reynolds, F Schraub, and P Runstadler. The structure of turbulent boundary layers. *Journal of Fluid Mechanics*, 30(4):741–773, 1967.

[18] H Kim, S Kline, and W Reynolds. The production of turbulence near a smooth wall in a turbulent boundary layer. *Journal of Fluid Mechanics*, 50(1):133–160, 1971.

[19] W George. Recent advancements toward the understanding of turbulent boundary layers. *AIAA Journal*, 44(11):2435–2449, 2006.

[20] W George. Is there a universal log law for turbulent wall-bounded flows? *Philosophical Transactions of the Royal Society of London A: Mathematical, Physical and Engineering Sciences*, 365(1852):789–806, 2007.

[21] G Brown and A Thomas. Large structure in a turbulent boundary layer. *Physics of Fluids*, 20(10):S243–S252, 1977.

[22] R Adrian, C Meinhart, and C Tomkins. Vortex organization in the outer region of the turbulent boundary layer. *Journal of Fluid Mechanics*, 422:1–54, 2000.

[23] D Coles. The law of the wake in the turbulent boundary layer. *Journal of Fluid Mechanics*, 1(2):191–226, 1956.

[24] P Spalart. Direct simulation of a turbulent boundary layer up to r θ= 1410. *Journal of Fluid Mechanics*, 187:61–98, 1988.

[25] S Robinson. Coherent motions in the turbulent boundary layer. *Annual Review of Fluid Mechanics*, 23(1):601–639, 1991.

[26] M Skote. *Studies of turbulent boundary layer flow throughdirect numerical simulation.* PhD thesis, Mekanik, 2001.

[27] M Skote and D Henningson. Direct numerical simulation of a separated turbulent boundary layer. *Journal of Fluid Mechanics*, 471:107–136, 2002.

[28] B Stratford. The prediction of separation of the turbulent boundary layer. *Journal of Fluid Mechanics*, 5(01):1–16, 1959.

[29] R Simpson, Y Chew, and B Shivaprasad. The structure of a separating turbulent boundary layer. part 1. Mean flow and Reynolds stresses. *Journal of Fluid Mechanics*, 113:23–51, 1981.

[30] Y Na and P Moin. Direct numerical simulation of a separated turbulent boundary layer. *Journal of Fluid Mechanics*, 374:379–405, 1998.

[31] A Smits and D Wood. The response of turbulent boundary layers to sudden perturbations. *Annual Review of Fluid Mechanics*, 17(1):321–358, 1985.

[32] A Alving and H Fernholz. Turbulence measurements around a mild separation bubble and downstream of reattachment. *Journal of Fluid Mechanics*, 322:297–328, 1996.

[33] J Neumann and H Wengle. Dns and les of passively controlled turbulent backward-facing step flow. *Flow, Turbulence and Combustion*, 71(1-4):297, 2003.

[34] J Neumann and H Wengle. Coherent structures in controlled separated flow over sharp-edged and rounded steps. *Journal of Turbulence*, 5(22):14, 2004.

[35] H Taylor. The elimination of diffuser separation by vortex generators. *United Aircraft Corporation, East Hartford, CT, Technical Report No*, 4012:3, 1947.

[36] J Lin, F Howard, D Bushnell, and G Selby. Investigation of several passive and active methods for turbulent flow separation control. In *AIAA, Fluid Dynamics, 21st Plasma Dynamics and Lasers Conference, 21st, Seattle, WA, June 18-20, 1990. 17 p.*, volume 1, 1990.

[37] G Godard and M Stanislas. Control of a decelerating boundary layer. part 1: Optimization of passive vortex generators. *Aerospace Science and Technology*, 10(3):181–191, 2006.

[38] D Rao and T Kariya. Boundary-layer submerged vortex generators for separation control-an exploratory study. *AIAA Paper*, 3546:1988, 1988.

[39] G Schubauer and H Skramstad. Laminar-boundary-layer oscillations and transition on a flat plate. Technical report, National Aeronautics And Space Administration Washington DC, 1948.

[40] G Selby, J Lin, and F Howard. Control of low-speed turbulent separated flow using jet vortex generators. *Experiments in Fluids*, 12(6):394–400, 1992.

[41] K McManus, P Joshi, H Legner, and S Davis. Active control of aerodynamic stall using pulsed jet actuators. In *Fluid Dynamics Conference*, page 2187, 1995.

[42] C Tilmann, K Langan, J Betterton, and M Wilson. Characterization of pulsed vortex generator jets for active flow control. Technical report, Air Force Research Lab Wright-Patterson AFB OH Air Vehicles Directorate, 2003.

[43] C Tilmann. Enhancement of transonic airfoil performance using pulsed jets for separation control. In *39th Aerospace Sciences Meeting and Exhibit*, page 731, 2001.

[44] J Magill, M Bachmann, G Rixon, and K McManus. Dynamic stall control using a model-based observer. *Journal of Aircraft*, 40(2):355–362, 2003.

[45] R Becker, R King, R Petz, and W Nitsche. Adaptive closed-loop separation control on a high-lift configuration using extremum seeking. *AIAA Journal*, 45(6):1382–1392, 2007.

[46] G Godard and M Stanislas. Control of a decelerating boundary layer. part 3: Optimization of round jets vortex generators. *Aerospace Science and Technology*, 10(6):455–464, 2006.

[47] Fast facts on transportation greenhouse gas emissions. `https://www.epa.gov/greenvehicles/fast-facts-transportation-greenhouse-gas-emissions`. Accessed: 2018-03-26.

[48] W Hucho and G Sovran. Aerodynamics of road vehicles. *Annual Review of Fluid Mechanics*, 25(1):485–537, 1993.

[49] S Ahmed, G Ramm, and G Faltin. Some salient features of the time-averaged ground vehicle wake. Technical report, SAE Technical Paper, 1984.

[50] P Joseph, X Amandolèse, and J Aider. Drag reduction on the 25 slant angle ahmed reference body using pulsed jets. *Experiments in Fluids*, 52(5):1169–1185, 2012.

[51] A Thacker, S Aubrun, A Leroy, and P Devinant. Experimental characterization of flow unsteadiness in the centerline plane of an ahmed body rear slant. *Experiments in Fluids*, 54(3):1479, 2013.

[52] M Minguez, R Pasquetti, and E Serre. High-order large-eddy simulation of flow over the ?ahmed body? car model. *Physics of Fluids*, 20(9):095101, 2008.

[53] G Pujals, C Cossu, and S Depardon. Optimal transient growth and very large-scale structures in zero-pressure gradient turbulent boundary layers. In *TSFP Digital Library Online*. Begel House Inc., 2009.

[54] R Martinuzzi and C Tropea. The flow around surface-mounted, prismatic obstacles placed in a fully developed channel flow. *Journal of Fluids Engineering*, 115(1):85–92, 1993.

[55] W Rodi. Comparison of les and rans calculations of the flow around bluff bodies. *Journal of Wind Engineering and Industrial Aerodynamics*, 69:55–75, 1997.

[56] G Iaccarino, A Ooi, P Durbin, and M Behnia. Reynolds averaged simulation of unsteady separated flow. *International Journal of Heat and Fluid Flow*, 24(2):147–156, 2003.

[57] K Shah and J Ferziger. A fluid mechanicians view of wind engineering: Large eddy simulation of flow past a cubic obstacle. *Journal of Wind Engineering and Industrial Aerodynamics*, 67:211–224, 1997.

[58] K Shah. Large eddy simulations of flow past a cubic obstacle. 1998.

[59] S Krajnovic and L Davidson. Large-eddy simulation of the flow around a surface-mounted cube using a dynamic one-equation subgrid model. In *TSFP Digital Library Online*. Begel House Inc., 1999.

[60] A Liakos and N Malamataris. Direct numerical simulation of steady state, three dimensional, laminar flow around a wall mounted cube. *Physics of Fluids*, 26(5):053603, 2014.

[61] A Yakhot, H Liu, and N Nikitin. Turbulent flow around a wall-mounted cube: A direct numerical simulation. *International Journal of Heat and Fluid Flow*, 27(6):994–1009, 2006.

[62] V Kolář. Vortex identification: New requirements and limitations. *International Journal of Heat and Fluid Flow*, 28(4):638–652, 2007.

[63] J Sillero, J Jiménez, and R Moser. One-point statistics for turbulent wall-bounded flows at reynolds numbers up to $\delta^+ \approx 2000$. *Physics of Fluids*, 25(10):105102, 2013.

[64] M Calaf, M Parlange, and C Meneveau. Large eddy simulation study of scalar transport in fully developed wind-turbine array boundary layers. *Physics of Fluids*, 23(12):126603, 2011.

[65] J Finnigan, R Shaw, and E Patton. Turbulence structure above a vegetation canopy. *Journal of Fluid Mechanics*, 637:387–424, 2009.

[66] S Belcher, I Harman, and J Finnigan. The wind in the willows: flows in forest canopies in complex terrain. *Annual Review of Fluid Mechanics*, 44:479–504, 2012.

[67] H Cheng and I Castro. Near wall flow over urban-like roughness. *Boundary-Layer Meteorology*, 104(2):229–259, 2002.

[68] S Belcher, N Jerram, and J Hunt. Adjustment of a turbulent boundary layer to a canopy of roughness elements. *Journal of Fluid Mechanics*, 488:369–398, 2003.

[69] O Coceal, A Dobre, T Thomas, and S Belcher. Structure of turbulent flow over regular arrays of cubical roughness. *Journal of Fluid Mechanics*, 589:375–409, 2007.

[70] Z Xie, O Coceal, and I Castro. Large-eddy simulation of flows over random urban-like obstacles. *Boundary-Layer Meteorology*, 129(1):1, 2008.

[71] W Anderson, Q Li, and E Bou-Zeid. Numerical simulation of flow over urban-like topographies and evaluation of turbulence temporal attributes. *Journal of Turbulence*, 16(9):809–831, 2015.

[72] M Shockling, J Allen, and A Smits. Roughness effects in turbulent pipe flow. *Journal of Fluid Mechanics*, 564:267–285, 2006.

[73] M Schultz and K Flack. The rough-wall turbulent boundary layer from the hydraulically smooth to the fully rough regime. *Journal of Fluid Mechanics*, 580:381–405, 2007.

[74] Y Wu and K Christensen. Outer-layer similarity in the presence of a practical rough-wall topography. *Physics of Fluids*, 19(8):085108, 2007.

[75] J Lee, H Sung, and P Krogstad. Direct numerical simulation of the turbulent boundary layer over a cube-roughened wall. *Journal of Fluid Mechanics*, 669:397–431, 2011.

[76] A Townsend. *The structure of turbulent shear flow*. Cambridge university press, 1980.

[77] H Weller, G Tabor, H Jasak, and C Fureby. A tensorial approach to computational continuum mechanics using object-oriented techniques. *Computers in Physics*, 12(6):620–631, 1998.

[78] H Choi and P Moin. Grid-point requirements for large eddy simulation: Chapman?s estimates revisited. *Physics of fluids*, 24(1):011702, 2012.

[79] L Richardson. *Weather prediction by numerical process*. Cambridge University Press, 2007.

[80] C Meneveau and J Katz. Scale-invariance and turbulence models for large-eddy simulation. *Annual Review of Fluid Mechanics*, 32(1):1–32, 2000.

[81] Wand Kim and S Menon. A new dynamic one-equation subgrid-scale model for large eddy simulations. In *33rd Aerospace Sciences Meeting and Exhibit*, page 356, 1995.

[82] M Germano, U Piomelli, P Moin, and W Cabot. A dynamic subgrid-scale eddy viscosity model. *Physics of Fluids A: Fluid Dynamics*, 3(7):1760–1765, 1991.

[83] E Robertson, V Choudhury, S Bhushan, and D Walters. Validation of openfoam numerical methods and turbulence models for incompressible bluff body flows. *Computers & Fluids*, 123:122–145, 2015.

[84] Y Cao and T Tamura. Large-eddy simulations of flow past a square cylinder using structured and unstructured grids. *Computers & Fluids*, 137:36–54, 2016.

[85] S Patankar and D Spalding. A calculation procedure for heat, mass and momentum transfer in three-dimensional parabolic flows. In *Numerical Prediction of Flow, Heat Transfer, Turbulence and Combustion*, pages 54–73. Elsevier, 1983.

[86] R Issa. Solution of the implicitly discretised fluid flow equations by operator-splitting. *Journal of Computational Physics*, 62(1):40–65, 1986.

[87] R Mittal and P Moin. Suitability of upwind-biased finite difference schemes for large-eddy simulation of turbulent flows. *AIAA Journal*, 35(8):1415–1417, 1997.

[88] G Tabor and M Baba-Ahmadi. Inlet conditions for large eddy simulation: a review. *Computers & Fluids*, 39(4):553–567, 2010.

[89] P Batten, U Goldberg, and S Chakravarthy. Interfacing statistical turbulence closures with large-eddy simulation. *AIAA Journal*, 42(3):485–492, 2004.

[90] L Davidson and M Billson. Hybrid les-rans using synthesized turbulent fluctuations for forcing in the interface region. *International Journal of Heat and Fluid Flow*, 27(6):1028–1042, 2006.

[91] P Druault, S Lardeau, J Bonnet, F Coiffet, J Delville, E Lamballais, J Largeau, and L Perret. Generation of three-dimensional turbulent inlet conditions for large-eddy simulation. *AIAA Journal*, 42(3):447–456, 2004.

[92] L Di Mare, M Klein, W Jones, and J Janicka. Synthetic turbulence inflow conditions for large-eddy simulation. *Physics of Fluids*, 18(2):025107, 2006.

[93] N Jarrin, R Prosser, J Uribe, S Benhamadouche, and D Laurence. Reconstruction of turbulent fluctuations for hybrid rans/les simulations using a synthetic-eddy method. *International Journal of Heat and Fluid Flow*, 30(3):435–442, 2009.

[94] R Poletto, T Craft, and A Revell. A new divergence free synthetic eddy method for the reproduction of inlet flow conditions for les. *Flow, Turbulence and Combustion*, 91(3):519–539, 2013.

[95] X Wu and P Moin. Direct numerical simulation of turbulence in a nominally zero-pressure-gradient flat-plate boundary layer. *Journal of Fluid Mechanics*, 630:5–41, 2009.

[96] A Ferrante and S Elghobashi. A robust method for generating inflow conditions for direct simulations of spatially-developing turbulent boundary layers. *Journal of Computational Physics*, 198(1):372–387, 2004.

[97] L Prandtl. Bericht uber untersuchungen zur ausgebildeten turbulenz. *Zs. angew. Math. Mech.*, 5:136–139, 1925.

[98] P Spalart and J Watmuff. Experimental and numerical study of a turbulent boundary layer with pressure gradients. *Journal of Fluid Mechanics*, 249:337–371, 1993.

[99] D De Graaff and J Eaton. Reynolds-number scaling of the flat-plate turbulent boundary layer. *Journal of Fluid Mechanics*, 422:319–346, 2000.

[100] JU Schlüter, H Pitsch, and P Moin. Large-eddy simulation inflow conditions for coupling with reynolds-averaged flow solvers. *AIAA Journal*, 42(3):478–484, 2004.

[101] T Lund, X Wu, and K Squires. Generation of turbulent inflow data for spatially-developing boundary layer simulations. *Journal of Computational Physics*, 140(2):233–258, 1998.

[102] M Baba-Ahmadi and G Tabor. Inlet conditions for les using mapping and feedback control. *Computers & Fluids*, 38(6):1299–1311, 2009.

[103] B Silverman. *Density estimation for statistics and data analysis*, volume 26. CRC press, 1986.

[104] J Kim, P Moin, and R Moser. Turbulence statistics in fully developed channel flow at low reynolds number. *Journal of Fluid Mechanics*, 177:133–166, 1987.

[105] L Devroye. Sample-based non-uniform random variate generation. In *Proceedings of the 18th conference on Winter simulation*, pages 260–265. ACM, 1986.

[106] E Meinders and K Hanjalić. Vortex structure and heat transfer in turbulent flow over a wall-mounted matrix of cubes. *International Journal of Heat and fluid flow*, 20(3):255–267, 1999.

[107] E Meinders, K Hanjalic, and R Martinuzzi. Experimental study of the local convection heat transfer from a wall-mounted cube in turbulent channel flow. *Journal of Heat Transfer*, 121(3):564–573, 1999.

[108] I Castro and A Robins. The flow around a surface-mounted cube in uniform and turbulent streams. *Journal of Fluid Mechanics*, 79(2):307–335, 1977.

[109] J Hwang and K Yang. Numerical study of vortical structures around a wall-mounted cubic obstacle in channel flow. *Physics of Fluids*, 16(7):2382–2394, 2004.

[110] W. Rodi. Large-eddy simulation of the flow past bluff bodies. *Closure Strategies for Turbulent and Transitional Flows*, pages 361–391, 2002.

[111] C Smith and S Metzler. The characteristics of low-speed streaks in the near-wall region of a turbulent boundary layer. *Journal of Fluid Mechanics*, 129:27–54, 1983.

[112] C Tomkins and R Adrian. Spanwise structure and scale growth in turbulent boundary layers. *Journal of Fluid Mechanics*, 490:37–74, 2003.

[113] M Guala, S Hommema, and R Adrian. Large-scale and very-large-scale motions in turbulent pipe flow. *Journal of Fluid Mechanics*, 554:521–542, 2006.

[114] K Kim and R Adrian. Very large-scale motion in the outer layer. *Physics of Fluids*, 11(2):417–422, 1999.

[115] S Shinde, S Tandon, K Maki, and E Johnsen. Flow separation over a backward-facing ramp with and without a vortex generator. In *46th AIAA Fluid Dynamics Conference*, page 3795, 2016.

[116] S Shinde, E Johnsen, and K Maki. Large eddy simulation of flow over a wall-mounted cube placed in a turbulent boundary layer. In *47th AIAA Fluid Dynamics Conference*, page 3640, 2017.

[117] K Angele and B Muhammad-Klingmann. The effect of streamwise vortices on the turbulence structure of a separating boundary layer. *European Journal of Mechanics-Fluids*, 24(5):539–554, 2005.

[118] H Le, P Moin, and J Kim. Direct numerical simulation of turbulent flow over a backward-facing step. *Journal of Fluid Mechanics*, 330:349–374, 1997.

[119] R Hearst, G Gomit, and B Ganapathisubramani. Effect of turbulence on the wake of a wall-mounted cube. *Journal of Fluid Mechanics*, 804:513–530, 2016.

[120] J Hunt, C Abell, J Peterka, and H Woo. Kinematical studies of the flows around free or surface-mounted obstacles; applying topology to flow visualization. *Journal of Fluid Mechanics*, 86(1):179–200, 1978.

[121] W Schofield and E Logan. Turbulent shear flow over surface mounted obstacles. *Journal of Fluids Engineering*, 112(4):376–385, 1990.

[122] A Larousse, R Martinuzzi, and C Tropea. Flow around surface-mounted, three-dimensional obstacles. In *8th Symposium on Turbulent Shear Flows, Volume 1*, volume 1, pages 14–4, 1991.

[123] C Tomkins. The structure of turbulence over smooth and rough walls. 2001.

[124] P Orlandi, S Leonardi, and R Antonia. Turbulent channel flow with either transverse or longitudinal roughness elements on one wall. *Journal of Fluid Mechanics*, 561:279–305, 2006.

[125] J Del Álamo and J Jimenez. Linear energy amplification in turbulent channels. *Journal of Fluid Mechanics*, 559:205–213, 2006.

[126] Y Hwang and C Cossu. Self-sustained process at large scales in turbulent channel flow. *Physical Review Letters*, 105(4):044505, 2010.

[127] Y Tominaga. Flow around a high-rise building using steady and unsteady rans cfd: Effect of large-scale fluctuations on the velocity statistics. *Journal of Wind Engineering and Industrial Aerodynamics*, 142:93–103, 2015.

[128] A Singh, S Medida, and K Duraisamy. Machine-learning-augmented predictive modeling of turbulent separated flows over airfoils. *AIAA Journal*, pages 1–13, 2017.

[129] B Blocken, T Defraeye, D Derome, and J Carmeliet. High-resolution cfd simulations for forced convective heat transfer coefficients at the facade of a low-rise building. *Building and Environment*, 44(12):2396–2412, 2009.

[130] S Tandon, S Shinde, K Maki, and E Johnsen. Flow control using passive vortex generators. In *47th AIAA Fluid Dynamics Conference*, page 3318, 2017.

[131] K Flack, M Schultz, and J Connelly. Examination of a critical roughness height for outer layer similarity. *Physics of Fluids*, 19(9):095104, 2007.

[132] B Ničeno, A Dronkers, and K Hanjalić. Turbulent heat transfer from a multi-layered wall-mounted cube matrix: a large eddy simulation. *International Journal of Heat and fluid flow*, 23(2):173–185, 2002.

[133] E Meinders and K Hanjalić. Experimental study of the convective heat transfer from in-line and staggered configurations of two wall-mounted cubes. *International Journal of Heat and mass transfer*, 45(3):465–482, 2002.